

## **INFORMATION TO USERS**

**This manuscript has been reproduced from the microfilm master. UMI films the text directly from the original or copy submitted. Thus, some thesis and dissertation copies are in typewriter face, while others may be from any type of computer printer.**

**The quality of this reproduction is dependent upon the quality of the copy submitted. Broken or indistinct print, colored or poor quality illustrations and photographs, print bleedthrough, substandard margins, and improper alignment can adversely affect reproduction.**

**In the unlikely event that the author did not send UMI a complete manuscript and there are missing pages, these will be noted. Also, if unauthorized copyright material had to be removed, a note will indicate the deletion.**

**Oversize materials (e.g., maps, drawings, charts) are reproduced by sectioning the original, beginning at the upper left-hand corner and continuing from left to right in equal sections with small overlaps.**

**ProQuest Information and Learning  
300 North Zeeb Road, Ann Arbor, MI 48106-1346 USA  
800-521-0600**

**UMI<sup>®</sup>**



## **NOTE TO USERS**

**This reproduction is the best copy available.**

UMI<sup>®</sup>



The Cool Interstellar Medium of NGC 5866

by

Glenn Kacprzak

A THESIS SUBMITTED IN PARTIAL FULFILMENT OF  
THE REQUIREMENTS FOR THE DEGREE OF

MASTER OF SCIENCE

in

Astronomy

(Department of Astronomy and Physics)

SAINT MARY'S UNIVERSITY

September 26, 2005

© Glenn Kacprzak, 2005



Library and  
Archives Canada

Bibliothèque et  
Archives Canada

0-494-06967-8

Published Heritage  
Branch

Direction du  
Patrimoine de l'édition

395 Wellington Street  
Ottawa ON K1A 0N4  
Canada

395, rue Wellington  
Ottawa ON K1A 0N4  
Canada

**NOTICE:**

The author has granted a non-exclusive license allowing Library and Archives Canada to reproduce, publish, archive, preserve, conserve, communicate to the public by telecommunication or on the Internet, loan, distribute and sell theses worldwide, for commercial or non-commercial purposes, in microform, paper, electronic and/or any other formats.

The author retains copyright ownership and moral rights in this thesis. Neither the thesis nor substantial extracts from it may be printed or otherwise reproduced without the author's permission.

**AVIS:**

L'auteur a accordé une licence non exclusive permettant à la Bibliothèque et Archives Canada de reproduire, publier, archiver, sauvegarder, conserver, transmettre au public par télécommunication ou par l'Internet, prêter, distribuer et vendre des thèses partout dans le monde, à des fins commerciales ou autres, sur support microforme, papier, électronique et/ou autres formats.

L'auteur conserve la propriété du droit d'auteur et des droits moraux qui protègent cette thèse. Ni la thèse ni des extraits substantiels de celle-ci ne doivent être imprimés ou autrement reproduits sans son autorisation.

---

In compliance with the Canadian Privacy Act some supporting forms may have been removed from this thesis.

Conformément à la loi canadienne sur la protection de la vie privée, quelques formulaires secondaires ont été enlevés de cette thèse.

While these forms may be included in the document page count, their removal does not represent any loss of content from the thesis.

Bien que ces formulaires aient inclus dans la pagination, il n'y aura aucun contenu manquant.

  
**Canada**

# Contents

<b>Contents</b> . . . . .	i
<b>List of Figures</b> . . . . .	iv
<b>List of Tables</b> . . . . .	vii
<b>Acknowledgments</b> . . . . .	viii
<b>Abstract</b> . . . . .	1
<b>1 Introduction</b> . . . . .	2
1.1 Lenticular Galaxies . . . . .	2
1.2 Galaxy Evolution: Environmental Effects . . . . .	3
1.3 Interstellar Gas . . . . .	5
1.4 Interstellar Dust . . . . .	7
1.5 NGC 5866 . . . . .	11
1.6 Motivations and Objectives . . . . .	12
<b>2 Data and Reductions</b> . . . . .	14
2.1 CO Observations and Data Reduction . . . . .	14
2.1.1 Beam Smoothing of $^{12}\text{CO}(3-2)$ Data . . . . .	23

---

<b>2.2</b>	SCUBA Observations and Data Reduction . . . . .	25
2.2.1	SCUBA 850 & 450 micron Images . . . . .	28
2.2.2	CO Emission in the SCUBA 850 Passband . . . . .	33
<b>3</b>	<b>Results: Properties of the Molecular Gas . . . . .</b>	<b>35</b>
3.1	Large Velocity Gradient Models . . . . .	35
3.2	Properties of the Molecular Gas . . . . .	38
<b>4</b>	<b>Results: Origin of the FIR-sub-mm Radiation . . . . .</b>	<b>42</b>
4.1	Single Temperature Models . . . . .	42
4.2	Monte Carlo Model . . . . .	49
4.2.1	Geometries & Parameters . . . . .	50
4.3	Initial Monte Carlo Radiative Transfer Models . . . . .	57
4.4	Further MC Radiative Transfer Models . . . . .	60
4.4.1	Parameter Search . . . . .	61
4.4.2	Monte Carlo Models: Refined . . . . .	69
<b>5</b>	<b>Correlated H<math>\alpha</math> Sub-mm Emission . . . . .</b>	<b>77</b>
5.1	H $\alpha$ to FIR-sub-mm Conversion . . . . .	82
5.2	IR-cirrus Dust Mass . . . . .	88
<b>6</b>	<b>Summary &amp; Conclusions . . . . .</b>	<b>93</b>
<b>Appendix A: CO Spectral Reductions . . . . .</b>		<b>100</b>
<b>Appendix B: CO Simplex Method . . . . .</b>		<b>102</b>

---

<b>Appendix C: LVG Model and Tests . . . . .</b>	<b>105</b>
<b>Appendix D: SCUBA Data Reductions . . . . .</b>	<b>107</b>
<b>Appendix E: Simulated SED Fit to Optical &amp; FIR Data . . . . .</b>	<b>115</b>
<b>Appendix F: Model Images . . . . .</b>	<b>119</b>
<b>References . . . . .</b>	<b>136</b>
<b>Curriculum Vitae . . . . .</b>	<b>142</b>

---

# List of Figures

2.1	$^{12}\text{CO}(2 - 1)$ Emission Line . . . . .	19
2.2	$^{13}\text{CO}(2 - 1)$ Emission Line . . . . .	19
2.3	$^{12}\text{CO}(3 - 2)$ Emission Line at GC Offset $3.2'', -2.5''$ . . . . .	20
2.4	$^{12}\text{CO}(3 - 2)$ Emission Line at GC Offset $8.7'', -6.8''$ . . . . .	20
2.5	$^{12}\text{CO}(3 - 2)$ Emission Line at GC Offset $14.2'', -11.1''$ . . . . .	21
2.6	$^{12}\text{CO}(3 - 2)$ Emission Line at GC Offset $3.2'', -11.1''$ . . . . .	21
2.7	$^{12}\text{CO}(3 - 2)$ Emission Line at GC Offset $14.2'', -2.5''$ . . . . .	22
2.8	450 micron Image of NGC 5866 . . . . .	31
2.9	850 micron Image of NGC 5866 . . . . .	31
2.10	450 micron Contour Map Over V-band Image . . . . .	32
2.11	850 micron Contour Map Over V-band Image . . . . .	32
3.1	$^{12}\text{CO}$ and $^{13}\text{CO}$ (2 - 1) Overlay . . . . .	37
3.2	LVG Models . . . . .	39
4.1	Single Temperature Dust Model . . . . .	48
4.2	Simulated SED for Extended Dust . . . . .	58
4.3	Simulated Images of NGC 5866 . . . . .	59
4.4	Model FIR Predictions . . . . .	65

---

4.5	Model SCUBA 450 $\mu\text{m}$ Flux Predictions . . . . .	66
4.6	Model SCUBA 850 $\mu\text{m}$ Flux Predictions . . . . .	66
4.7	Simulated SED: $h_{z_{dust}} = 100 \text{ pc}$ , $h_{r_{dust}} = 2080 \text{ pc}$ & $M_{bulge} = 0$ . . .	67
4.8	Simulated Images of NGC 5866 . . . . .	68
4.9	$h_{z_{dust}}$ Flux Predictions . . . . .	72
4.10	Simulated Images of NGC 5866 Varying $h_{z_{dust}}$ . . . . .	73
4.11	$h_{r_{dust}}$ Flux Predictions . . . . .	74
4.12	Simulated Images of NGC 5866 Varying $h_{r_{dust}}$ . . . . .	75
4.13	Simulated SED for Extended Dust . . . . .	76
5.1	$\text{H}\alpha$ & Convolved (FWHM = 8") $\text{H}\alpha$ Images . . . . .	80
5.2	Correlation Between 450 $\mu\text{m}$ & $\text{H}\alpha$ . . . . .	80
5.3	$\text{H}\alpha$ & Convolved (FWHM = 15") $\text{H}\alpha$ Images . . . . .	81
5.4	Correlation Between 850 $\mu\text{m}$ & $\text{H}\alpha$ . . . . .	81
5.5	Simulated SED for IR-cirrus Dust Mass $M_{bulge} = 0$ . . . . .	90
5.6	Simulated SED for IR-cirrus Dust Mass $M_{bulge} = 0.44$ . . . . .	91
5.7	Simulated Images for IR-cirrus Dust . . . . .	92
B.1	Simplex Algorithm . . . . .	104
C.2	Comparing LVG Models . . . . .	106
D.3	SCUBA Reduction Procedure . . . . .	109
E.4	Initial Optical SED Fit to Data . . . . .	118
E.5	Deviation in Optical SED Fit . . . . .	118

---

F.6	Simulated Images of NGC 5866: $h_{z_{dust}} = 50$ pc, $h_{r_{dust}} = 580$ pc . . .	120
F.7	Simulated Images of NGC 5866: $h_{z_{dust}} = 50$ pc, $h_{r_{dust}} = 1080$ pc . . .	121
F.8	Simulated Images of NGC 5866: $h_{z_{dust}} = 50$ pc, $h_{r_{dust}} = 1580$ pc . . .	122
F.9	Simulated Images of NGC 5866: $h_{z_{dust}} = 50$ pc, $h_{r_{dust}} = 2080$ pc . . .	123
F.10	Simulated Images of NGC 5866: $h_{z_{dust}} = 100$ pc, $h_{r_{dust}} = 580$ pc . . .	124
F.11	Simulated Images of NGC 5866: $h_{z_{dust}} = 100$ pc, $h_{r_{dust}} = 1080$ pc . .	125
F.12	Simulated Images of NGC 5866: $h_{z_{dust}} = 100$ pc, $h_{r_{dust}} = 1580$ pc . .	126
F.13	Simulated Images of NGC 5866: $h_{z_{dust}} = 100$ pc, $h_{r_{dust}} = 2080$ pc . .	127
F.14	Simulated Images of NGC 5866: $h_{z_{dust}} = 200$ pc, $h_{r_{dust}} = 580$ pc . . .	128
F.15	Simulated Images of NGC 5866: $h_{z_{dust}} = 200$ pc, $h_{r_{dust}} = 1080$ pc . .	129
F.16	Simulated Images of NGC 5866: $h_{z_{dust}} = 200$ pc, $h_{r_{dust}} = 1580$ pc . .	130
F.17	Simulated Images of NGC 5866: $h_{z_{dust}} = 200$ pc, $h_{r_{dust}} = 2080$ pc . .	131
F.18	Simulated Images of NGC 5866: $h_{z_{dust}} = 300$ pc, $h_{r_{dust}} = 580$ pc . . .	132
F.19	Simulated Images of NGC 5866: $h_{z_{dust}} = 300$ pc, $h_{r_{dust}} = 1080$ pc . .	133
F.20	Simulated Images of NGC 5866: $h_{z_{dust}} = 300$ pc, $h_{r_{dust}} = 1580$ pc . .	134
F.21	Simulated Images of NGC 5866: $h_{z_{dust}} = 300$ pc, $h_{r_{dust}} = 2080$ pc . .	135

# List of Tables

2.1	CO Line Intensities . . . . .	18
3.1	CO Line Ratios . . . . .	37
4.1	FIR and SCUBA Flux Densities . . . . .	48
4.2	Monte Carlo Model Input Geometries . . . . .	55
4.3	Optical and NIR Flux Densities . . . . .	56
5.1	H $\alpha$ Corrected FIR and SCUBA Flux Densities . . . . .	87

# Acknowledgments

After night of drinking and celebrating the conclusions of many rounds of corrections, I had time to dwell on the many people that have helped me get this thesis done. Even though I might not be able to mention all of them, I am gracious non the less.

First and foremost, I would like to thank Dr. Gary Welch. Gary, you provided me, from beginning to end, with a wealth of knowledge that I will carry with me throughout my career. It was difficult, at times, to communicate from New Mexico to Halifax but we still got the job done. I am sure that my English skill drove you up the wall, however, I hope I walked away with some improvement. I would like to thank the rest of the faculty at SMU. I always felt that everyone cared about my future and I hope to make you proud.

Louise, Ashley, Dave, and Ray. Thank you for all the help and time that you invested in me. The nights at the Dome, Split Crow, Marquee, and Pacifico were some of the best nights of my life! Louise, all I can say is thank you. You had a strong work ethic that I tried to fallow and you new how to have fun when it was time. The few weeks before I left Halifax and the long checklist of things to do before we left was a blast. Long live the Marquee and the nights we had! Ashley, thanks for coming to NMSU and keeping me company. Having you around helps me remember how great Canada really is. I would also like to thank Amy for helping

me with corrections and putting up with me.

Moving to New Mexico had provided me with many new experiences. This school has encouraged me to continue forward when everyone reaches the point of questioning their choice in career. My advisor Dr. Chris Churchill, has provided me with a great thesis project and many opportunities to travel and meet the people in the field. Even though Las Cruces is not the greatest place to live, the school makes worth it.

Of course none of this would have happened if it wasn't for the love and support of my family. They drove me half way across North America to make sure that I continue advancing in my career. My mom, dad and brother thanks everything. Being away from home for so many years can take its toll but knowing that even though you can't see it, the support is always there. Every weekend my dad would ask me if I was ever going to get my thesis done. Well, I think now I can say it is.

# Abstract

Glenn Kacprzak: The Cool Interstellar Medium of NGC 5866

Submitted: August 10th 2005

The nearly edge-on S0 galaxy NGC 5866 is notable for its massive molecular interstellar medium, prominent central dust lane, and large IRAS 100 micron flux. The galaxy is relatively isolated, and neither the kinematics nor morphology of the gas suggests that a merger has taken place. Instead, NGC 5866 may be entering an era of star formation fueled with gas donated by its aging stellar population. Are we seeing a counter example of the popular view that galaxies evolve through mergers? We explore that possibility using multi-transition CO observations and SCUBA (Submillimetre Common-User Bolometer Array) imagery of NGC 5866. We analyze the gas and dust components of the interstellar medium using large velocity gradient (LVG) models, single temperature dust models and a three-dimensional Monte Carlo radiation transfer code.

---

# Chapter 1

## Introduction

### 1.1 Lenticular Galaxies

Lenticular galaxies (S0s) hold the pivotal position on the Hubble tuning-fork diagram (Hubble 1936). The diagram illustrates a sequence of elliptical galaxies with increasing ellipticity (E0–E7) which then evolves into the S0 type galaxy. At type S0, the tuning fork branches into parallel sequences of barred spiral galaxies (SBa–SBc) and unbarred spiral galaxies (Sa–Sc), which are arranged in order of decreasing bulge-to-disk luminosity ratio and decreasing tightness in the winding of the spiral arms.

Upon studying properties of ellipticals, spirals and S0s, one finds that "typical" S0s represent a morphological and gas abundance transition state between spirals and ellipticals. S0s do not have spiral arms, however, are morphologically similar to spirals since they both have disks, bulges and occasionally dust lanes. However, S0s are also similar to ellipticals since both have low gas abundances, low star formation rates (SFR) and consist of old stellar populations. What are the progenitors of S0s if both spirals and ellipticals have similar characteristics? Can spirals evolve into S0s by going through an era of rapid star formation or starburst followed by an era of quiescence or can mechanisms such as ram pressure stripping simply remove all

---

of the gas thereby quenching star formation? Searching for counter examples of a typical S0 galaxy could provide clues into the evolution of S0s in general.

This chapter reviews how local environment influences properties of galaxies, and the properties of ISM in both gas and dust components of galaxies. This thesis will explore the gas and dust properties and edge-on S0 galaxy, NGC 5866, which may be counter example of the typical S0 since it could be entering an era of star formation fueled with gas donated by its aging stellar population.

## 1.2 Galaxy Evolution: Environmental Effects

The origin and evolution of early-type galaxies is one of the most controversial topics in current extragalactic research. The disk S0s share similar morphology to a few elliptical galaxies which have been observed to have disk-like structure and disk-like rotation (Scorza & Bender 1995; Michard 1998; Rix et al. 1999; Naab & Burkert 2001). It is clear that ellipticals and S0s have similar stellar populations, low interstellar medium (ISM) masses and cool temperatures relative to spirals, and relatively low current star formation rates.

The similarities between S0s with spirals and ellipticals has motivated studies of how the local environment plays a role in galaxy morphology. Many possible environmental explanations have been proposed to account for the formation of lenticulars. One idea is that normal spirals are stripped of their gas during galaxy-galaxy interaction or undergo gas consumption via induced star formation during stripping (Spitzer & Baade 1951; Sandage & Visvanathan 1978; Larson, Tinsley, &

---

Caldwell 1980). Another idea is that rapidly moving spirals within galaxy clusters are stripped of their gas by ram pressure induced by passing through a hot intercluster plasma (Gunn & Gott 1972; Melnick & Sargent 1977). Other mechanisms include gas evaporation by a hot intergalactic medium (Cowie & Songaila 1977), and removal of gas by galactic winds (Faber & Gallagher 1976). Those gas removal mechanisms are consistent with observations showing that early-type galaxies become more frequent as their environment becomes more galaxy rich, such as in the Coma and Virgo clusters (Hubble & Humason 1931; Abell 1965; Oemler 1974). Studies show that the fraction of elliptical and S0 especially galaxies increases steadily with increasing galaxy number density (i.e. number of galaxies per unit volume). This is corroborated by a corresponding decrease in the fraction of spiral galaxies (Dressler 1980; Postman et al. 2005). Similar trends have been found for galaxies in less populated groups, but the dependence weakens or disappears when the crossing time is approximately the age of the universe (Melnick & Sargent 1977).

On the other hand, a mechanism such as ram-pressure stripping by hot plasma would not apply to early-type galaxies outside of rich clusters. Low velocity encounters between spirals are characteristic of lower density clusters where S0s are also found. At these low velocities, it is more likely for an encounter to result in a merger instead of the removal via stripping of the interstellar medium (ISM). Ideally, one should study isolated S0s since their environment has little or no evolutionary influence.

---

## 1.3 Interstellar Gas

Molecular gas is important because molecular clouds are the immediate progenitors of star formation, so there is a strong link between the physical conditions in molecular clouds and star formation. Studies of both far-infrared (Knapp et al. 1989) and  $H\alpha$  emission (Plana et al. 1998) indicates that some S0s are indeed undergoing star formation. Star-formation in S0s is an obvious mechanism for removing gas especially in isolated S0s. By comparing the physical properties of the ISM in S0s to other Hubble types, we will be able to see if lenticulars have typical ISM properties of star forming spirals.

Early-type galaxies were originally believed to have relatively little ISM and negligible star formation rates. The idea that S0s should be devoid of gas was first disputed by Faber and Gallagher (1976), who estimated that gas shed by dying stars could contribute  $\sim 10^{10} M_{\odot}$  in the case of NGC 5866. Unless there are mechanisms for removing the gas from the galaxy, such as star formation or galactic winds, the gas should be observable. Numerous groups (e.g. Wiklind & Henkel 1989; Sage & Wrobel 1989; Knapp et al. 1989) have verified that some S0s do, in fact, contain a cool ISM, but typically much less than the amount predicted by the simple arguments of Faber and Gallagher. In many cases only upper limits for the masses of molecular and/or atomic hydrogen have been observationally determined.

Observations of gas kinematic in some S0s suggest that gas has been accreted from external sources. The strongest evidence is the presence of ionized gas which is counter-rotating with respect to the stars in 40 percent of a 15-member sample

---

of S0s (Bertola, Buson & Zeilinger 1992). Counter rotation is impossible to explain assuming an internal origin of the gas. Van Driel and Van Woerden (1991) also found that the HI distribution in S0s is often highly inclined, from 25 to 55 degrees with respect to the stellar plane, and that the gas is located in an inner and/or outer rings. It has been proposed that the most likely scenario for the creation of an outer ring is a not-too-recent accretion of another gas rich galaxy. Further observations of the interstellar gas are required in order to understand these poorly studied objects. Ciotti & Pellegrini (1996) found that for a sample of early-type galaxies that S0s have a lower mean X-ray luminosity per unit optical luminosity than ellipticals. They also found correlations between the X-ray properties and the axial ratios, where spherical systems have the highest X-ray luminosity to optical luminosity ratio. That trend holds for S0s and Es. Their models show that rotation cannot induce a change in the flow of the hot gas independently of the galaxy shape. Flattening by rotation could reduce the gas binding energy, implying that S0s and non-spherical Es are less likely to retain a significant halo of hot X-ray gas.

Molecular hydrogen ( $\text{H}_2$ ) is the most abundant molecule in the ISM. Unfortunately, the  $\text{H}_2$  molecule is symmetric and therefore has zero permanent dipole moment, so that none of the mm-wave rotational and vibrational transitions that make other molecules easy to detect can be observed. As a result a tracer molecule such as  $^{12}\text{CO}$  is used to study the large-scale molecular ISM in other galaxies. CO is believed to be a good tracer for  $\text{H}_2$  since both form in cool regions of  $T \leq 1000$  K. CO has a 'fundamental'  $J = 1-0$  rotational transition at 115.2712 GHz and higher-level

transitions at higher frequencies.

The distribution of molecular clouds varies between Hubble types. In disk galaxies the CO is typically concentrated in clumpy regions tracing the ridges of the spiral pattern, although central concentrations in early-type spirals and starburst systems are common as well. In early-type galaxies, the CO tends to be concentrated in the central regions within  $0.1D_{25}$  (Tacconi et al. 1991; Welch & Sage 2003), where  $D_{25}$  is the observed diameter for an isophote of blue luminosity of 25 mags/arcsec<sup>2</sup>. Measurements of atomic hydrogen in early-type galaxies are few; mostly upper limits have been set. Of the known measurements, some indicate that the  $M_{H_2}/M_{HI}$  mass ratio is roughly 0.44 (Henkel & Wiklind 1997), while others find it to vary between 0.1 and 30 (Van Driel & Van Woerden 1991). The latter range covers the known range for spirals which on average is 2 (Casoli et al. 1998). In irregular galaxies, the interstellar medium is clumpy and is apparently dominated by atomic hydrogen, rather than molecular hydrogen.

## 1.4 Interstellar Dust

The interplay between gas and dust and being able to measure their relative abundances can reveal how S0s are related to other galaxy morphological types. Dust is responsible for most of a normal galaxy's far infrared (FIR)–sub-mm radiation. Dust grains are heated by absorbing blue and UV starlight and re-radiating in the FIR–sub-mm. That process plays a major role in shaping the galaxy spectral energy distribution (SED). The amount of dust, blue, and UV starlight govern the

output flux that is observed.

The gas-to-dust mass ratio of the ISM for the Milky Way has been measured to be 100 (Knapp & Kerr 1974), and this value has been used in most extragalactic work. Using the measured gas mass and the assumed ratio one can estimate the expected dust mass. However, the average lower limit of the ratio for S0 galaxies is around 800 to 1600 where only upper limits to the mass of HI have been measured (Thronson et al. 1989; Fich & Hodge 1993). These discrepancies illustrate why a study of the ISM is not complete without investigating directly the properties of the interstellar dust.

Dust can be observed in blue and UV absorption and far-infrared (FIR) emission. The FIR flux is often assumed to come from dust being heated by hot OB stars, which are believed to be embedded in dusty molecular clouds, making FIR emission a potential indicator of the star formation rate. The IRAS survey data showed that FIR emission is present in all types of galaxies, even early types for which optical data suggested only a modest amount of dust (Jura 1986).

A portion of the FIR flux, however, also comes from IR-cirrus. The term "IR-cirrus" refers to a population of widely distributed grains heated by the general interstellar radiation field. Since IR-cirrus is clearly a source of FIR emission in galaxies, one should be careful when using FIR flux to trace star formation. It is important to realize that the diffuse old background stellar population can be responsible for a majority of IR measurements especially in early type galaxies. Thronson and Bally (1987) find that 2/3 of their sample of early type galaxies have expected IRAS

---

colors,  $Flux_{12\mu m}/Flux_{25\mu m}$  and  $Flux_{60\mu m}/Flux_{100\mu m}$ , consistent with IR-cirrus as apposed to star formation. If the ratio  $Flux_{60\mu m}/Flux_{100\mu m}$  is greater than 0.45, more than half of the the inferred flux is contributed by star forming regions (Helou 1986).

Dust grains responsible for most of the FIR-sub-mm radiation are heated by absorbing blue and UV starlight whose wavelength approaches the characteristic grain size. Those grains radiate like black bodies modified by a wavelength-dependent emissivity, a behavior caused by the fact that the grains are smaller than the peak blackbody wavelength (around 100 microns) and thus cannot radiate at such wavelengths as efficiently as a perfect blackbody. Complete interpretation of the UV-optical-IR energy balance is difficult because it requires knowledge of the distribution of stellar types, grain population and grain size distribution. Dust temperatures,  $300\text{ K} > T_{dust} > 20\text{ K}$ , are usually attributed to different regimes of heating such as OB stars environments, regions near cooler stars, and the infrared cirrus emission.

Other potentially observable consequences of diffuse dust are radial optical color gradients. In most cases, early-type galaxies display redder colors toward the center. Those color gradients are usually interpreted as caused by variations in the metallicity within the stellar population. However, there is some scatter in the relationship of color gradients and metal line strength gradients (Davies, Sadler, & Peletier 1993), and it remains possible that dust extinction also creates a part of these color gradients. By studying color gradients one hopes to understand the mass and distribution of dust. Witt, Thronson and Capuano (1992) have shown that real-

---

istic distributions of diffuse dust in early type galaxies can produce color gradients. Their model is based on a uniform distribution of dust over a symmetric stellar population and incorporates a Monte-Carlo multiple-scattering radiative transfer code. Goudfrooij and de Jong (1995) have applied the same model to their optical and IRAS data, finding that the observed color gradients were always at least as large as those of the model. That strongly suggests differential extinction from a diffuse dust distribution in early-type galaxies causes at least part of the observed color gradients. Goudfrooij and de Jong investigated whether the assumption of a diffuse dust component uniformly distributed over the galaxy could be energetically consistent with IRAS data. They discovered that for almost all elliptical galaxies in their sample, the IRAS data could be reproduced within one-sigma uncertainty by assuming only two dust components: an optically visible dust lane and/or patches, and a component diffusely distributed within the inner few kpc. Dust heated by optical photons from the general stellar population was usually sufficient to account for the observed dust temperatures. Goudfrooij and de Jong's work agrees with the results of Thronson and Bally (1987) who conclude that 23 of a larger sample of early-type galaxies have IRAS color characteristics of IR-cirrus.

It might be possible to determine if the dust in a galaxy is heated by newly forming stars or by the general stellar population. If so then this could provide an independent means of determining the importance of star formation inside a given galaxy.

## 1.5 NGC 5866

The main focus of this study is the edge-on  $S0_3$  galaxy NGC 5866. The galaxy is located within the sparse NGC 5907 group at a distance of 15.3 Mpc (Tully & Fisher 1987). NGC 5866 is a known X-ray source and has been observed by the EINSTEIN satellite. The luminosity of  $6.26 \times 10^{39}$  ergs  $s^{-1}$  between 0.5–4.5 keV, results in a hot gas mass of  $2.38 \times 10^8 M_{\odot}$  (Fabbiano et al. 1992). It is a moderately strong IRAS source and contains  $4.39 \times 10^8 M_{\odot}$  of molecular gas (Welch & Sage 2003) that probably coincides with its prominent central dust lane. The molecular gas mass was determined from CO J= 1–0 multi-single point observations of NGC 5866 using the IRAM 30m telescope. A spectrum was first obtained in the center of the galaxy and additional positions along the major axis were observed at 10'' steps until no emission was observed. In NGC 5866 CO J= 1–0 was observed over the entire extent of the optical component out to 50'' from the center of the galaxy. Curiously, there has been no detection of HI 21 cm emission and the upper limit is  $M(HI) \leq 1.2 \times 10^8 M_{\odot}$  at the one-sigma level (Sage & Welch 2005). The dust lane has an inclination of 2–5 degrees from the optical major axis and is roughly 2 to 3 arcseconds thick (Burbidge & Burbidge 1960). Star formation within the dust lane is evident from  $H\alpha$  emission (Plana et al. 1998), which implies a star formation rate of  $0.243 M_{\odot} \text{yr}^{-1}$ . Stellar recycling should have contributed  $1.98 \times 10^{10} M_{\odot}$  of gas and dust which is roughly 45 times more than observed (Welch & Sage 2003). The mean gas return rate over the past 10 Gyr would result in a star formation rate of  $2 M_{\odot} \text{yr}^{-1}$  which is higher than the current star formation

---

rate. That is consistent with the idea that stars could have built up the observed molecular gas supply. NGC 5866 is a prime candidate for a study of the ISM in a fairly normal S0; it is relatively isolated and thus not likely to have been influenced by an ambient intergalactic medium, and it does not seem to have undergone any recent interactions. Choosing an isolated S0 decreases the possibility that the local environment has influenced its evolution

## 1.6 Motivations and Objectives

This thesis contains an analysis of the cool ISM in the S0<sub>3</sub> galaxy NGC 5866. The tasks at hand are to determine the physical conditions in the molecular gas, and to attempt to identify the heating sources responsible for the FIR emission.

Data obtained from the IRAM 30m and JCMT 15m telescopes will be used to study the gas component. Those telescopes provide a unique opportunity to directly compare the intensities of different CO transitions, since the IRAM beam size at the frequency of the  $J = 1-0$  transition is very similar to that of the JCMT at the frequency of the  $J = 2-1$  transition. JCMT observations of the  $^{12}\text{CO}(3-2)$  transition will also be used, but only after making beam size corrections. With these data, it is possible to determine the mass of H<sub>2</sub> (Welch & Sage 2003), and the physical conditions of the molecular clouds in the area observed.

The dust component will be investigated with data from IRAS, and the JCMT SCUBA instrument that is used at wavelengths 450 and 850 microns. SCUBA has imaging capabilities and is also sensitive to cooler gas than is IRAS. The images will

---

provide information on the quantity and the distribution of dust in the galaxy.

Single-temperature dust models, similar to Fich and Hodge (1991), are used to obtain crude dust mass estimates. A three-dimensional Monte Carlo radiative transfer code obtained from Kenneth Wood is used to simulate optical and SCUBA images of NGC 5866. By comparing observed and simulated images we will attempt to determine the morphology of the dust, and thus identify the likely heating sources. An additional constraint is provided by comparing the observed and model optical-to-mm spectral energy distributions.

The main objective in the SCUBA study is to find out if IR-cirrus, especially in the elliptical-like bulge of NGC 5866, is an important source of its FIR-sub-mm emission. A large inferred diffuse dust mass would support the dust-based interpretation of color gradients in E, S0 galaxies.

So what has removed most of the gas returned by the aging stellar population in NGC 5866? Do physical conditions inside its molecular gas lead to expectations of higher future SFRs? NGC 5866 may be entering an era of star formation fueled with gas donated by its aging stellar population. Are we seeing a counter example of the popular view that galaxies evolve through mergers? We will attempt to answer these questions by understanding the physical conditions of the ISM which will help differentiate between quiescent and active star forming environments.

## Chapter 2

# Data and Reductions

### 2.1 CO Observations and Data Reduction

Single-point spectra for the  $J = 2-1$  transitions of  $^{12}\text{CO}$  and  $^{13}\text{CO}$  were obtained using the James Clerk Maxwell Telescope (JCMT) on 2001 December 20–21 as part of Canadian program M01B/C04. An additional five-point map of  $J = 3-2$  transition for  $^{12}\text{CO}$  was obtained in 2002 April 26, CANSERV program S01B/C05. Receiver A3 was used for the  $J = 2-1$  transitions and receiver B3 was employed for  $J = 3-2$ . The Digital Autocorrelation Spectrometer (DAS) was used in wideband mode to provide a 1800 MHz passband, equivalent to  $2300 \text{ km s}^{-1}$  and  $1600 \text{ km s}^{-1}$  for  $\text{CO}(2-1)$  and  $\text{CO}(3-2)$ , respectively, since earlier CO observations of NGC 5866 indicated that the linear line width is of the order of  $600 \text{ km s}^{-1}$ . The JCMT main beam is assumed to have a  $FWHM = 21''$  for the  $J = 2-1$  transitions and a  $FWHM = 14''$  for the  $J = 3-2$  transition. All the data were taken with beam switching in azimuth using a throw of  $180''$  at 1 Hz. Pointing and focus were monitored regularly by observing IRC+10216 and two stars X Her and RX Bootis, the former is believed accurate to 2–3 arcseconds. For the  $J = 2-1$  observations, the telescope was pointed at an offset of  $R.A = 8.67''$  and  $DEC = -6.77''$  from the center of NGC 5866, assumed to be at  $R.A = 15^{\text{h}}12^{\text{m}}07^{\text{s}}.0$ ,  $DEC = +55^{\circ}57'20''.0(1950.0)$ . The offset was chosen

based on observations of Welch and Sage (2003), which show that the strength of the  $^{12}\text{CO}(1-0)$  emission reaches maximum at that location.

Intensity ratios can be used to deduce the physical conditions of the molecular gas in the observed area. The ratios are only meaningful when the CO intensities ( $I_{CO}$ ) are deduced from the same beam size, since different size beams sample different areas of the source. The frequencies of the  $^{12}\text{CO}(2-1)$  and  $^{13}\text{CO}(2-1)$  transitions differ by only  $\sim 4\%$  and are assumed to refer to the same beam size. Since, however, the  $^{12}\text{CO}(3-2)$  beam size is much smaller than that at  $\text{CO}(2-1)$ , a five-point map of  $^{12}\text{CO}(3-2)$  was made in order to be able to compare the intensities of the two transitions. Three measurements of the five-point map were taken along the major axis of the galaxy orientated at a position angle of 128 degrees with a spacing of 7 arcseconds. Two other measurement were taken on each side of the minor axis which was orientated at a position angle of 38 degrees. The center pointing was located at the offset specified above.

The JCMT SPECKX software package was used to reduce the data. A linear baseline was removed from each scan, which was then averaged with corresponding scans to produce a final spectrum for each transition. The total baseline intervals are  $1600 \text{ km s}^{-1}$  and  $800 \text{ km s}^{-1}$  for the  $\text{CO}(2-1)$  and  $\text{CO}(3-2)$  respectively. The integrated CO intensity,  $I_{CO}$ , was determined by

$$I_{CO} = \int \frac{T_A^*}{\eta_{MB}} dV \quad (2.1)$$

where  $T_A^*$  (Kutner & Ulich 1981) is the antenna temperature, and  $\eta_{MB}$  is the telescope's main beam efficiency, and the integration extends over the velocity limits of the line. The main-beam efficiency is 0.63 for B3 and 0.69 for A3 receivers as stated in the JCMT User's Guide. A more complete description of the data reduction method is given in Appendix A.

The  $J = 2-1$  and the  $J = 3-2$  spectra are binned to a resolution of 21.7 km s<sup>-1</sup> and 32.5 km s<sup>-1</sup> respectively. Uncertainties in  $I_{CO}$  were determined by the quadratic sums of the uncertainties due to random noise in the line spectrum and in the determination of the baseline level (Sage 1990). The uncertainty due to the random noise across the line is determined by,

$$\Delta I_l = T_{rms} \times \Delta v_i \times \left[ \frac{\Delta v_c}{\Delta v_i} \right]^{1/2} \quad (2.2)$$

where  $T_{rms}$  is the root mean square noise per channel of smoothed baseline (Table 2.1, column 5),  $\Delta v_i$  is the velocity width of the line window, and  $\Delta v_c$  is the smooth channel width. The error from the uncertainty in determining the baseline of the spectra is,

$$\Delta I_b = T_{rms} \times \Delta v_i \times \left[ \frac{\Delta v_c}{\Delta v_b} \right]^{1/2} \quad (2.3)$$

---

where  $\Delta v_b$  is the velocity width of the baseline. The CO intensities are in Table 2.1 and Figures 2.1–2.7 show the reduced spectra for each transition at the pointing specified where the assumed emission line width is underlined.

Table 2.1: CO Line Intensities

Transitions	Offset (")	<i>FWHM</i> (")	$I_{CO}$ (K km s <sup>-1</sup> )	rms (mK)
<sup>12</sup> CO				
1 – 0 <sup>a</sup>	8.7, -6.8	21	28.06 ± 0.37	2.98
2 – 1	8.7, -6.8	21	20.72 ± 2.05	15.9
3 – 2	3.2, -2.5	14	15.71 ± 2.62	19.0
	8.7, -6.8	14	5.87 ± 2.54	17.5
	14.2, -11.1	14	1.21 ± 0.95	11.1
	3.2, -11.1	14	4.92 ± 1.75	12.7
	14.2, -2.5	14	6.14 ± 1.30	11.1
Convolved 3 – 2 <sup>b</sup>	8.7, -6.8	21	6.10 ± 2.56 <sup>c</sup>	–
<sup>13</sup> CO				
2 – 1	8.7, -6.8	21	2.44 ± 0.41	3.17

<sup>a</sup>Data obtained by Welch & Sage (2003) at the IRAM 30m telescope

<sup>b</sup>Determined as explained in the text

<sup>c</sup>Uncertainty determined by the quadratic sums of the mean uncertainty of the five pointings and the standard deviation produced by the Simplex Method

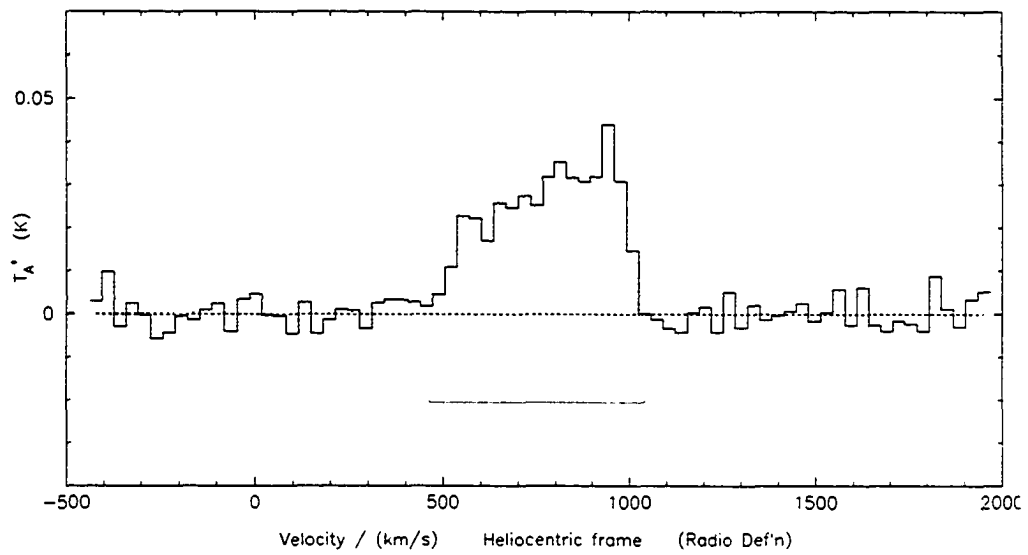


Figure 2.1: Fully reduced  $^{12}\text{CO}(2-1)$  transition which was observed at the offset listed in Table 2.1. The emission linewidth is underlined.

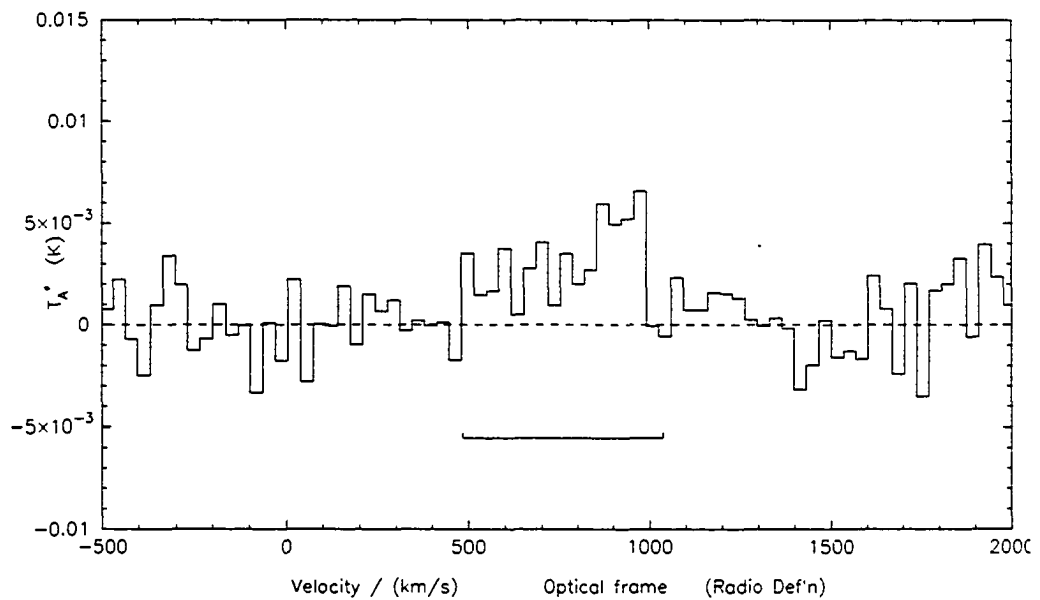


Figure 2.2: Same as previous except for the  $^{13}\text{CO}(2-1)$  transition.

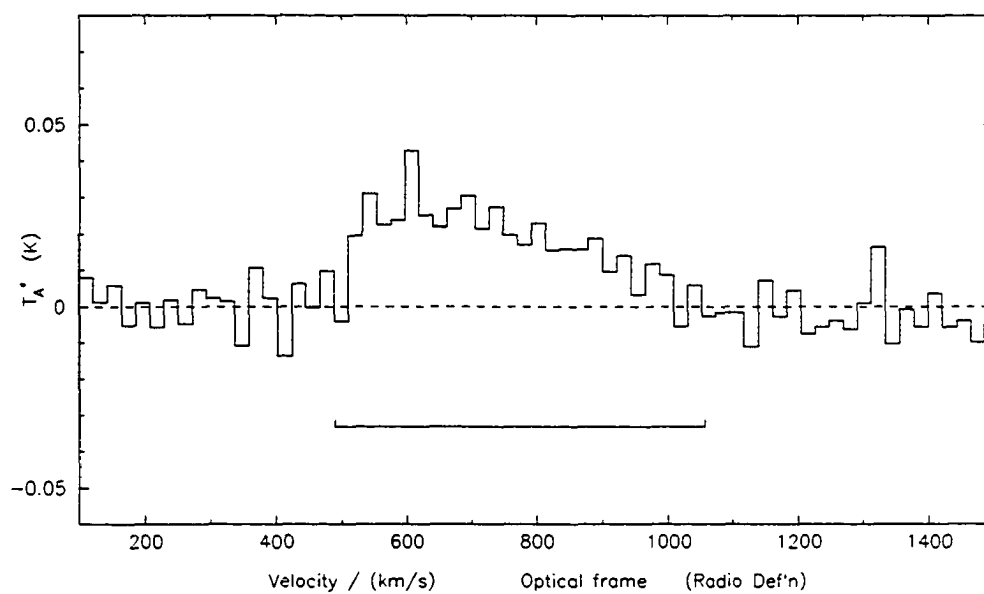


Figure 2.3: One of the five pointings for the  $^{12}\text{CO}(3-2)$  transition. Emission line at an offset of  $3.2'', -2.5''$ .

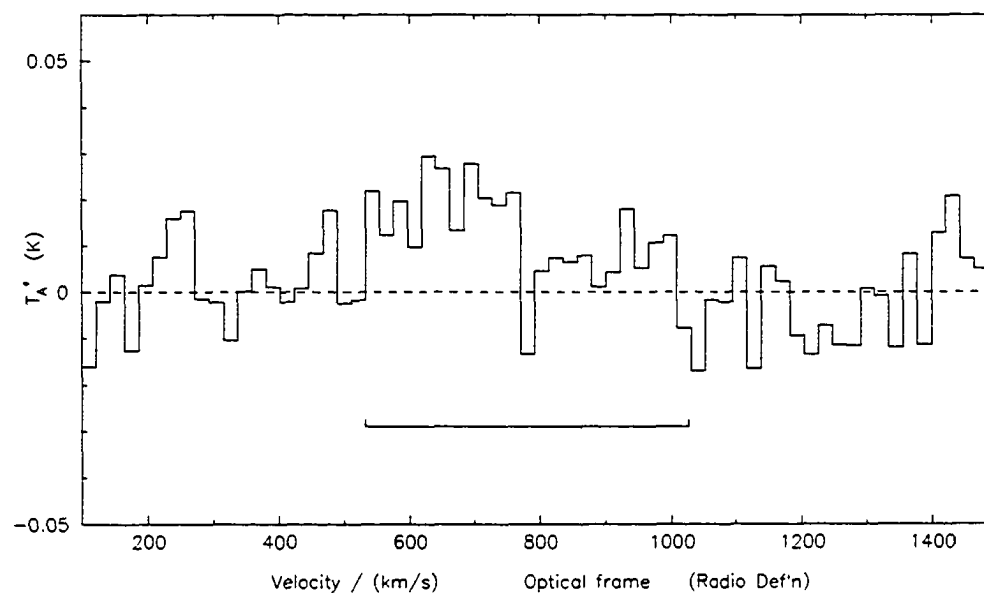


Figure 2.4: Same as previous but taken at an offset  $8.7'', -6.8''$ .

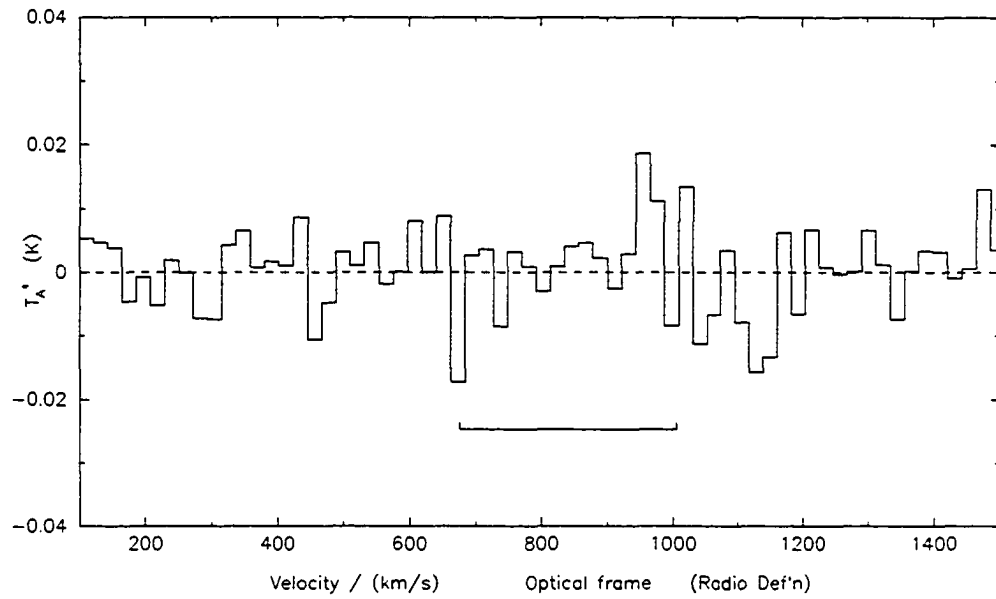


Figure 2.5: Same as previous but taken at a an offset of  $14.2''$ ,  $-11.1''$ .

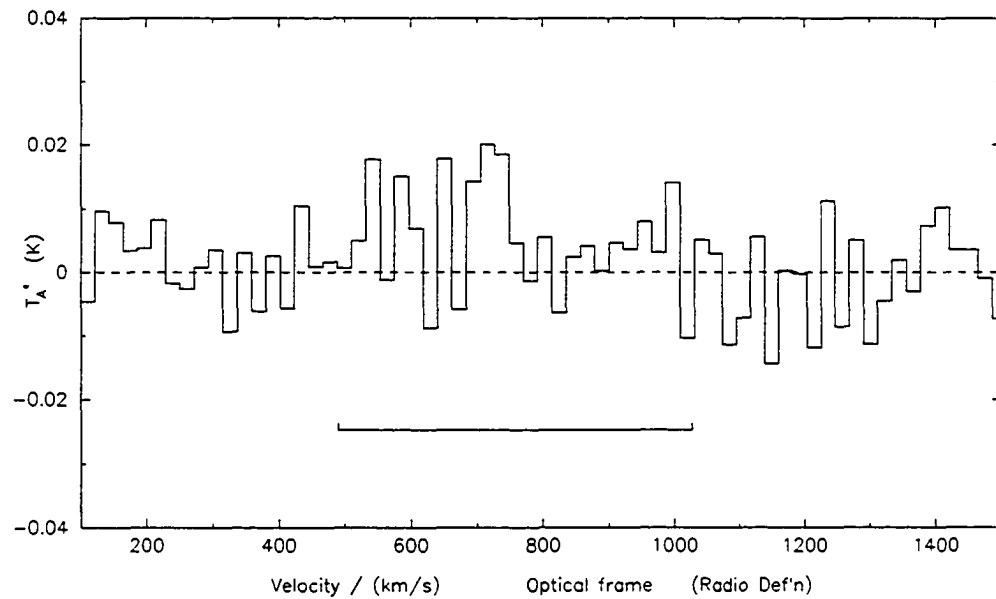


Figure 2.6: Same as previous but taken at a different offset of  $3.2''$ ,  $-11.1''$ .

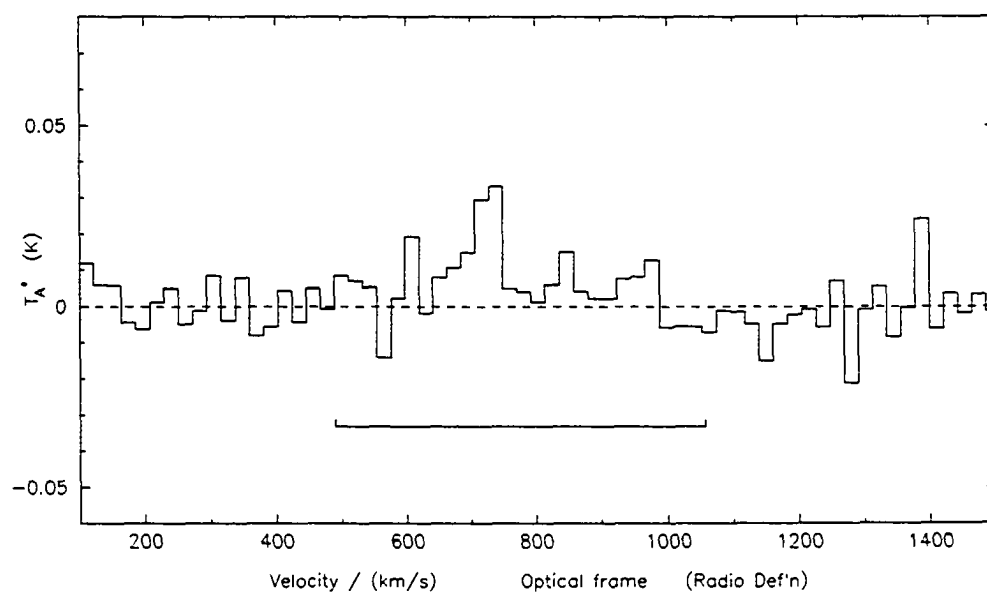


Figure 2.7: Same as previous but taken at a different offset of  $14.2''$ ,  $-2.5''$ .

### 2.1.1 Beam Smoothing of $^{12}\text{CO}(3 - 2)$ Data

The next step is to smooth the  $^{12}\text{CO}(3 - 2)$  beam resolution so that the intensities can be directly compared to those of the other transitions. It is worth noting that  $^{12}\text{CO}(2 - 1)$  and  $^{13}\text{CO}(2 - 1)$  show similar line shape and line width. Both have a line width of around  $600 \text{ km s}^{-1}$  and a maximum intensity around  $900 \text{ km s}^{-1}$ . However, the  $^{12}\text{CO}(3 - 2)$  displays slightly different line shapes as seen in Figure 2.3 where for this particular pointing the line shape is opposite to that of the other transitions. The remaining pointings possibly display similar line widths but their kinematic properties are difficult to see since they are at lower signal-to-noise. The kinematics differences are puzzling which could suggest errors in telescope pointing, even though the pointing was checked, all the data for each transition were taken on different dates. The differences could also arise if we are not looking at the same region of gas with the  $^{12}\text{CO}(3 - 2)$  transition as we are with the other transitions. Both scenarios are possible and cannot differentiate between the two unless more  $^{12}\text{CO}(3 - 2)$  maps are made.

A map of  $^{12}\text{CO}(3 - 2)$  emission was taken in order to convolve these data to the lower spatial resolution of the  $(2 - 1)$  data. While this technique bypasses the need for uncertain filling factor corrections, it requires assuming a source geometry. It has been assumed here that the source is a two-dimensional Gaussian and that it is centered on the pointing with the maximum measured  $^{12}\text{CO}(3 - 2)$  intensity. Using the  $\text{CO}(3 - 2)$  data and given the assumption of the source geometry, we can artificially "observe" the source and vary its fitting parameters in order to best fit

the observed five-point map. Once the shape of the source is fixed, it can then be artificially observed with any chosen beam.

The maximum CO(3–2) intensity is at an offset of  $R.A. = 3.2''$ ,  $DEC = -2.5''$  from the center of NGC 5866. That however, is not the center of our five point map as was expected from previous J= 1–0 observations (Welch & Sage 2003). Since the exact position of the intensity peak is unknown, the assumption that the true maximum occurs at offset of  $R.A. = 3.2''$ ,  $DEC = -2.5''$  is uncertain which introduces added uncertainties to our procedure. The only way to resolve this problem is by acquiring a large source map.

Assuming a Gaussian shape and fixing the peak location at the offset of  $R.A. = 3.2''$ ,  $DEC = -2.5''$  leaves three free parameters for the source shape: the amplitude (i.e the peak intensity) and the source width in both  $x$  ( $\sigma_x$ ) and  $y$  ( $\sigma_y$ ) which are in the major and minor axis directions, respectively. To artificially observe the source a Gaussian telescope beam of  $FWHM = 14''$  was convolved with the synthetic source to simulate the observed line intensity which can be compared to the actual data. The Simplex Method was used to find the best-fit parameters. That method is a variation of the process of minimizing the Chi squared, in which the parameter space is searched until a best-fit to the observations is obtained. The basic algorithm and details of the Simplex model can be found in Appendix B. The solution-space was assumed to be smooth and without local-minima. Under those assumptions one would expect that there exists a unique solution. However, the Simplex was given various starting values in solution-space to quantify the accuracy of that assumption.

The fitting process yields an amplitude or peak intensity of  $346.15 \pm 33 \text{ K km s}^{-1}$ , a  $\sigma_x$  and  $\sigma_y$  of  $0.21 \pm 0.02''$  and  $7.462 \pm 0.007''$ , respectively. The uncertainties are the standard deviations in the output values corresponding to different values to the starting Simplex. The  $^{12}\text{CO}(3-2)$  source recovered here is very small so in the next section we will be looking at physical conditions in only a small fraction of the galaxy's total CO which may or may not be representative of the average conditions found in NGC 5866.

The source defined by the above procedure was convolved with a  $FWHM = 21''$  Gaussian beam to give an integrated intensity of  $6.10 \pm 2.56 \text{ K km s}^{-1}$ . The uncertainty is determined by the quadratic sums of the mean uncertainty of the five pointings and the standard deviation produced by the Simplex Method. That intensity can now be directly compared with the other  $J = 2-1$  and  $J = 1-0$  intensities, as required by Large Velocity Gradient (LVG) modeling. The modeling will be discussed in the next chapter.

## 2.2 SCUBA Observations and Data Reduction

Continuum jiggle-maps of NGC 5866 were obtained at 450 and 850 microns at the JCMT using the SCUBA instrument on 2001 December 20th and 22nd, as a part of program M01B/C34. The telescope  $FWHM$  at those wavelengths is  $8''$  and  $15''$ , respectively. All the data were taken by beam switching in azimuth using a throw of  $180''$ . Pointing and focus were monitored regularly by observing IRC+10216 and 1418+546 and should be accurate to within 2 arcseconds. Instrument noise

measurements were regularly taken to permit identification of bad bolometers.

Two programs were used for data reduction. The pipeline tool ORAC-DR was used to get a first look at the images. A complete reduction was performed using SURF. The following is a summary of the SURF data reduction; a more complete description of the reduction is provided in Appendix D.

Each integration of 10 minutes must be reduced separately; all are grouped together at the end of the reduction process. The first step is to remove the variance of the sky using the REDUCE\_SWITCH task. The task takes the off-source data obtained when chopping and removes a median value from the source signal. The data is then flat-fielded using FLATFIELD, following which it is necessary to correct for the atmospheric attenuation.

The zenith sky opacity  $\tau_{CSO}$ , at 225 GHz, is obtained from the CSO sky monitor, which takes measurements every ten minutes. The latest available relationships between  $\tau_{CSO}$ ,  $\tau_{850}$  and  $\tau_{450}$  (see Appendix D) is used to find the sky opacity at 450 and 850 microns. The task EXTINCTION is used once zenith opacity is determined. Since their sky opacities differ, the long and short wavelength data sets are separated at that point and reduced independently thereafter. The next step identifies and discards any bolometers that were noisy during the observation period.

Noisy bolometers are identified using the command SCUNOISE, which displays the readings of each bolometer during the noise measurements. There are 37 and 91 bolometers in the long and short wavelength arrays, respectively. The majority of the bolometers should have a typical noise level around 40 nV (SCUBA Users

Guide). Bolometers are deemed too noisy if their output is above 100 nV, and any pixel with a noise level of over 500 nV is normally removed. Bolometers that are noisy throughout the observing run can be removed using the `CHANGE_QUALITY` command. Rotation of the night sky during data acquisition ensures that missing bolometers produce no 'holes' in the final map. A total of two sky bolometers were removed from the 850 micron data set for both observing nights. The 450 data was very noisy on the second night and 16 bolometers were removed, whereas only one bolometer was removed in data from the first night.

To ensure an accurate sky subtraction, an initial `DESPIKEing` was done at the  $5\sigma$  level to remove any spikes in the data set. The sky bolometers must be identified before the sky can be removed. Sky bolometers are those that observe the sky during one 64 point jiggle map. Since the source is extended and faint, care must be taken in choosing the sky bolometers. The task `SCUOVER` is used to overlay the bolometer positions on the maps. Once the sky bolometers are chosen, the task `REMSKY` is used to remove the sky signal from the data.

A final group despiking (`DESPIKE NOLOOP`) at the  $3\sigma$  level was performed. The task compares all the maps made in one observing night and cuts out spikes higher than the cutoff. The despiked data can then be `REBINed` to create a final reduced map of all the data acquired for one night. This completes the necessary data reduction for one night.

The source IRC+10216 was used to calibrate the SCUBA maps at both wavelengths. The uncertainties in the calibration, added in quadrature with the variance

---

of the fluxes determined for each individual night, represents the uncertainty in the total flux of NGC 5866. The maps for each observation night were weighted according to the total integration times of 30 minutes on the 20 Dec and for 60 minutes on the 22 Dec, and were then added to produce the final calibrated map.

### 2.2.1 SCUBA 850 & 450 micron Images

The final maps are displayed without contours in Figures 2.8 and 2.9 and as contours over a V-band image obtained at l'observatoire de Mont Megantic in Figures 2.10 and 2.11. The SCUBA images are noisy around the edges which is a natural consequence of the jiggle-map mode. Dead space between the bolometers causes the outer regions of the image to be under sampled and results in a rough and noisy outer ring.

The galaxy is optically thin at the wavelengths observed by SCUBA so all the cool dust in the galaxy can be seen. The SCUBA maps in Figures 2.8 and 2.9 show slightly different morphology. The 450 micron image is very flat and disk-like, similar to that of the dust lane, whereas the 850 micron image is more bulgy in the center. Are we looking at a two component disk and bulge dust distributions or are the different morphologies just a result of different beam sizes? Is there an appreciable amount of dust in the bulge of the galaxy or is most of it concentrated in the disk? Only with models can one determine the possible distributions of the dust in the galaxy. Dust morphology at 450 and 850 microns will be explored in Chapter 5.

---

The contour plots in Figures 2.10 and 2.11 show the similarities between the optical and SCUBA images. NGC 5866 has a prominent optical dust lane (see Figure 2.10) and due to the resolution of SCUBA, it is difficult to determine if all the emission is coming from the dust lane or from a bulge component as well. The 450 micron map is disk-like and is coincident with the optical dust lane where that dust may reside. The intensity maximum of the 450 map is also coincident with the optical center of the bulge of the galaxy. Similar properties are seen with the 850 micron map overlay. The intensity maximum at 850 microns is located in the center of the bulge of the galaxy. It is difficult to say if the cool gas at 850 microns also resides in the dust lane due to the lower resolution map, however the 850 micron maps semi-major axis is aligned with the dust lane and is symmetric about that axis. The morphology of the dust distribution is also symmetric about the center of the galaxy. There are no major perturbations detected which is consistent with NGC 5866 not having any recent harassments of mergers.

The extent of the dust emission is also consist with the extent of the molecular gas found (Welch & Sage 2003) which might also coincide with the prominent central dust lane.

The total flux of the sub-mm maps were determined via aperture photometry. An elliptical aperture was used to minimize the sky source. The total flux for NGC 5866 at 450 and 850 microns are  $1.75 \pm 0.7$  Jy and  $0.28 \pm 0.03$  Jy respectively. The rms background signal, in the selected sky bolometers, for each image is 0.25 mJy and 0.015 mJy for the 450 and 850 micron images respectively. These fluxes can

now be used along with the IRAS fluxes to determine the total dust mass.

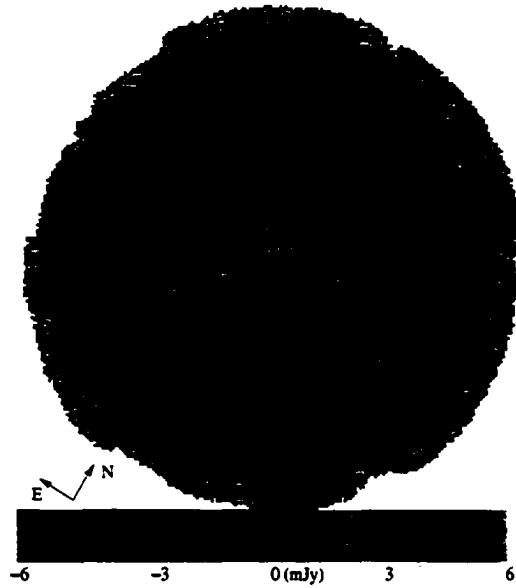


Figure 2.8: False color SCUBA image at 450 microns. The diameter of the image is  $3' 3''$ . A color flux scale is indicated above and is in units of mJy.



Figure 2.9: Same as above except that it is the SCUBA 850 micron image.



Figure 2.10: Optical V-band image of NGC 5866. The contours represent the SCUBA image at 450 micron. The contours are 3, 1.5, 0.75 Jy.

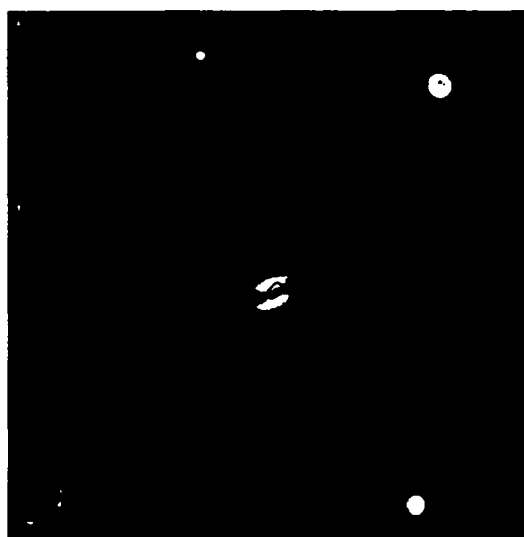


Figure 2.11: Same as above except that the contours represent the SCUBA image at 850 microns. The contours are 0.3, 0.075, 0.0375, 0.0188 Jy.

### 2.2.2 CO Emission in the SCUBA 850 Passband

One must consider the possibility that because the CO(3 – 2) transition has a wavelength of 864.8 microns, emission from this line could seriously contaminate the 850 micron SCUBA map. The flux density contribution from the (3 – 2) transition can be estimated using the line ratio  $R_{32}=[I_{CO(3-2)}/I_{CO(2-1)}]$  and the total observed signal of CO(2 – 1) = 91 K km s<sup>-1</sup> (Welch & Sage 2003). For an ideal antenna the flux density is determined by

$$S_\nu = \frac{2k}{A_p} T_A^* \quad (2.4)$$

where  $k$  is the Boltzmann constant,  $A_p = \pi r^2$  is the physical area of the antenna and  $T_A^*$  is the antenna temperature in Kelvin. Since SCUBA is sensitive over a given bandpass ( with transmission function  $t_\nu$ ), the integrated flux density for the (3 – 2) transition becomes,

$$S_{CO} = \frac{2kt_{CO}}{A_e} \frac{\int_{line} T_A^* d\nu}{\int_{passband} t_\nu d\nu} \quad (2.5)$$

where  $t_{CO}$  is the transmission of the SCUBA filter at 864.8 microns, and  $A_e$  is the effective area of the JCMT at this wavelength. The integral over the CO(3 – 2) line can be determined using  $R_{32}$  and the CO(2 – 1) intensity. Normalizing the equation,

---

yields the following equation which will determine the total CO flux ( $S_{CO}$ ) observed by SCUBA.

$$S_{CO}(Jy) = 8.891 \times 10^{22} \frac{2kt_{CO}}{A_e} \frac{\int_{line} T_A^* d\nu}{\int_{passband} t_\nu d\nu} \quad (2.6)$$

It is found that CO contributes only 22.6 mJy or 8.2% of the total emission. The observed 850 micron flux has therefore not been corrected for CO emission, since such a correction would be comparable to the uncertainty of the calibration.

## Chapter 3

# Results: Properties of the Molecular Gas

### 3.1 Large Velocity Gradient Models

By using models, it is possible to obtain an  $\text{H}_2$  density and gas kinetic temperature from the rotational transitions of CO. The Large Velocity Gradient (LVG) model is rather successful, and has been used in many experiments to determine the physical conditions of molecular clouds (Phillips, White, & Richardson 1985; Li, Seaquist, & Sage 1993; Xie, Young, & Schloerb 1994). The LVG model for radiative transfer in molecular lines was created for the condition of an idealized velocity field  $v_r \propto r$ , where  $r$  is the distance from the center of a spherical emitting cloud (Scoville & Solomon 1974; Goldreich & Kwan 1974). The model is based on the assumption that the emission lines are broadened by the general flow of the gas, i.e. the velocity gradient, and not by the small random motions caused by turbulence. The model deals with local radiative transfer, in which molecular line photons are emitted at some location and can be reabsorbed within a surrounding region whose size is of order the local line width divided by an assumed velocity gradient. Otherwise photons escape from the region due the existence of the systematic velocity shift. It is assumed that the source has uniform physical conditions. The information

---

required to construct an LVG model are measurements of the ratio of intensities of two or more transition lines of any molecule that has been included in the model. The present study uses the three ratios given in Table 3.1. The ability to constrain the properties of the ISM strongly depends on the identity of the transitions in the line ratios.

The LVG code used here was developed by T. Hasegawa in 1991 (see Greaves et al. 1992) and modified by G. Welch in order to create more useful output. We adopt a  $^{12}\text{CO}$  abundance per velocity gradient  $X_{\text{CO}}/(dv/dr) = 1 \times 10^{-5} \text{ pc}/(\text{km s}^{-1})$  (eg: Wilson, Howe, & Balogh 1999; Li, Seaquist, & Sage 1993) and the  $^{12}\text{CO}/^{13}\text{CO}$  ratio is assumed to be 50 (eg: Li, Seaquist, & Sage 1993; Mao et al. 2000). Appendix C contains more information about how the model was tested and used for this project.

Table 3.1: CO Line Ratios

Transitions	Line Ratios
$^{12}\text{CO} \frac{(3-2)}{(2-1)}$	$0.29 \pm 0.15$
$^{12}\text{CO} \frac{(2-1)}{(1-0)}$	$0.74 \pm 0.08$
$\frac{^{12}\text{CO} (2-1)}{^{13}\text{CO} (2-1)}$	$8.5 \pm 2.3$

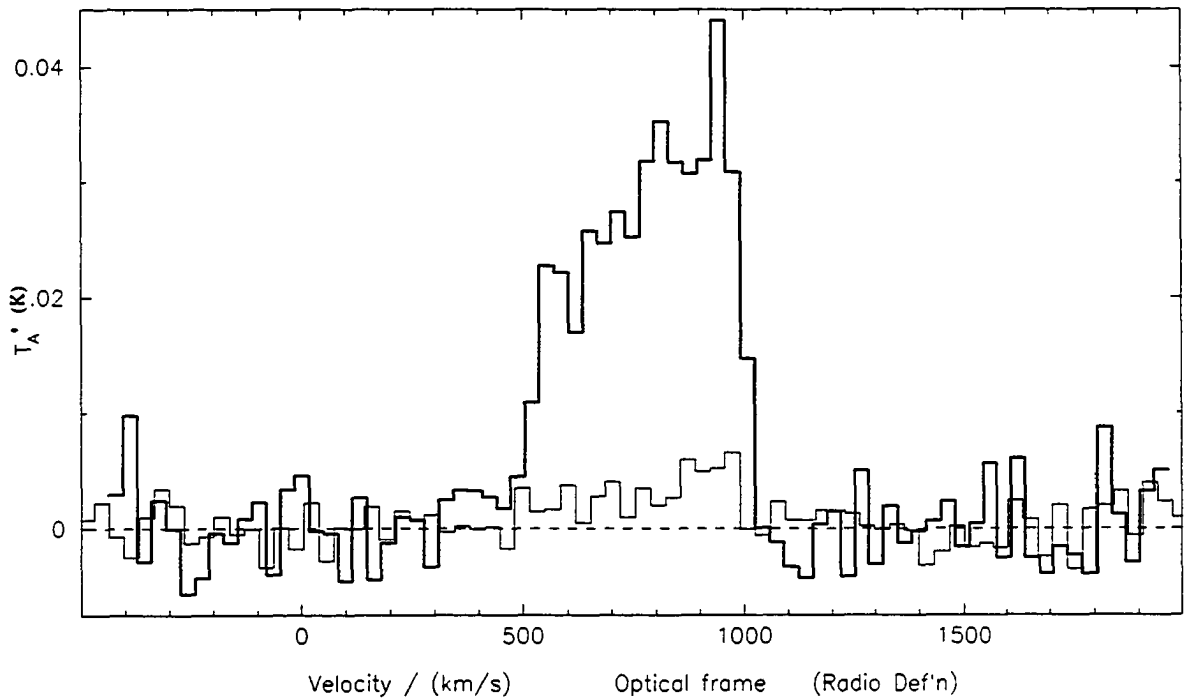


Figure 3.1:  $^{12}\text{CO}$  (dark line) and  $^{13}\text{CO} (2-1)$  (thin line) overlay in  $V(LSR)$  which displays the kinematic similarities of the gas at these two transitions.

## 3.2 Properties of the Molecular Gas

The CO lines, except for the  $J = 3 - 2$  transition, display similar line shapes (see Figure 3.1). The emission extends over  $V(LSR) = 500-1000 \text{ km s}^{-1}$ . The  $J = 3 - 2$  transition (see Figure 2.4) does show similar width, however, the line shape is opposite to that of the other transitions. The rest of the pointings (Figures 2.3–2.7) possibly show similar line widths but the line profiles are difficult to recover. Pointing errors could produce such results, however, it is possible that we are looking at different regions of gas. Despite those worries it will be assumed that the same gas is observed in all transitions.

Figure 3.2 represents the results of the LVG analysis on NGC 5866. The symbols  $R_{21}$ ,  $R_{32}$ , and  $R_{1213}$ , denote the ratios  $\frac{I_{CO(2-1)}}{I_{CO(1-0)}}$ ,  $\frac{I_{CO(3-2)}}{I_{CO(2-1)}}$  and  $\frac{I(^{12}CO)}{I(^{13}CO)}$ , respectively. The solid, dashed, and dotted lines represent loci of constant  $R_{21}$ ,  $R_{32}$ , and  $R_{1213}$ , respectively. Each set of three contours shows density–temperature pairs derived from the observed values in Table 3.1 and their one-sigma deviations. The acceptable ranges of physical conditions from the analysis, if all CO transitions are observed from the same region of gas, are a kinetic temperature of  $7 \text{ K} \leq T_{kin} \leq 13 \text{ K}$  and a molecular hydrogen density of  $n_H = (1.8 - 2.8) \times 10^3 \text{ cm}^{-3}$ . These ranges, shown by the red region in Figure 3.2, indicate that the gas is cool and moderately dense. If it is assumed that all the transitions are emitted from the same gas except the  $J = 3 - 2$  transitions then the modeled physical conditions would still have the same molecular hydrogen density with a temperature range of  $7 \text{ K} \leq T_{kin} \leq 20 \text{ K}$ . Those conditions are still consistent with cool and moderately dense gas.

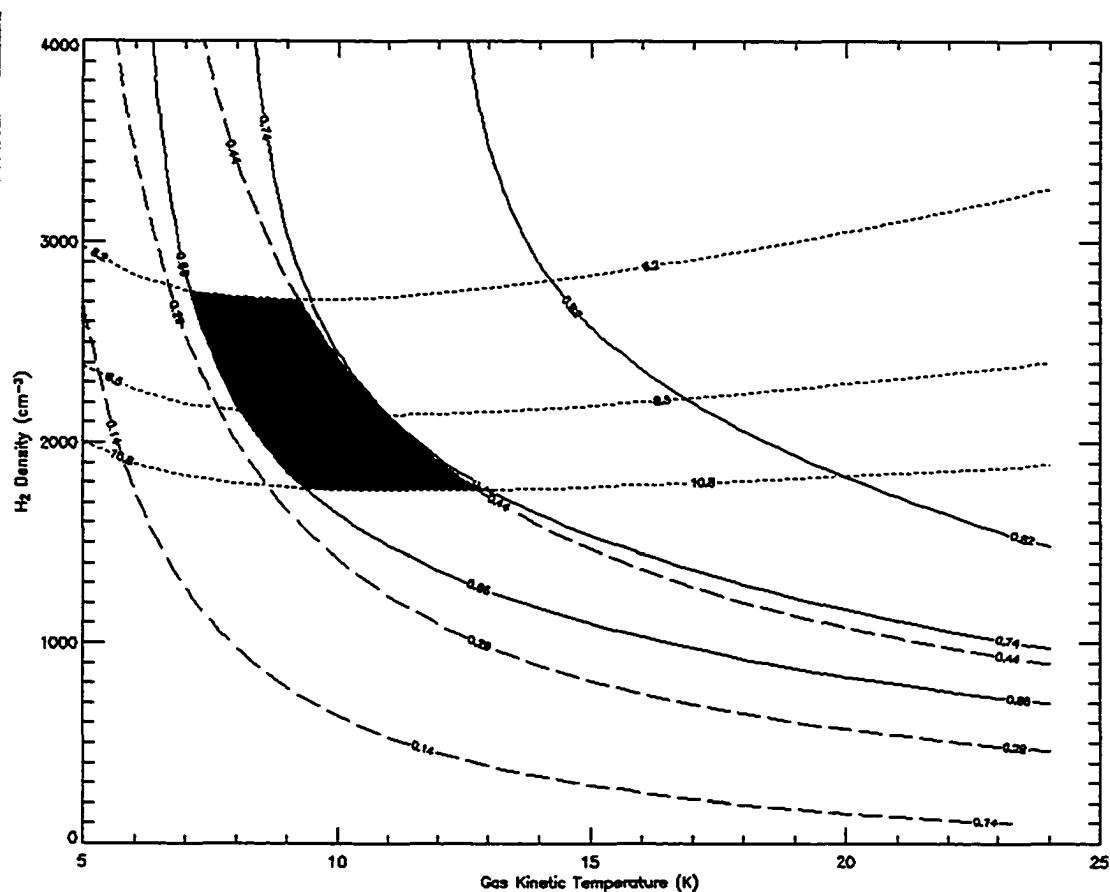


Figure 3.2: LVG model results. The solid, dashed, and dotted lines represent the  $R_{21}$ ,  $R_{32}$  and  $R_{1213}$ , respectively. The contours show the one-sigma deviations about the observed values. The red region indicates the allowed solution space if we assume that the emission from the different transitions is coming from the same gas.

The line ratios observed here are typical of those in other star forming S0s as well as spirals. The present results of  $R_{21} = 0.74 \pm 0.08$  falls within range of  $0.5 \leq R_{21} \leq 1.1$  determined for star-forming S0s (Sage 1990) spiral galaxies (Hafok & Stutzki 2003), and more specifically, for the arms of spirals (Garcia-Burillo, Guelin, & Cernicharo 1993). We also find that  $R_{32} = 0.29 \pm 0.15$  falls in the range covered by typical spirals (Hafok & Stutzki 2003). Similarly, a  $R_{1213} = 8.5 \pm 2.3$  falls in the range 5–10 which is typical of spiral arms (Garcia-Burillo, Guelin, & Cernicharo 1993). Note, however, that none of the above studies derives line ratios from observations having similar beam sizes. Line ratios used in those studies involve complicated correction factors that, except for  $R_{32}$ , are not necessary for this data set. Having similar beam sizes reduces the uncertainty in predictions for the environmental conditions of the molecular ISM.

One recent study of 10 early-type galaxies (Vila-Vilarró et al. 2003) has beam-matched observations of  $\frac{I_{CO(2-1)}}{I_{CO(1-0)}}$ ,  $\frac{I_{CO(3-2)}}{I_{CO(1-0)}}$ .  $^{12}\text{CO}(3-2)$  was detected in 6 galaxies. The line ratios in that study are consistent with that of NGC 5866. They conclude that there are possibly two distinct categories of galaxies: cool environments ( $T \leq 30$  K) and warm environments ( $T \geq 30$  K). In both categories, star formation is believed to be the sole heating process for molecular gas and dust (Vila-Vilarró et al. 2003). Both categories have ISM temperatures similar to those found in spirals. The similarity may be due to the fact that the star formation efficiency (SFE) is nearly the same as in spirals even though the SFR are several orders of magnitude smaller.

NGC 5866 appears to contain an environment typical of star-forming spirals even if we neglect the  $^{12}\text{CO}(3 - 2)$  transition. Hence, the physical conditions of the dense gas, together with the  $\text{H}\alpha$  and FIR emission indicates that NGC 5866 is forming stars and will probably continue to do so. The next chapter addresses the significance of star formation in heating the dust component of the ISM.

## Chapter 4

# Results: Origin of the FIR-sub-mm Radiation

This section will discuss the analysis of the SCUBA data. The goal is to determine the mass and the distribution of the interstellar dust in NGC 5866 and to infer the importance of dust heating sources such as newly forming stars. The analysis starts with a simple single temperature dust model used to get a general idea of the average temperature of the dust and a rough approximation of the dust mass. The approximated dust mass and other known properties of NGC 5866 are then used to construct a more sophisticated three-dimensional Monte Carlo model. Simulated SCUBA and optical images of NGC 5866 are compared to the data in an attempt to determine the morphology of the dust. In addition,  $H\alpha$  images are qualitatively compared to the SCUBA images to see if there are any resemblances or common features. The comparison could indicate the importance of dust heated by star formation in the SCUBA flux densities.

### 4.1 Single Temperature Models

Single-temperature dust models are used to constrain the mass and temperature of interstellar dust by modeling the IRAS and sub-mm fluxes (Fich & Hodge 1991).

Those models are a good representation of the FIR and sub-mm regimes but it is still a crude method since it is known that dust spans a wide range of temperatures and can not be represented by one value. This method does however provide an approximation of the average temperature and an order of magnitude approximation of the dust mass. The model is based on the assumption that dust radiates as a blackbody Planck function  $B(\nu, T)$  modified by a power-law emissivity of index  $\beta$ ,

$$S(\text{mJy}) \propto \left( \frac{\nu}{\nu_o} \right)^\beta B(\nu, T) \quad (4.1)$$

where  $\nu$  is the frequency and  $\nu_o$  is the dust emissivity characteristic frequency chosen to be at 250 microns. The temperature of the dust  $T$ , is determined through an iterative process using the equation above and is normalized by the flux densities from IRAS at 100 and 60 microns. The program is set to determine the temperature with an accuracy criterion of 0.1 K. Using the IRAS flux densities found for NGC 5866 (Knapp et al. 1989) in Table 4.1, dust temperatures were determined to be 30.0, 27.8, and 25.9 K for  $\beta = 1, 1.5$  and 2 respectively. By normalizing the above equation and using the temperatures determined for the emissivity indexes one can determine the predicted flux densities at 450 and 850 microns. Figure 4.1 shows the continuum emission from three different single temperature dust models with the indicated temperatures and emissivity indexes, which have been normalized to the 100 micron IRAS photometry. The IRAS 60 and 100  $\mu\text{m}$  and the SCUBA 450 and

850  $\mu\text{m}$  flux densities are shown with  $1\sigma$  uncertainties. As shown in Figure 4.1, the best least-squares fit results in a  $\beta$  of 1.38 and a dust temperature of 28.3 K. The value of 28.3 K is typical for dust temperatures as seen in a study of 23 early-type galaxies; Fich & Hodge 1993; Fich & Hodge 1991, using similar methods, find a range of temperatures from 20–40 K. Using the best-fit results, it is possible to determine the dust mass since

$$M_{dust} = \frac{S_{100\mu m}(\text{mJy}) \times D^2}{\left(\frac{100\mu m}{\nu_o}\right)^\beta B(\nu, T) \times 2.089 \times 10^{14}} \quad (M_\odot) \quad (4.2)$$

where  $D$  is the distance to the galaxy in Mpc. The dust mass was determined to be  $2.13 \times 10^6 M_\odot$ . Using  $M(H_2)$  from Welch & Sage (2003), this results in a  $M(H_2)$ -to- $M_{dust}$  ratio of 206 which is about a factor of two higher than the Galactic value.

It is worth noting that the IRAS and SCUBA data can also be fit to multi-component single temperature models to get an estimate of the contribution of various heating sources. A two component dust model was used to model the data to get an estimate of the cool dust mass in NGC 5866. First, the IRAS data was modeled with a hot dust component using a of  $\beta = 1.5$  giving a temperature of 27.8 K. The residual SCUBA flux densities (i.e. observed minus model) and the observed flux densities were then modeled using a cool dust component with a temperature of 11 K and using the same  $\beta$ . Dust masses were then calculated for both the hot and cold dust components. It was determined that the hot dust mass is

$M_{dust\ hot} = 2.09 \times 10^6 M_{\odot}$  and the cool dust mass is  $M_{dust\ cool} = 2.04 \times 10^6 M_{\odot}$ . The model indicates that there could be roughly and equal amounts of hot and cool dust residing in NGC 5866. The previous single temperature dust model does not show any evidence in for cool dust. The single temperature dust models are primitive and lead only to an order of magnitude estimate of the dust mass. The total dust mass predicted produce by the two-component model is  $M_{total} = 4.13 \times 10^6 M_{\odot}$ , which results in a  $M(H_2)$ -to- $M_{dust}$  ratio of 106 – roughly equal to the Galactic value.

The  $H_2$ -to-dust mass ratio is a controversial topic and is widely studied because the majority of galaxies seem to have a gas to dust ratio much higher than the Galactic value. Most of the studies are undertaken by using CO to predict the  $H_2$  mass and IRAS fluxes to get the dust mass. One foreseen problem is that IRAS is sensitive primarily to warm dust and that the warm dust mass is an underestimate of the total dust mass for all types of galaxies (Young, et al. 1989) implying that most of the dust would be cooler than 30 K. There is some evidence for more cool dust than warm dust from a survey of 14 early-type galaxies by Fich and Hodge (1993). They observed a sample of galaxies in the sub-millimeter and added data from IRAS in order to see both the warm and cool dust. According to their models, which are similar to the single temperature dust models, they find evidence that the amount of cool dust is an order of magnitude greater than that of the warm dust. In their sample they also find galaxies that have gas-to-dust ratios close to the Galactic value of 100.

It is difficult to determine from the single temperature dust models whether NGC 5866 contains large amounts of cool dust. The sub-millimeter fluxes fit extremely well to a single temperature dust model as well as a multi-single temperature dust model. The first model shows no direct evidence of large amounts of cool dust unless that dust is extremely cold and the second model shows that there are roughly equal amounts of hot and cool dust. Further studies of cool dust can be achieved using Monte Carlo models.

Gas-to-dust ratios have been measured in large samples such as the survey by Young et al. (1989). They found, out of 128 galaxies of all types, an  $H_2$ -to-dust mass ratio of  $570 \pm 50$  which is almost a factor of 6 times that of the Galactic value. They also found a tight correlation, correlation coefficient of 0.97, for 170 galaxies

$$M(H_2) = 4.0 \times 10^2 M_D^{1.04 \pm 0.02} \quad (4.3)$$

where the masses are in solar units. This would give NGC 5866 a predicted ratio of  $716 \pm 195$  which is higher than the derived from Equation 4.2 however, it is within  $3\sigma$ . Their equation is not specific to early-type galaxies, however, and therefore a good agreement is not expected.

Another IRAS-based survey by Wiklind, Combes and Henkel (1995) demonstrated that the average gas-to-dust ratio was roughly 700 for a survey of 29 ellipticals. They also found that there was a small fraction of galaxies that had gas-to-

---

dust ratios as low as 50. It appears that possession of low gas-to-dust ratios is not correlated with FIR luminosity or blue luminosity. They found, however, that the gas-to-dust ratio depended on the dust temperature, i.e. that galaxies with a low gas-to-dust ratio have low dust temperatures. It is possible then that these galaxies with low gas-to-dust ratios and low dust temperatures contain copious amounts of cool dust to which the IRAS survey was not sensitive.

In the next section we will take full advantage of the SCUBA data, and not only model the photometric flux but also generate images to find further information about the specific distributions in the galaxy. The cool (diffuse) dust component of NGC 5866 will be modeled using a Monte Carlo radiative transfer code by Bjorkman and Wood (2001). The next section describes the code and the parameters required specifically to model NGC 5866.

Table 4.1: FIR and SCUBA Flux Densities

Wavelength ( $\mu\text{m}$ )	Flux Density (Jy)
60	$5.21 \pm 0.021$
100	$16.61 \pm 0.051$
450	$1.75 \pm 0.7$
850	$0.28 \pm 0.03$

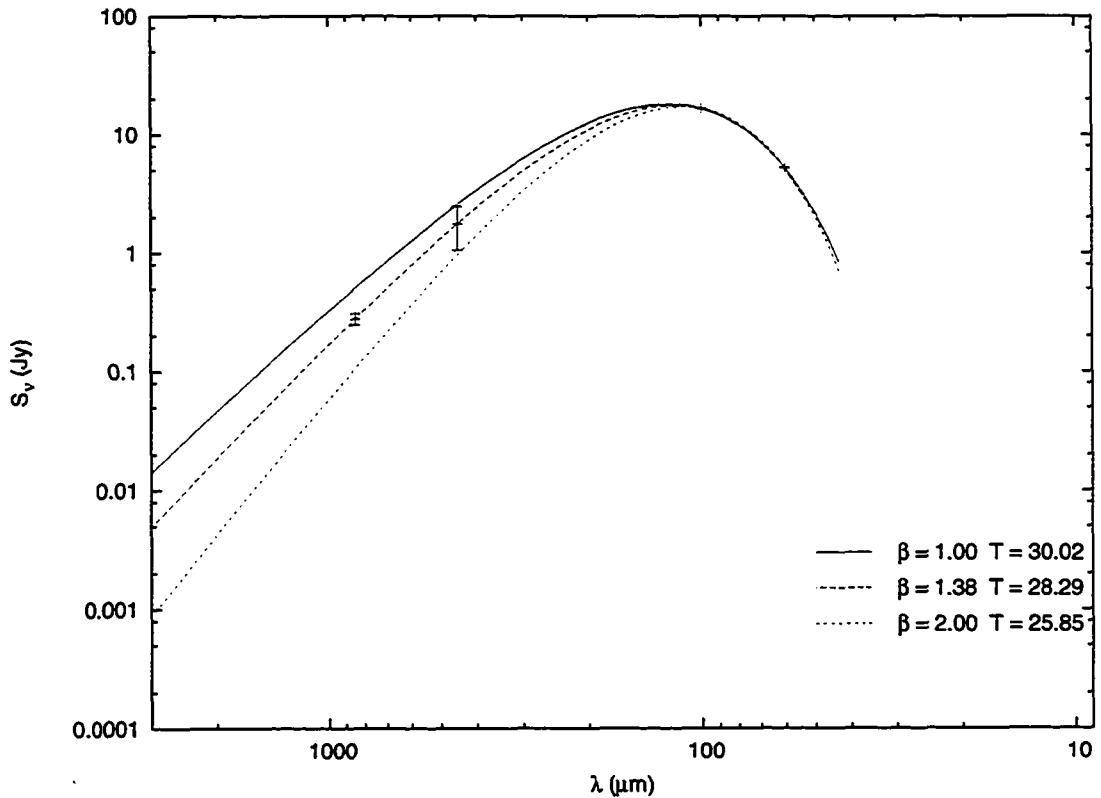


Figure 4.1: The IRAS 60 and 100 micron and the SCUBA 450 and 850 micron flux densities are drawn with one sigma uncertainties. The curves show the continuum emission from single temperature dust models with the indicated temperatures in Kelvin and emissivity indexes.

## 4.2 Monte Carlo Model

In order to take full advantage of the SCUBA dust maps and going beyond modelling photometry which limits one to single temperature dust models, we will now utilize a three-dimensional radiative transfer model. Radiative transfer models are not restricted to a global single dust temperature but allows dust to heat and cool governed by its local environment and dust properties, respectively. It is also possible to explore the spatial distribution of dust and produce simulated images that can be compared directly to SCUBA maps to see what dust morphologies are allowed within the observations. The possibility of constraining dust morphology and the importance of possible heating sources is one major advantage to these types of models. Simulated spectra can also be used to constrain additional model parameters.

The Monte Carlo radiative transfer simulations (Bjorkman & Wood 2001) used here are based on following photons as they are scattered, absorbed and re-emitted within the ISM. The advantage of this method is that the positions of the photons are always known so that the distribution of energy within the ISM is also known. The spectral energy distribution (SED) of the heating source is broken up into monochromatic photon packets which are stochastically emitted. The dust is heated by the incoming photons where the frequencies of the interactions are determined from the optical depth. Since the system is in radiative equilibrium, the absorbing grain will re-radiate photons at other wavelengths. The process of scattering, absorption and re-emission, will continue until all the photons have escaped from the galaxy.

The outgoing photons are placed into frequency and observed-direction bins. The method thus provides a way of determining the SED and producing images at a given wavelength. The code does not account for rapidly heated dust grains which becomes important in the near-IR between 5 and 30 microns; however, this does not affect the regimes that we are attempting to model. The code does not account for star formation as a heat source. The only heating source is the general stellar population determined by the input SED. We will now discuss the parameters that were used to make this model appropriate for NGC 5866.

### 4.2.1 Geometries & Parameters

A summary of the geometries, as well as the parameters used in the code appears in Table 4.2. The model consists of two main components; stellar and ISM. Each component will be distributed in the bulge and the disk of the model galaxy.

A single Jaffe (1983) model was used to represent the distribution of light and dust in the bulge component. It was assumed that the dust in the bulge of the galaxy models have the same distribution as the stellar component in order to minimize the number of free parameters. The Jaffe model for the stellar luminosity distribution  $L_\nu(r)$ , and the dust distribution  $\rho_b(r)$  are

$$L_\nu(r) \ \& \ \rho_b(r) \propto \frac{1}{\frac{r^2}{r_j^2} \left(1 + \frac{r^2}{r_j^2}\right)^2} \quad (4.4)$$

where the bulge size is a function of the Jaffe radius, which is defined as  $r_J = r_e/0.763$  where  $r_e$  is the effective radius which is defined as the distance from the center of a galaxy from within which half the galaxy's luminosity is emitted. The effective radius is  $37''$  (Fisher, Franx, & Illingworth 1996) for NGC 5866, which is 2.74 kpc for a distance of 15.3 Mpc.

The stellar luminosity  $L_\nu(r, z)$  and dust  $\rho_b(r, z)$  distributions in the disk are represented by a double exponential in cylindrical coordinates

$$L_\nu(r, z) \ \& \ \rho_d(r, z) \propto \exp\left(\frac{-z}{h_z} + \frac{-r}{h_r}\right) \quad (4.5)$$

where  $h_z$  is the exponential scale height and  $h_r$  is the exponential scale length. The stellar exponential scale length  $h_{r,*}$  is  $28''$  (Fisher, Franx, & Illingworth 1996) or 2.08 kpc at a distance of 15.3 Mpc. The stellar exponential scale height of NGC 5866 has not been measured; therefore, we will use a study by de Grijs and Kruit (1996) who sampled eight early-type spirals in the B, V, R, and I bands and found that the ratio of the scale length to scale height is well behaved with a mean value of 5.9. Using their results gives NGC 5866 a scale height  $h_{z,*}$  of 0.687 kpc. The dust distribution in the disk is similar to that of the stellar component except that the scale height  $h_{z,dust}$  and scale length  $h_{r,dust}$  for the dust will remain free parameters in order to test an array of dust scale heights and lengths.

The galaxy luminosity distribution, in both the disk and the bulge, is scaled by

the parameter  $L_{\nu_o}$ .  $L_{\nu_o}$  is used to normalize the output SED to that of the observed values in U, B, V, J, H, K which were obtained from the NASA Extragalactic Database (NED) (see Table 4.3). The output SED is normalized by adjusting the scaling parameter until a  $\chi$ -squared minimization fit is achieved between the output SED and the the observed data from Table 4.3. The other scaling function  $L_b$  is used to account for the amount of light contributed by only the bulge component of the galaxy. That is determined from the optical bulge-to-disk luminosity ratio  $L_{bd}$  which is 0.44 for NGC 5866 (Khosroshahi, Wadadekar, & Kembhavi 2000).

The bulge stellar luminosity contribution  $L_b$  is scaled over the entire volume of the bulge where it is evaluated from the minimum resolution of the bulge of  $r_{min} = 1.01$  pc to a bulge cutoff limit of  $r_{max} = 7000$  pc. The minimum radius is a limit set by the code and it is not necessary, for the purpose for this study, to know what is going on in the central parsec of the galaxy. The upper limit,  $r_{max}$ , is the maximum size of the galaxy. The luminosity in the disk  $L_d$  is normalized in a similar manner except over a cylinder of height  $h_z$  and radius  $h_r$ .

The total mass of gas and dust in the model is defined as  $M_{ISM}$  and will be initially set to the molecular gas mass found by Welch & Sage (2003). The fraction of dust and gas in the bulge is  $M_{bulge}$  and is a free parameter.  $M_{bulge}$  is the bulge mass fraction where  $0 \leq M_{bulge} \leq 1$ , such that  $M_{bulge} = 0$  implies no dust in the bulge (i.e. all the dust is in the disk). The dust density distributions are normalized in the bulge  $\rho_{b_o}$  and the disk  $\rho_{d_o}$  in the same fashion as the stellar luminosity (see Table 4.2).

The dust opacity model used here are from Kim, Martin, and Hendry (1994). Their opacity models are based on a mixture of spherical bare silicates and bare graphites that have a size and abundance distribution of that of the Milky Way. The code does not assume that photons undergo isotropic scattering with the dust, instead they obey a Henyey–Greenstein phase function which is typically used in dust models. The opacity model has been successfully used in various modified versions of this code (see Whitney, Wood, Bjorkman, & Wolff 2003; Matthews & Wood 2001).

The opacity models are calculated for a gas and dust mixture and thus have a built in assumption that the gas-to-dust ratio is equal to that of the Galactic value of 100. At the wavelengths of interest, the gas carries almost all the mass and the dust carries almost all the opacity. In order to change the gas-to-dust ratio one can either generate new opacities tables or the same result can be achieved by changing  $M_{ISM}$ . That can be done since the radiation transfer code computes the product of ISM mass and opacity. So the gas-to-dust ratio can be modified by multiplying either  $M_{ISM}$  or the opacity tables.

The input stellar spectral energy distribution for the model of NGC 5866 was chosen from Bruzual and Charlot (1993). The simulated SED chosen was a 1 Gyr star formation burst model at an age of 10 Gyr. The output SED will be normalized to the optical data from Table 4.3. In order to artificially observe the galaxy, transmission functions are required to appropriately account for the passbands used at the telescopes. The optical filters are obtained for passbands for the Johnson–

---

Cousins UBVRI system which have been devised by comparing synthetic data with actual observations (Bessel 1990). The IRAS and SCUBA functions were obtained directly from the respective websites. The maximum transmission of all filters were normalized to 1.

It has been assumed that the galaxy is viewed edge-on so that the inclination of the disk is 90 degrees.

To summarize, the distribution of stars and dust in the bulge are represented by a single Jaffe model, while the stars and dust in the disk are represented by separate double exponential functions. All the parameters are fixed by observation except for three free parameters: bulge mass fraction  $M_{bulge}$ , dust scale height  $h_{z_{dust}}$ , and the dust scale length  $h_{r_{dust}}$ . The scaling factor  $L_{\nu_o}$  can be constrained by the optical data for NGC 5866 and the other three parameters will be constrained by the images taken by SCUBA. We will now proceed to model the galaxy and see if it is possible to constrain the three free dust parameters.

Table 4.2: Input Geometries for Model for NGC 5866

Description	Parameters
Stellar distribution in the bulge	$L_\nu(r) = \left(\frac{L_b}{4\pi}\right) L_{\nu_o} \frac{1}{\frac{r^2}{r_J^2} \left(1 + \frac{r^2}{r_J^2}\right)^2}$
Stellar distribution in the disk	$L_\nu(r, z) = L_d L_{\nu_o} \exp\left(\frac{-z}{h_{z_*}} + \frac{-r}{h_{r_*}}\right)$
Bulge luminosity contribution	$L_b = \frac{L_{bd}}{r_J^3} \frac{1}{\frac{1}{1 + \frac{r_{min}}{r_J}} - \frac{1}{1 + \frac{r_{max}}{r_J}}}$
Disk luminosity contribution	$L_d = \frac{1 - L_{bd}}{4 \pi h_{z_*} h_{r_*}^2}$
Maximum & minimum limits for bulge	$r_{min} = 1.01^a$ pc $r_{max} = 7000$ pc
Bulge-to-disk ratio	$L_{bd} = 0.44$
Jaffe radius for stars & dust	$r_J = 3590$ pc
Stellar disk scale height	$h_{z_*} = 687$ pc
Stellar disk scale length	$h_{r_*} = 2080$ pc
Dust distribution in the bulge	$\rho_b(r) = \rho_{b_o} \frac{1}{\frac{r^2}{r_J^2} \left(1 + \frac{r^2}{r_J^2}\right)^2}$
Dust distribution in the disk	$\rho_d(r, z) = \rho_{d_o} \exp\left(\frac{-z}{h_{z_{dust}}} + \frac{-r}{h_{r_{dust}}}\right)$
Initial bulge dust density	$\rho_{b_o} = \frac{M_{ISM} M_{bulge}}{r_J^3} \frac{1}{\frac{1}{1 + \frac{r_{min}}{r_J}} - \frac{1}{1 + \frac{r_{max}}{r_J}}}$
Initial disk dust density	$\rho_{d_o} = \frac{M_{ISM} (1 - M_{bulge})}{4 \pi h_{z_{dust}} h_{r_{dust}}^2}$
Scaling Factor	$L_{\nu_o}$
Free parameter: dust scale height	$h_{z_{dust}}$
Free parameter: dust scale length	$h_{r_{dust}}$
Free parameter: bulge mass fraction	$M_{bulge}$

<sup>a</sup>limit set by MC code

Table 4.3: Optical and NIR Flux Densities

Filter	Wavelength ( $\mu\text{m}$ )	Flux Density (Jy)
U	0.365	$0.0645 \pm 0.0045$
B	0.439	$0.216 \pm 0.014$
V	0.522	$0.403 \pm 0.027$
J	1.24	$1.48 \pm 0.38$
H	1.63	$2.14 \pm 0.55$
K	2.18	$1.78 \pm 0.46$

## 4.3 Initial Monte Carlo Radiative Transfer

### Models

With the model geometries set, an initial model was run to see how well the model fit the observed data. It seems natural to assume for a first run that the stellar scale length and height are equal to that of the dust (i.e.  $h_{z_{dust}} = h_{z_*}$  &  $h_{r_{dust}} = h_{r_*}$ ). The next likely assumption is that dust obeys the same luminosity ratio as the bulge-to-disk ( $M_{bulge}=0.44$ ).

The model outputs can be seen in Figures 4.2 and 4.3. The model predicted fluxes seen in the SED fit within the observed uncertainties of the optical data but do not fit within the uncertainties of the IRAS and SCUBA fluxes. It appears, from the SED, that there might be a set of dust scale lengths and heights that would better fit the observed data. The model images in Figure 4.3 make it clear that the set of parameters do not reproduce the SCUBA images. The model images are convolved with the appropriate SCUBA resolutions in order to compare them directly. The images are very bulge dominated and not very disk-like at 450 microns. The bulgy model images could arise from having too much dust in the bulge and/or having too small dust scale lengths and heights in the disk.

In order to resolve this problem, the next section will have an array of models with a wide range of values for the three unknown parameters. It is our hope to constrain the geometry of the dust in NGC 5866.

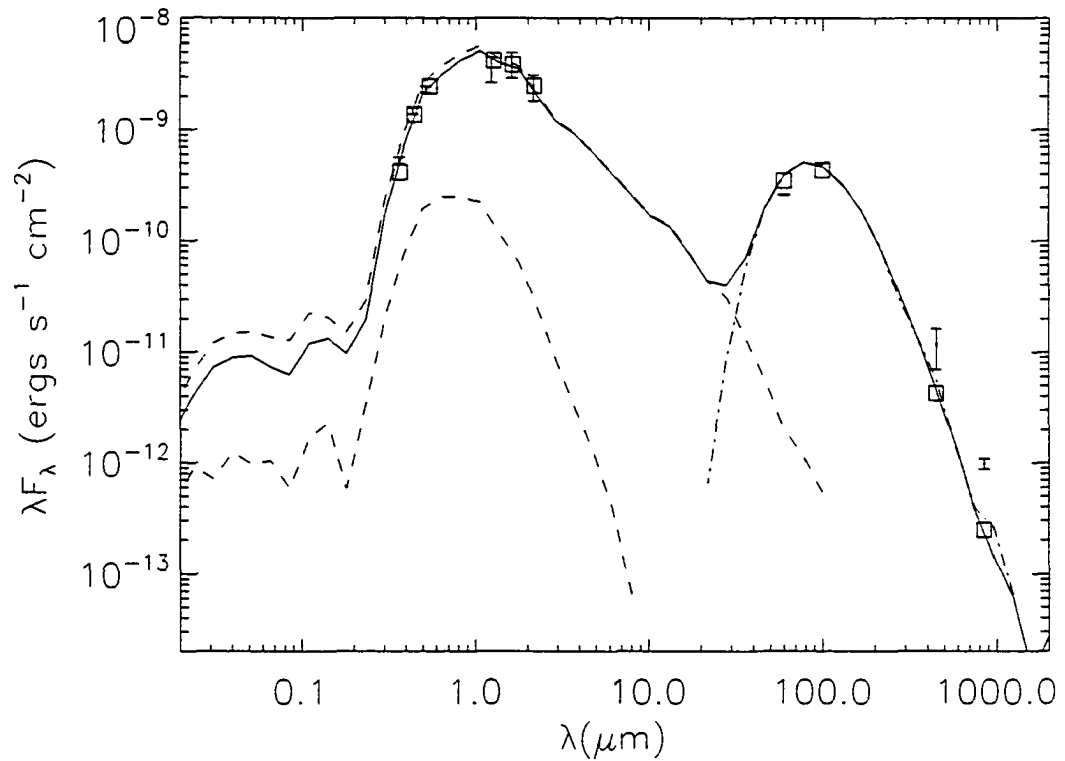


Figure 4.2: Sample SED (solid line) for NGC 5866 predicted by the Monte Carlo code. The boxes are the predicted fluxes and the 10 data points are the observed fluxes for NGC 5866 at, respectively, U, V, B, J, H, K, IRAS 60  $\mu\text{m}$ , IRAS 100  $\mu\text{m}$ , SCUBA 450  $\mu\text{m}$ , SCUBA 850  $\mu\text{m}$ . The top dashed line represents a typical SED of a one Gyr burst model of age of 10 Gyr. The lower dashed line shows the SED of scattered emission and the dashed dotted line represents the re-radiated, thermal contribution.

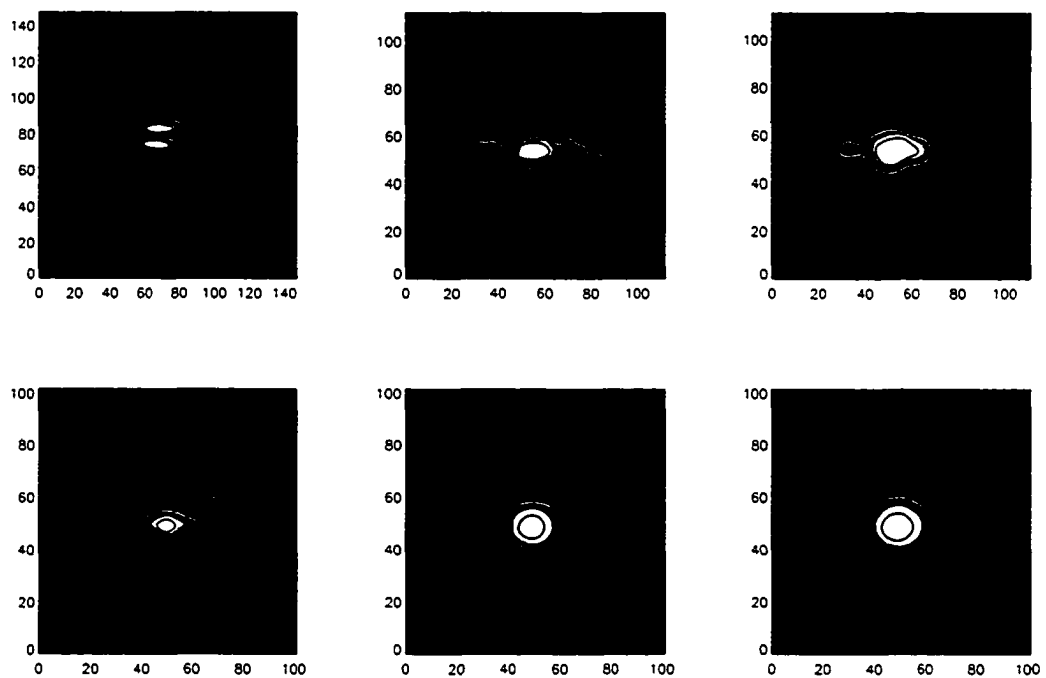


Figure 4.3: The top row: images of NGC 5866 in the V-band and 450 and 850  $\mu\text{m}$  respectively. Below are images produced by the model for comparison. The contours are one-fifth of the max value. The model sub-mm images have been convolved with the appropriate SCUBA beam sizes. All images are  $101'' \times 101''$ .

## 4.4 Further MC Radiative Transfer Models

A large parameter space will now be explored to see how well the models fit the observed data. A broad parameter space is first explored with  $h_{z_{dust}}$ ,  $h_{r_{dust}}$  and  $M_{bulge}$  in hope to constrain one or more parameters.

For each set of  $h_{z_{dust}}$  and  $h_{r_{dust}}$ , the bulge mass will vary such that  $M_{bulge} = 0, 0.10, 0.25, 0.5, 0.75$ . The dust scale height will vary from  $h_{z_{dust}}(\text{pc}) = 50, 100, 200, 300$  and the dust scale length will vary from  $h_{r_{dust}}(\text{pc}) = 580, 1080, 1580, 2080$ . In order to restrict the parameter space, it is assumed that the dust scale heights and lengths are not greater than that found for the stellar component. The dust scale height will be limited to 300 pc because of the size of the dark dust lane observed in the optical images. The above parameter space results in a total of 80 models. Before the models are started, an additional step must be taken in order to normalize the stellar SED from Bruzual and Charlot (1993) to the data found in Table 4.3. Adjusting the parameter  $L_{\nu}$  causes the stellar emission component of the SED to increase or decrease in total flux. This parameter can be adjusted until a best fit is obtained with the observations. The details of the normalization are provided in Appendix E. We chose to normalize the output SED for one particular set of parameters ( $h_{z_{dust}} = 100$  pc,  $h_{r_{dust}} = 2080$  pc,  $M_{bulge} = 0$ ) knowing that the normalization would not be the same for all 80 models. That is not a problem since the dust emission component of the output SED scales linearly with  $M_{ISM}$ . Therefore, by fine tuning each model by adjusting  $M_{ISM}$  to the desired best fit to the IRAS and SCUBA data. For this study, the dust component of the output SED

will be normalized such that the 60 and 100  $\mu\text{m}$  fluxes are equally over and under predicted, respectively. Implying that the difference in the uncertainties in the 60 and 100  $\mu\text{m}$  is equal to zero. Now that all the models are set to the same level, they can be directly compared.

#### 4.4.1 Parameter Search

The images and the output SED of all 80 models were analyzed. Appendix F contains the images of 64 of the 80 models where the models for  $M_{bulge} = 0.75$  were left out since they were highly bulge dominated and did not display anything useful.

Looking at the FIR predicted flux densities from all 80 models we find a trend displayed in Figure 4.4. The model flux density errors describes the percentage by which the 60 and 100  $\mu\text{m}$  fluxes are over and under predicted, respectively. In other words, it is the percent accuracy of predicting the observed fluxes so that for example, in Figure 4.4 30% implies that the model predicted flux is 30% greater than observed at 60 microns. An acceptable fit occurs when the model fluxes are predicted to within the uncertainties of the observations so when the model fluxes are within 0.4% and 11% at 60 and 850 microns, respectively. The points are such that for each scale length and bulge mass there are four scale heights binned into one point and the errors are derived by the variance produced by the four scale heights. Models having 10% or more of the dust mass in the bulge do not fit the FIR data well and can only get within 16% of the observed errors. However, for models with no dust in the bulge the data fit is much better and improves with

larger disk scale heights. The best fit occurs when  $h_{\tau_{dust}} = h_{\tau_*}$  and  $M_{bulge} = 0$  and can predict the FIR flux densities within 7%, which is still much larger than the observed uncertainties (0.4% at 60 microns and 0.3% at 100 microns). This would suggest that if all the dust is heated by the general stellar population without star formation then there should be virtually no dust in the bulge of the galaxy.

The SCUBA data displays similar trends to that found in the FIR data except the SCUBA data were not as well predicted as the FIR regime where acceptable values should be around 40% and 11% at 450 and 850 microns, respectively. Figure 4.5 and Figure 4.6 show again that as the mass of dust in the bulge decreases and the disk scale length increases, the predicted flux densities improve. In all of the models the SCUBA data are under-predicted. This result is not so surprising since the code being used simulates only dust being heated by the general stellar population and not by active star formation. There is some evidence, which has been previously discussed, that indicates that there is a comparable amount of active star formation occurring in NGC 5866. In the next chapter we will attempt to correct for dust being heated by star formation in hope of producing a better SED fit.

Figure 4.7 is the resulting output SED for one of the best fit models. Only the model predicted optical fluxes fit within the measured uncertainties. The model fit is not satisfactory since the sub-mm modeled data are less than that of the observed fluxes and heating by the general stellar population cannot account for it within the explored parameter space. Presumably, the sub-mm wing will increase only if more dust is placed at larger radii.

Figure 4.8 is one set of model images produced by the code. The top row of images (left to right) are the V-band and SCUBA 450 and 850  $\mu\text{m}$ , respectively, with the corresponding simulated images underneath. The parameters that define geometries of the simulated images are  $h_{z_{dust}} = 100$  pc and  $h_{r_{dust}} = 2080$  pc with varying  $M_{bulge} = 0, M_{bulge} = 0.10, M_{bulge} = 0.25, M_{bulge} = 0.50$  for rows 2, 3, 4, 5 respectively. The images are displayed such that the box sizes are  $101'' \times 101''$  for all images so that the sizes of features can be compared directly. All the other model images can be found in Appendix F for comparison. The second row in Figure 4.8 are the images that correspond to the SED in Figure 4.7. The model images are smoothed to the SCUBA 450 and 850 micron resolution, respectively. The images produced by the code solidify the findings produced by the output SEDs. In all Figures F.6–F.21 it is evident that as the bulge mass fraction increases the images become less like the observations. Also, short disk dust scale lengths create a bulge-like feature which tends to be boxy. As the scale length increases, for any assumed scale height, the images become more similar to what is observed. Thus both images and SEDs indicate a low bulge mass fraction and a large disk scale length for the dust.

Even with  $M_{bulge} = 0$  the contours of the simulated sub-mm images are still too compact and do not look like the data. It would appear that, and as Figure 4.4 would suggest, the scale length of the dust would have to be greater than the stellar scale length in order to produce more cold dust emission and to produce more realistic images. One may therefore ask whether the fit improves if  $h_{r_{dust}} > h_{r_*}$ . Could

more cool dust be hidden further out within the stellar distribution? The best fit SED as seen in Figure 4.7, requires  $M_{ISM} = 6.30 \times 10^8 M_{\odot}$  which is larger than the observed ISM mass of NGC 5866. Given the code assumes a  $M(H_2)$ -to- $M_{dust}$  ratio of 100 this would give a dust mass of  $6.30 \times 10^6 M_{\odot}$  which is a factor of 1.5–3 more than predicted by the single temperature dust models. This demonstrates that there is possibly more cool dust than predicted or the gas-to-dust ratio is quite larger. A larger gas-to-dust ratio is also consistent with other galaxy surveys. It is also difficult to constrain the scale height of the dust by using the SEDs and the images. It does seem here that the scale height does not exceed that of the stellar component. It is also worth noting that the V-band image can be reproduced by most models implying that the key to constraining the free parameters rely on the imaging capabilities of SCUBA.

The parameter search will now be expanded to see how changing the scale height changes the results of the models and also determine how far does the dust need to extend within the disk in order to correctly predict the sub-mm fluxes and produce more realistic sub-mm images.

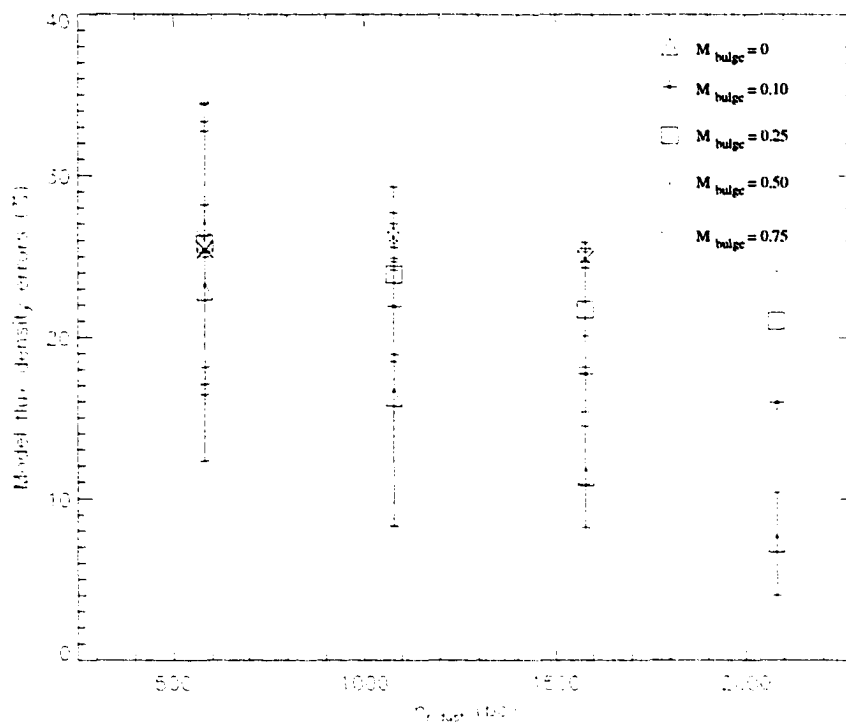


Figure 4.4: The model flux density error is the percentage by which the observed FIR flux is under or over predicted at 60 and 100 microns for a given scale length. Each point represents the average of four scale heights, as explained in the text.

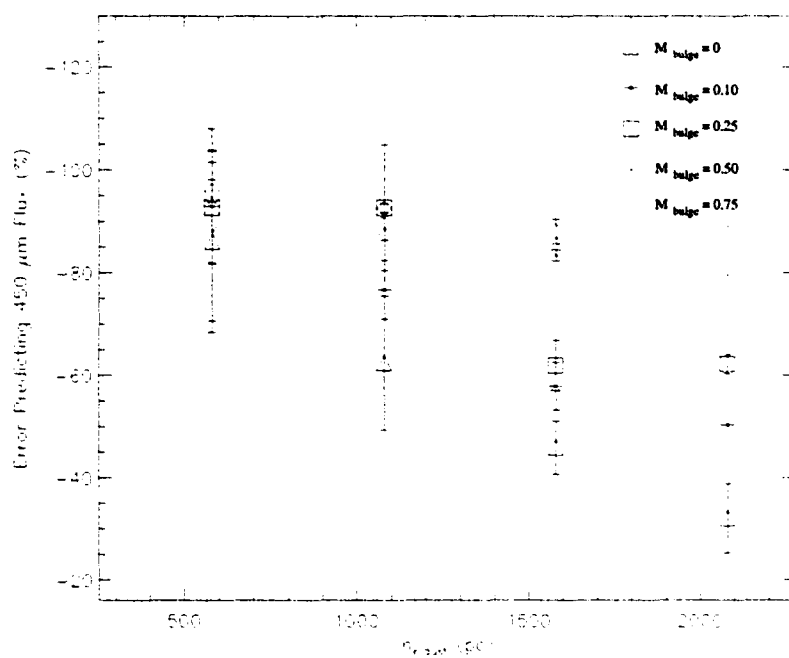


Figure 4.5: The percentage errors in predicting the SCUBA 450  $\mu\text{m}$  flux density. The values are negative since the models always under predicted the values. The binning and error bars are the same as in Figure 4.4.

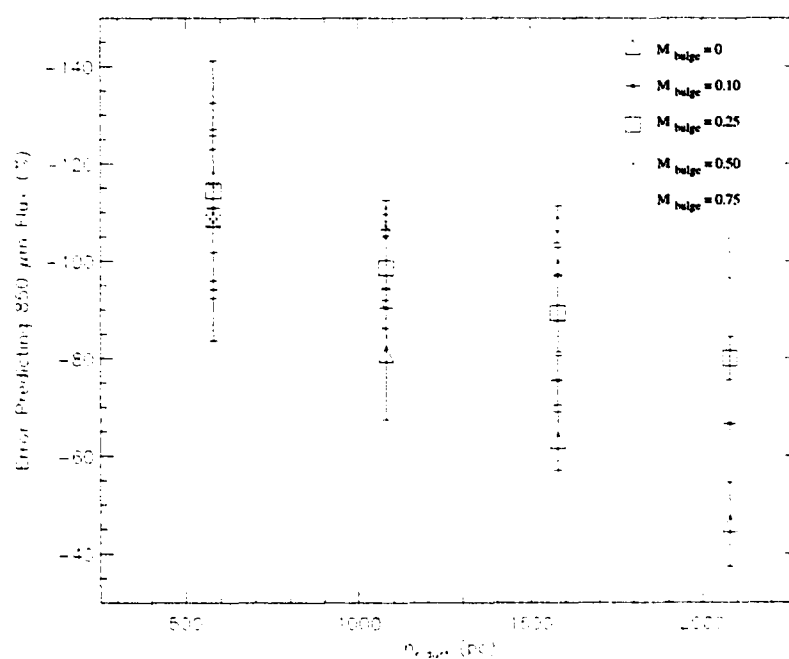


Figure 4.6: Same as Figure 4.5 except for 850  $\mu\text{m}$ .

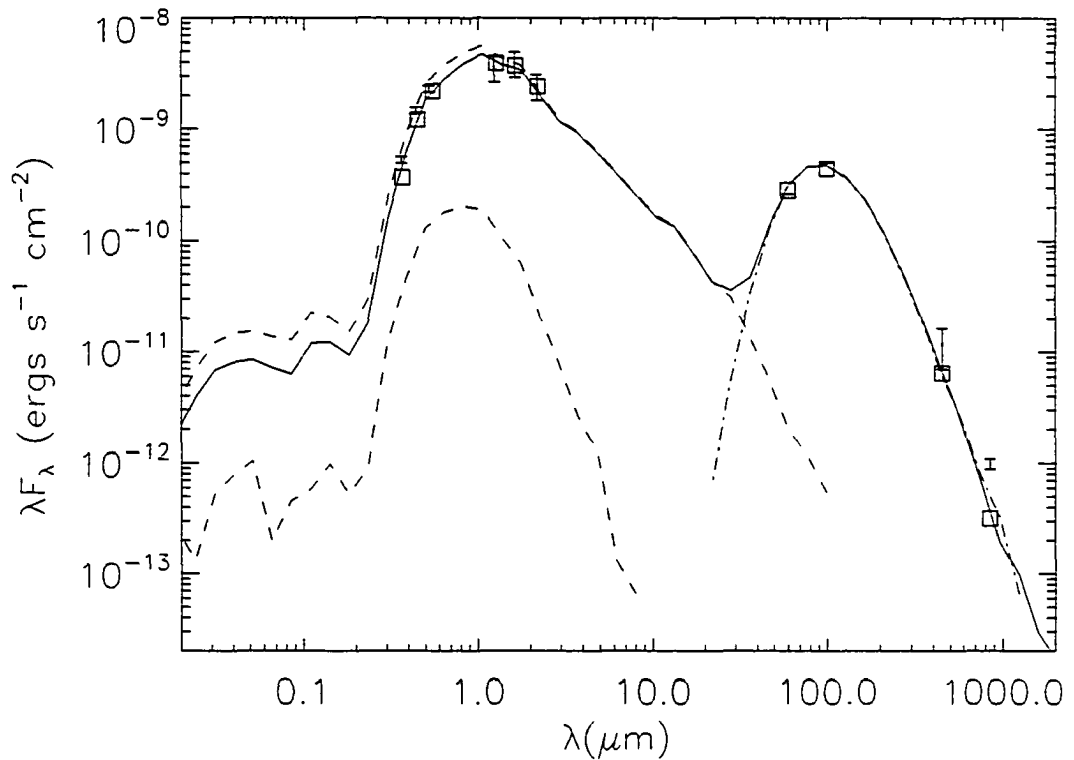


Figure 4.7: Sample SED (solid line) for NGC 5866 predicted by the Monte Carlo code for parameters  $h_{z_{dust}} = 100$  pc,  $h_{r_{dust}} = 2080$  pc &  $M_{bulge} = 0$ . The boxes are the predicted fluxes and the 10 data points are the observed fluxes for NGC 5866 at, respectively, U, V, B, J, H, K, IRAS 60  $\mu\text{m}$ , IRAS 100  $\mu\text{m}$ , SCUBA 450  $\mu\text{m}$ , SCUBA 850  $\mu\text{m}$ . The top dashed line represents a typical SED of a one Gyr burst model of age of 10 Gyr. The lower dashed line shows the SED of scattered emission and the dashed dotted line represents the re-radiated, thermal contribution.

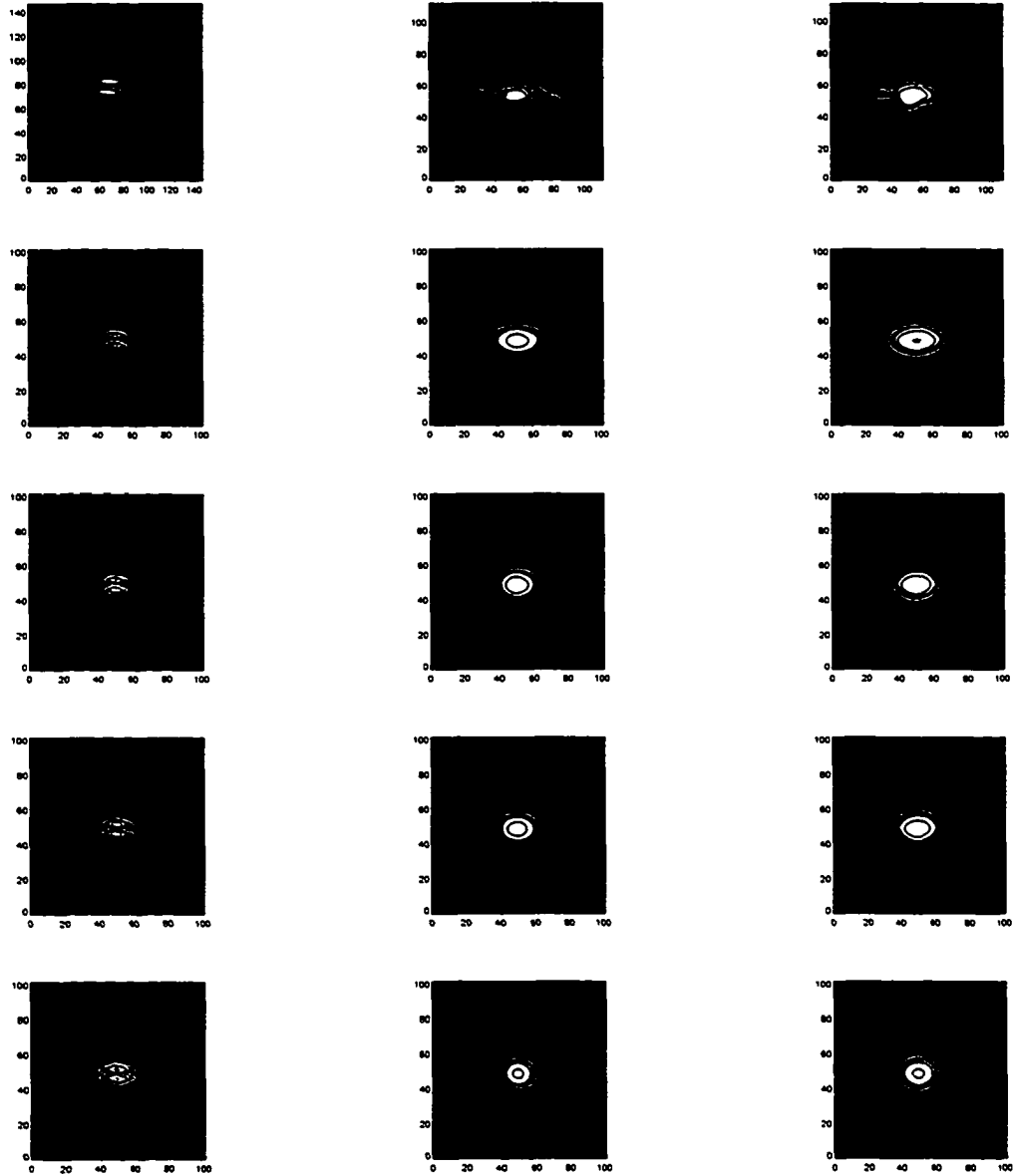


Figure 4.8: The top row: images of NGC 5866 in the V-band and 450 and 850  $\mu\text{m}$  respectively. Below are images produced by the models for comparison. The parameters for the remaining four rows are:  $h_{z_{dust}} = 100$  pc,  $h_{r_{dust}} = 2080$  pc &  $M_{bulge} = 0, 0.10, 0.25, 0.5$  for rows 2, 3, 4, 5 respectively. The contours are one-fifth of the max value. All images are  $101'' \times 101''$ .

#### 4.4.2 Monte Carlo Models: Refined

We first test how the dust scale height alone changes the predicted fluxes. The scale length remains fixed at  $h_{r_{dust}} = 2080$  pc and also fix the bulge mass fraction such that  $M_{bulge} = 0$  and vary the dust scale height are  $h_{z_{dust}}(\text{pc}) = 50, 100, 200, 300, 400, 500, 687$ . Figure 4.9 shows the predicted FIR and sub-mm flux densities as a function of dust scale height. Constraints on the scale height are not apparent here because there is no visible trend within the SED data. The images produced by the models may constrain the data more effectively. Figure 4.10 show that for scale heights larger than 300 pc, the V-band image starts to lose its dust lane. However, the SCUBA images appear unchanged. The optical images, therefore, suggest that dust scale height must be less than or equal to roughly 300 pc.

In order to limit the parameter space, the assumption was made that the dust distribution is not greater than the stellar component. There have been hints from the SED fits, however, that there could be a preference for the dust having a larger disk scale length than the stellar distribution. On the other hand, the assumption has been verified observationally by several groups. One such study looked at 25 partially overlapping spiral galaxies and directly measured the effective absorption in galaxy disks (White, Keel, & Conzelmann 2000; Domingue et al. 1999). This technique is independent of internal disk structure of the galaxy. The inter-arm dust was found to have a scale length consistent with that of the disk stellar component. Other radiative transfer models such as Matthews and Wood (2001) have assumed dust scale heights smaller than that of the stars and others have chosen dust scale

heights equal to that of the stars (Byun, Freeman & Kylafis 1994). Therefore the assumption appears to be reasonable. We ran four additional models with fixed  $h_{z_{dust}} = 200$  pc and  $M_{bulge} = 0$ , where the dust scale length is set to  $h_{r_{dust}} = 1.5, 2.00, 2.50, 3.00$  times the stellar scale length. Figure 4.11 shows the predicted flux densities for varying  $h_{r_{dust}}$ . There is an obvious trend toward a preferred larger scale length. Both IRAS and SCUBA data can be matched to within their observed error if very large dust scale lengths are assumed. In Figure 4.12 both the width and extent of the sources are similar to that of the SCUBA images. Most importantly, the model contours are more spread out and less compact than previously seen. Figure 4.13 is the SED produced by one of the models. The sub-mm tail of the model SED is now comparable to the observed values. It is clear that to get the far end of the sub-mm wing up in the SED one needs to put more dust further out, implying that there must be more cool dust. So how much more dust is out there compared to what is observed?

The single- and two-temperature models determined the dust mass for NGC 5866 to be  $2.13\text{--}4.13 \times 10^6 M_{\odot}$ . The radiative transfer model which produced the SED in Figure 4.13 requires a dust mass of  $16.0 \times 10^6 M_{\odot}$  which is a factor of 3.9–7.5 greater than predicted by the single temperature dust model. That implies that if the dust is heated only by the general stellar population then there are large amounts of cool dust extending far beyond the stellar component. Are large dust scale length consistent with other observations?

There have been several observations that show the dust distributions in some

galaxies extend far beyond the stellar component. Two different studies in the NIR (Kylafis, Misiriotis & Papamastorakis 2001) and FIR (Radovich, Kahanpaa, & Lemke 2001) show, for a small sample of galaxies which were mapped, that the dust component extends to roughly  $1.4h_r$ . Another survey measured the extent of  $100\ \mu\text{m}$  galactic emission for 299 galaxies (Nelson, Zaritsky & Cutri 1998), finding evidence for dust emission at large radii, around 30 kpc. The scale lengths are larger than the stellar distribution, but not as extreme as indicated by Figures 4.11–4.13. However, the surveys mentioned above studied warm dust in the NIR and FIR and not cool dust in the sub-mm.

In summary, it is unlikely that the dust in NGC 5866 extends far beyond the stellar distribution. There also have been no detections of gas in NGC 5866 on scale lengths of several kpc. The fact that very large dust scale lengths are required to predict the total sub-mm flux densities may demonstrate that the models have neglected other sources of dust heating, especially those related to star formation. Although the models do produce realistic simulated galaxy images, one should include heating by young stars in the code to see how it would affect the predictions. That, however, is beyond the scope of the present work. In order to see how much dust is heated by star formation we will instead use the measured  $\text{H}\alpha$  flux to predict the contributed FIR and sub-mm flux densities.

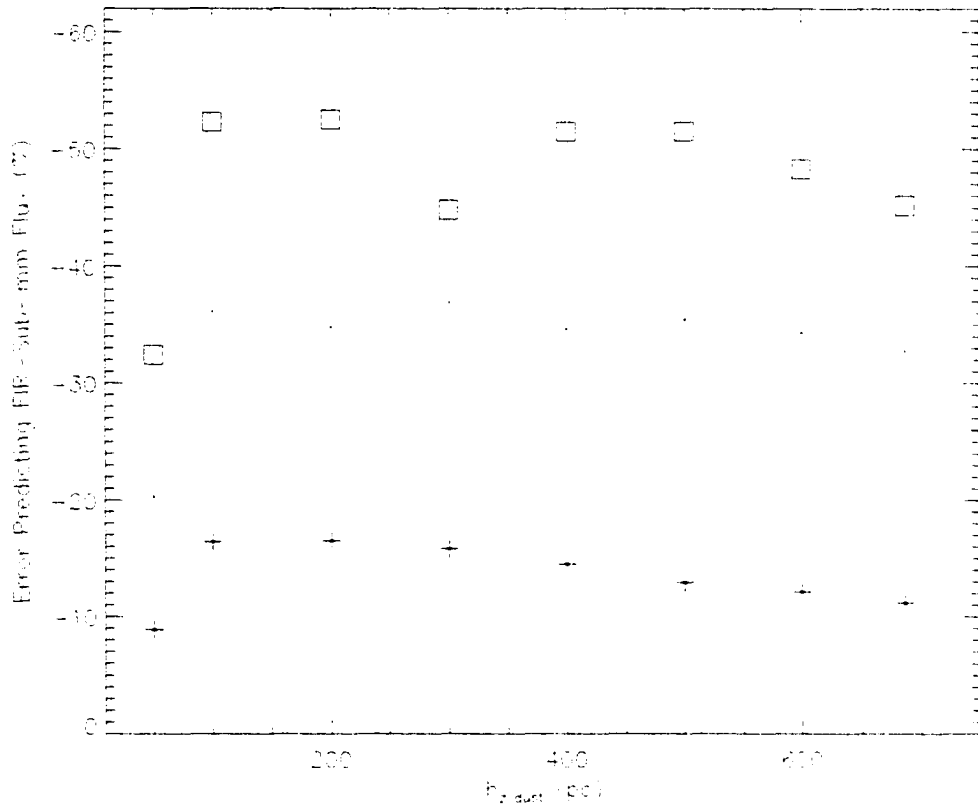


Figure 4.9: Percentage errors in predicting the SCUBA 850  $\mu\text{m}$  (box) 450  $\mu\text{m}$  (X) and the 60  $\mu\text{m}$  (star) flux density for various values of the dust scale height. In all cases  $h_{r,dust} = 2080$  pc &  $M_{bulge} = 0$ . The values are negative since the models always under predicts the SCUBA 850 and 450  $\mu\text{m}$ . The 100  $\mu\text{m}$  flux density is over predicted by same amount that the 60  $\mu\text{m}$  (star) flux density is under predicted.

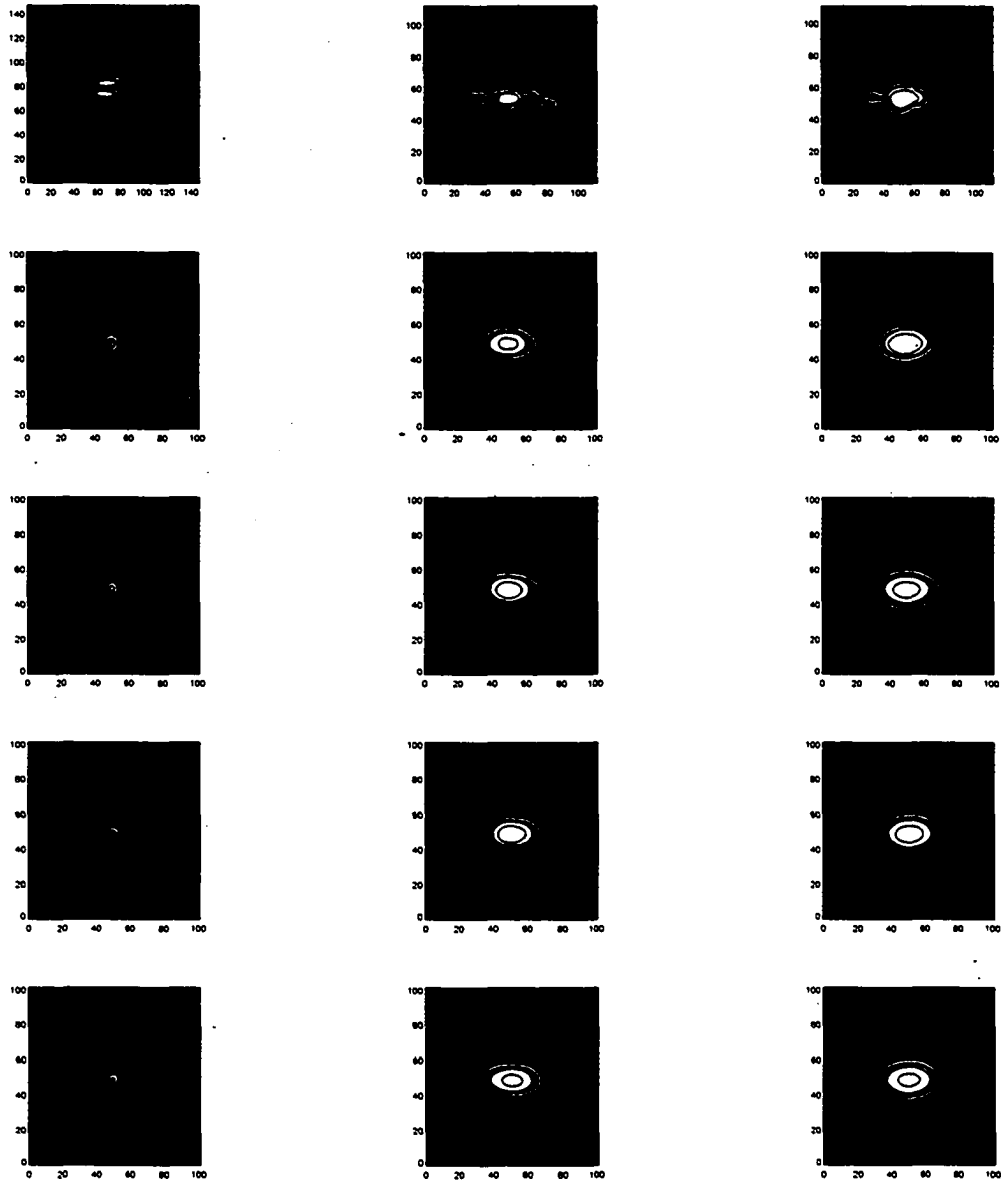


Figure 4.10: The top row: images of NGC 5866 in the V-band and 450 and 850  $\mu\text{m}$  respectively. Below are images produced by the models for comparison. The parameters for the remaining four row are:  $h_{\tau_{\text{dust}}} = 2080$  pc &  $M_{\text{bulge}} = 0$  and  $h_{z_{\text{dust}}} = 400, 500, 600, 687$  for rows 2, 3, 4, 5 respectively. The contours are one-fifth of the max value. All images are  $101'' \times 101''$ .

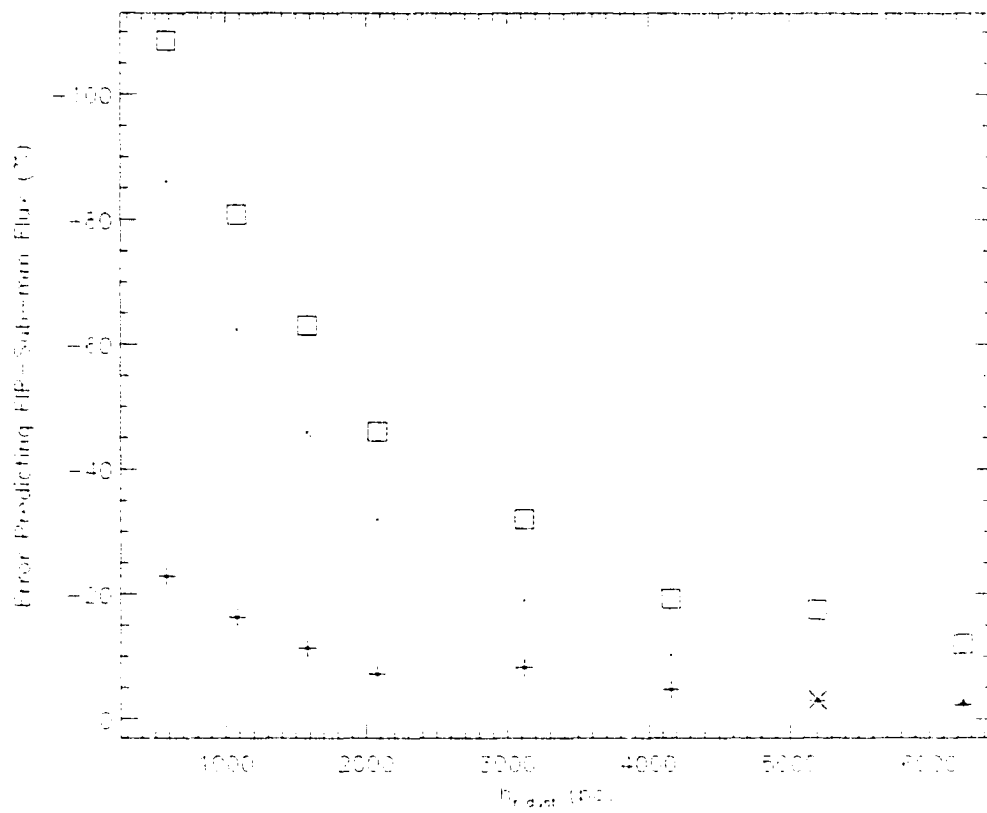


Figure 4.11: Same as Figure 4.9 except for various values of the dust scale length. In all cases  $h_{z_{dust}} = 200$  pc &  $M_{bulge} = 0$ .

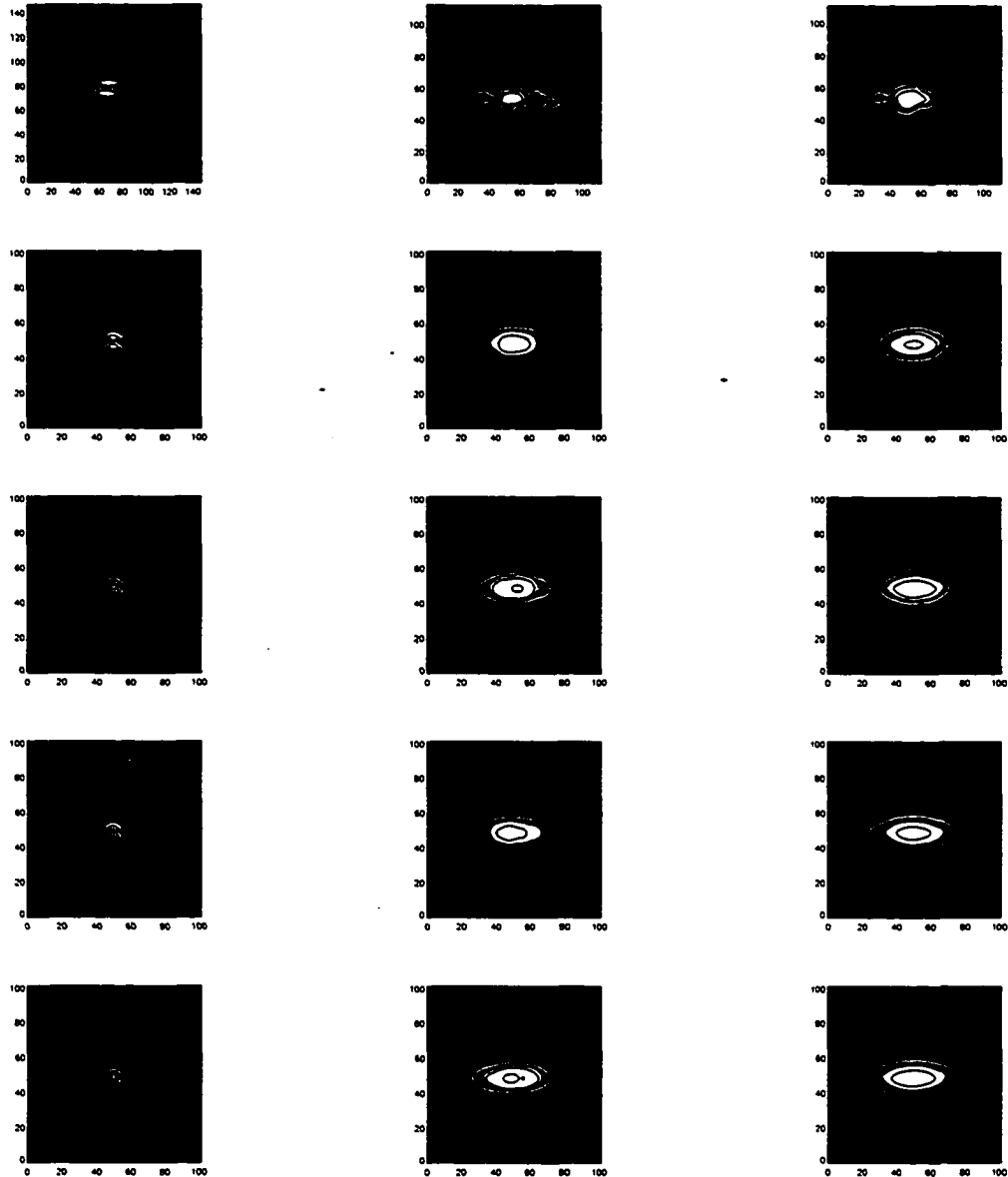


Figure 4.12: The top row: images of NGC 5866 in the V-band and 450 and 850  $\mu\text{m}$  respectively. Below are images produced by the models for comparison. The parameters for the remaining four row are:  $h_{z_{dust}} = 200$  pc, &  $M_{bulge} = 0$ ,  $h_{r_{dust}} = 3120, 4160, 5200, 6240$  pc for rows 2, 3, 4, 5 respectively. The contours are one-fifth of the max value. All images are  $101'' \times 101''$ .

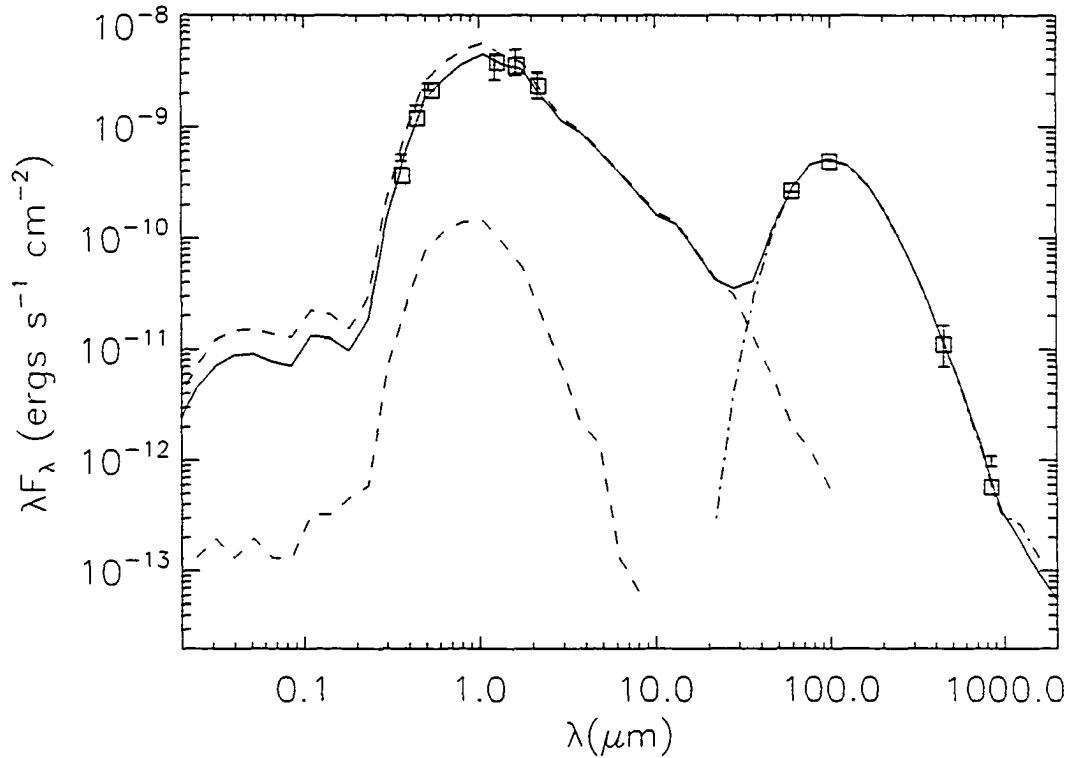


Figure 4.13: Sample SED (solid line) for NGC 5866 predicted by the Monte Carlo code for parameters  $h_{z_{dust}} = 200$  pc,  $h_{\tau_{dust}} = 3120$  pc &  $M_{bulge} = 0$ . The boxes are the predicted fluxes and the 10 data points are the observed fluxes for NGC 5866 at, respectively, U, V, B, J, H, K, IRAS 60  $\mu\text{m}$ , IRAS 100  $\mu\text{m}$ , SCUBA 450  $\mu\text{m}$ , SCUBA 850  $\mu\text{m}$ . The top dashed line represents a typical SED of a one Gyr burst model of age of 10 Gyr. The lower dashed line shows the SED of scattered emission and the dashed dotted line represents the re-radiated, thermal contribution.

## Chapter 5

# Correlated H $\alpha$ Sub-mm Emission

The dust observed by SCUBA is heated by two sources: the old stellar population and newly forming stars. Since the code being used is only able to model IR-cirrus, dust being heated by the general stellar population, we must somehow account for the dust that is being heated by newly forming stars. It is believed that NGC 5866 is undergoing star formation, as indicated by the observed H $\alpha$  emission (Plana et al. 1998). An H $\alpha$  image was obtained from Plana et al. (Figure 5.1) which was obtained on the SAO telescope using an interference filter at a central wavelength of 6586 Å and a FWHM= 14 Å. The H $\alpha$  map has a pixel resolution of 0.67'' and extends over 60'' along the major axis of the galaxy and is almost aligned with respect to the stars and dust lane. The H $\alpha$  has the same extent as the optical dust lane of NGC 5866 but it cannot be determined if the emission is produced in the dust lane. The distribution of H $\alpha$  is disk-like and the bright regions are off to one side of the galaxy and not in the center.

If dust observed by SCUBA is heated by star formation, then it is expected that the H $\alpha$  image and SCUBA images would have similar morphology. In order to qualitatively see how well the H $\alpha$  emission is correlated with the dust emission measured by SCUBA, the H $\alpha$  image was convolved with an artificial telescope beam with the same FWHM as that of the SCUBA (Sandell & Weintraub 2001) images

(Figures 5.1 & 5.3). The two convolved H $\alpha$  images were arbitrarily normalized to reduce the negative regions in the residual image and then the SCUBA images were subtracted by the normalized-convolved H $\alpha$  images as seen in Figures 5.2 and 5.4 for the 450  $\mu\text{m}$  and 850  $\mu\text{m}$ , respectively.

The disk component visible in the SCUBA 450  $\mu\text{m}$  image is no longer present in the residual. The only emission left in the residual image is a flattened and concentrated bulge. Emission in the bulge remains relatively high and maintains the same morphology as in the original image. Similar features are also present in the 850  $\mu\text{m}$  residual image. Again, the disk structure does not appear in the residual image and a dominant bulge component remains. The bulge also keeps its original morphology and the SCUBA 850  $\mu\text{m}$  is brighter in the disk on the same side as the H $\alpha$  image.

It is possible that the residual "bulge" shown in Figures 5.2 and 5.4 is an artifact produced by a large optical depth at the wavelength of H-alpha. Imagine an edge-on disk with uniform distributions of cool dust and HII regions. The optical emission would be subject to large internal extinction, so that emission would be seen only from a thin strip across the front edge of the disk. The H-alpha image would therefore show little central concentration. At the sub-mm wavelengths observed by SCUBA, however, the disk is optically thin which implies that all the dust in the disk is observable. Given the above geometry, the SCUBA maps would increase in brightness towards the center since more dust is observed along a line of sight as the center of the disk is approached. The residual of the H $\alpha$  and SCUBA images would

---

then have a strong bulge component. However, it is expected that there would be an observable gradient from the edge of the disk to the center of the residual map since the SCUBA maps increase in flux from the edge to the center. It is also worth noting that there is no such gradient observable above the signal-to-noise of the residual images in Figures 5.2 and 5.4. Since the disk subtraction does not leave any residual emission, it is plausible that the "bulge" component shown in the residual images represents emission not associated with star formation.

Except for excess "bulge" emission, the residual images show that the cool dust corresponds well with the star forming gas. The dust at  $450\ \mu\text{m}$  has very similar morphology which is expected since the radiation comes from warmer dust which is perhaps more closely related to star formation regions. It is also expected that cool dust heated by the general stellar population should be concentrated in the bulge of the galaxy since the number of heating sources are highly centrally concentrated. The similarities in the  $H\alpha$  and sub-mm emission would support the conclusion that some, maybe most, of the SCUBA signal comes from warm dust associated with star formation in the galaxy. Unfortunately we can only be qualitative here since the quantitative connection between the  $H\alpha$  emission and FIR emission from nearby dust is unknown. It is clear, however, that the FIR-sub-mm emission must be corrected for dust heated by newly forming stars if we wish to model the total flux densities correctly.

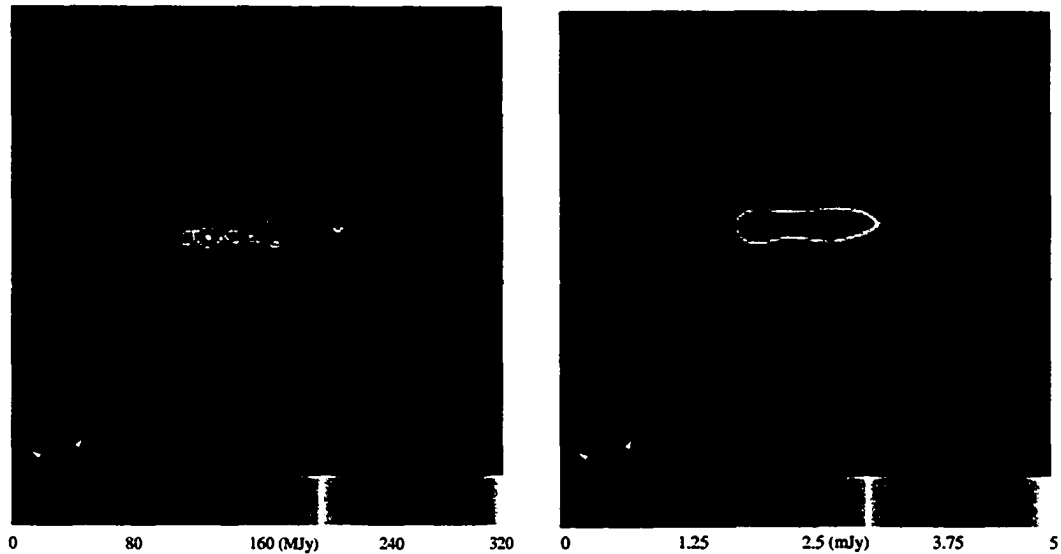


Figure 5.1: The figure to the left is a false colored  $H\alpha$  image (Plana et al. 1998) where the length of the emission is  $40''$ . The image to the right is the convolved (FWHM =  $8''$ ) and normalized  $H\alpha$  image.

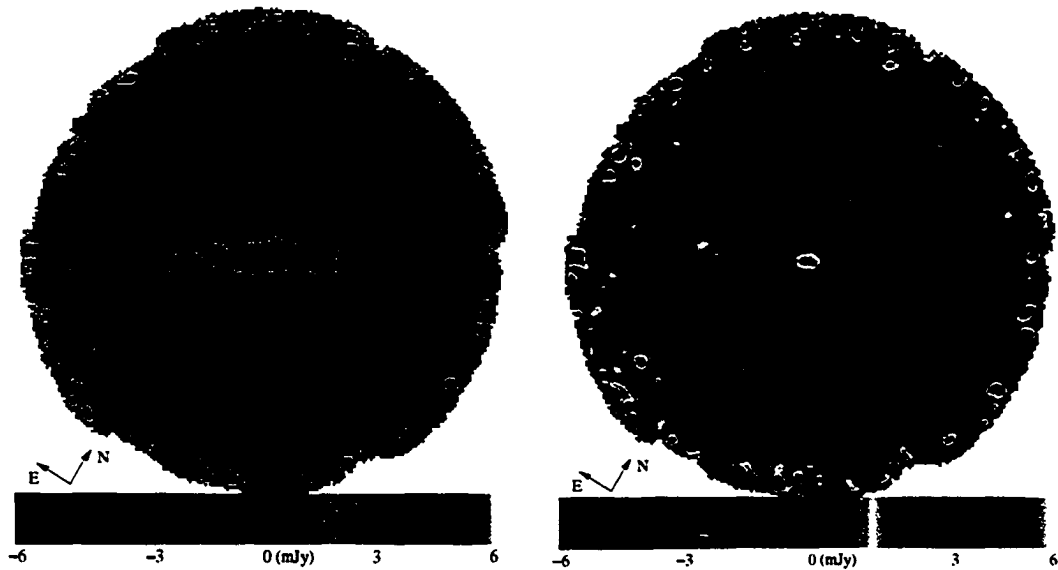


Figure 5.2: The image to the left is the same as Figure 2.8 which is a SCUBA image at  $450 \mu\text{m}$ . On the right is a subtraction of the SCUBA image by the normalized-convolved  $H\alpha$  image.

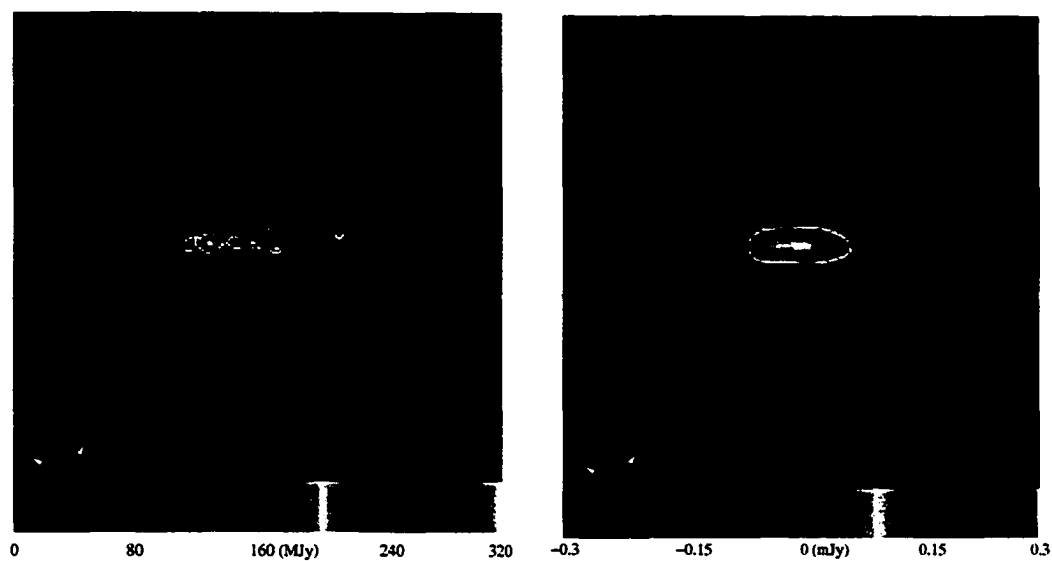


Figure 5.3: Same as Figure 4.4 except the image to the right is convolved with a beam of FWHM 15".

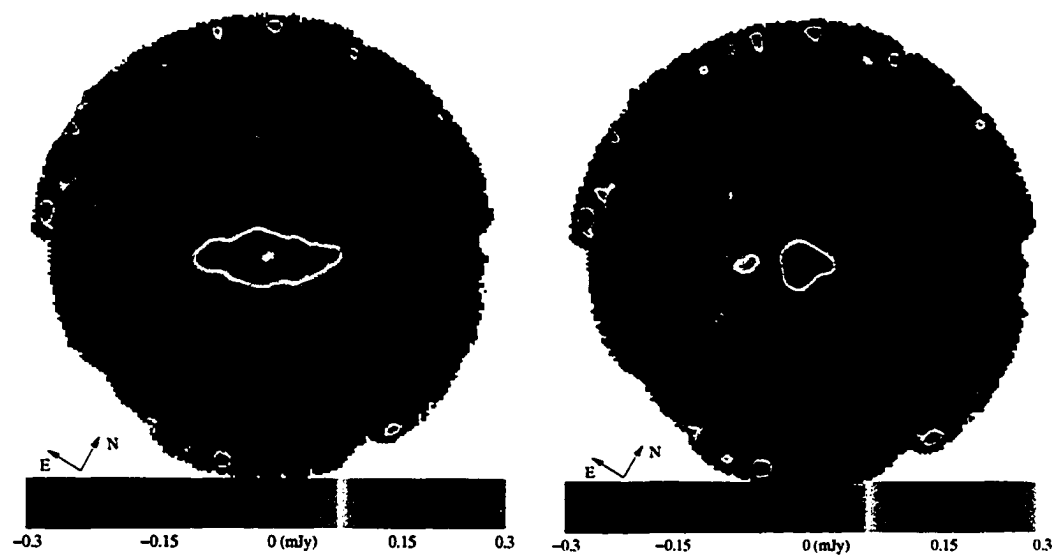


Figure 5.4: The image to the left is the same as Figure 2.9 which is a SCUBA image at 850  $\mu\text{m}$ . On the right is the result of the subtraction of the SCUBA image by the normalized-convolved H $\alpha$  image.

## 5.1 $H\alpha$ to FIR-sub-mm Conversion

The  $H\alpha$  flux of NGC 5866 is used to estimate the amount of FIR-sub-mm emission corresponding to dust heated by newly forming stars.

A recent survey of 81 nearby field galaxies was used to study the correlation of SFRs predicted by  $H\alpha$  and by FIR emission. The equation below (Kewley et al. 2002) shows a correlation between  $H\alpha$  and FIR luminosity once  $H\alpha$  was corrected for extinction in the host galaxy.

$$\log \frac{L(FIR)}{L(H\alpha)} = (0.62 \pm 0.08) \log[E(B - V)] + 2.66 \pm 0.06. \quad (5.1)$$

The color excess  $E(B - V)$  of the NGC 5866 must be determined in order to use the relation above to estimate the FIR luminosity  $L(FIR)$ .

To determine the color excess of NGC 5866, color profiles have been obtained from Peletier & Balcells (1997). They obtained optical and NIR surface brightness and color  $B - R$  profiles for the disk and bulge components of a sample of 30 nearby S0 to Sbc galaxies with inclinations larger than 50.  $E(B - R)$  was determined by taking the difference between  $(B - R)_{r=1''} = 2.096$  and  $(B - R)_{r=11''} = 1.408$  along the minor axis of NGC 5866, giving a color excess of  $E(B - R) = 0.688$ . Beyond a minor axis distance of 11'',  $B - R$  is roughly constant and therefore give a reasonable estimation of the color excess. Since  $E(B - V)$  is needed and the data in hand provide  $B - R$  profiles,  $E(B - V)$  can be estimated using Equation 5.3 as well

as incorporating Equation 5.2 the color excess can be found by (Miller & Mathews 1972);

$$\delta m_\lambda = \begin{cases} 0.74\lambda^{-1} - 0.34\lambda^{-1} & \lambda^{-1} \leq 2.29 \\ 0.43\lambda^{-1} + 0.37\lambda^{-1} & \lambda^{-1} > 2.29 \end{cases} \quad (5.2)$$

where  $\lambda$  is in microns. Equation 5.2 and the inverse wavelengths of the appropriate filters ( $\lambda_B^{-1} = 2.29 \mu\text{m}^{-1}$ ,  $\lambda_V^{-1} = 1.83 \mu\text{m}^{-1}$ , and  $\lambda_R^{-1} = 1.43 \mu\text{m}^{-1}$ ) results in a  $\delta m_B = 1.355$ ,  $\delta m_V = 1.014$ , and  $\delta m_R = 0.718$ , respectively. Equation 5.3 then gives a  $E(B - V) = 0.368$ .

$$E(B - V) = E(B - R) \left( \frac{\delta m_B - \delta m_V}{\delta m_B - \delta m_R} \right). \quad (5.3)$$

Using Equation 5.1 and  $\log L(H\alpha) = 40.49$  (Plana et al. 1998), which was correct for a distance of 15.3 Mpc,  $L(FIR) = 1.95 \times 10^9 L_\odot$ .

Since we wish to estimate the IRAS 60 and 100 micron flux densities, one further step must be taken to determine them from the FIR luminosity. The fluxes of the FIR ( $F(FIR)$ ), IRAS 60 ( $F_{60}$ ) and 100 ( $F_{100}$ ) microns are related as follows (Helou et al. 1988):

$$F(FIR) = 1.26 \times 10^{-14} F_{100} \left( 2.58 \frac{F_{60}}{F_{100}} + 1 \right) \text{ W m}^{-2} \quad (5.4)$$

where  $F_{60}$  and  $F_{100}$  are in units of Jy. To determine the  $F_{60}$  and  $F_{100}$  from Equation 5.4 a value for the ratio of  $F_{60}$  and  $F_{100}$  must be assumed.

The NGC 5866 IRAS 12 ( $F_{12}$ ) and 25 ( $F_{25}$ ) micron flux ratio is 0.097, along with the results from Helou (1986 see Figure 2), was used to determine a maximum value for the  $F_{60}/F_{100}$  ratio expected for star formation. The ratio upper limits are based on dust emission models for a range of stellar radiation fields (Désert 1986) and serves as a upper limit fit to observed color ratios. Given  $F_{12}/F_{25} = 0.097$ , the maximum expected ratio of  $F_{60}/F_{100}$  for NGC 5866 is 0.355. Now using Equation 5.4, the amount of IRAS 60 and 100  $\mu\text{m}$  flux estimated to be associated with star formation are  $F_{60H\alpha}$  and  $F_{100H\alpha}$  equal 3.98 Jy and 11.21 Jy, respectively (column 3 of Table 5.1).

Since there is no direct correlation between  $H\alpha$  and sub-mm flux, complex models are not justified for predicting the sub-mm flux from the IRAS fluxes. The same single-temperature dust model used in Section 4.1 (see Figure 4.1) will be used again here since the single temperature model was so successful in predicting the sub-mm flux densities from the original IRAS data. Using the same  $\beta$  (1.38) as before, and new IRAS best fit temperature of  $T = 29.37$  K, flux densities for 450 and 850  $\mu\text{m}$  are predicted to be 1.04 Jy and 0.16 Jy, respectively. Notice that from the simplistic model and analysis that roughly 60% of the sub-mm emission is correlated with the

same environment responsible for the H $\alpha$  emission, namely star formation (column 3 of Table 5.1).

The remaining flux (column 4 of Table 5.1) corresponds to dust heated by the general stellar population. Notice, the new  $F_{60}/F_{100}$  ratio is now 0.23 which is typical of dust only heated the general stellar population. Using those fluxes, the radiative transfer code can now be used to predict the maximum amount of dust that is heated by the general stellar population.

The information above can also be used to compute the luminosity of the IR-cirrus dust emission. Using the remaining flux from Table 5.1 (column 4) and Equation 5.4 the luminosity of the IR-cirrus dust  $L_{cirrus}(FIR) = 0.77 \times 10^9 L_{\odot}$ . The ratio of the contribution of FIR luminosity due to star formation and IR-cirrus is  $L_{\star}(FIR)/L_{cirrus}(FIR) = 2.5$ . Star formation appears to be the major heat source in the 40 to 120  $\mu\text{m}$  regime whereas the general stellar population provides less than half of the emission in the sub-mm regime. The SFR predicted for  $L_{tot}(FIR)$  is  $0.269 M_{\odot}/yr$  whereas the corrected luminosity which corresponds to star formation only  $L_{\star}(FIR)$  gives a SFR =  $0.192 M_{\odot}/yr$ . Both of those values are close to the SFR of  $0.243 M_{\odot}/yr$  determined from H $\alpha$  emission. Notice that the total FIR luminosity over predicts the SFR as many surveys have suggested since there are two components responsible for the FIR emission. The corrected luminosity corresponding to star formation slightly lower by 26% than the one determined by H $\alpha$ . The discrepancy could arise from the approximations assumed in all the calculations above.

The star formation rates can be compared to the mass return rate expected for NGC 5866. Given the blue luminosity  $L_B$  the mass return rate (Ciotti et al. 1991) is

$$\dot{M}_*(t) \simeq 1.5 \times 10^{-11} L_B t_{15}^{-1.3} \quad (5.5)$$

where  $t_{15}$  is the age in units of 15 Gyr. If we assume an age of 10 to 15 Gyr we find a ISM mass return rate of 0.430 to 0.254  $M_\odot/\text{yr}$ . The mass return rate is quite sensitive to the age of the stellar population. In either case, the mass return rate is greater than the star formation rates. Since neither of these rates are constant it is difficult to predict how much mass is expected to be observable in NGC 5866, however, it is clear that ISM should be present given that the mass return rate is larger than the star formation rate. The gas observed in this galaxy has been returned by its aging stellar population and the only reasonable source for removing the gas is star formation.

Table 5.1: FIR and SCUBA Flux Densities Before & After  $H\alpha$  Corrections

$\lambda$ ( $\mu\text{m}$ )	Flux Density (Jy)	$H\alpha$ Correlated (Jy)	IR-Cirrus Correlated (Jy)
60	$5.21 \pm 0.021$	3.98	$1.23 \pm 0.005$
100	$16.61 \pm 0.051$	11.21	$5.40 \pm 0.02$
450	$1.75 \pm 0.7$	1.04	$0.71 \pm 0.3$
850	$0.28 \pm 0.03$	0.16	$0.12 \pm 0.01$

## 5.2 IR-cirrus Dust Mass

After correcting for the amount of radiation that could be correlated with star formation, roughly 60%, the remaining flux is modeled to see what is expected to be the maximum amount of dust that is associated with IR-cirrus. Two models were run to approximate the dust mass of the IR-cirrus component. The first model uses  $M_{bulge} = 0$  which assumes that all the IR-cirrus dust is in the disk of the galaxy. The second model assumes that the mass fraction of dust in the disk of the galaxy and the bulge of the galaxy is the same as the luminosity light fraction (see Table 4.2). Both models have  $h_{r_{dust}} = 2080$  pc and  $h_{z_{dust}} = 200$ . The dust mass is adjusted for each model in order to obtain a best fit with the FIR and sub-mm data.

Figure 5.5 and Figure 5.6 are the SEDs for models with  $M_{bulge} = 0$  and  $M_{bulge} = 0.44$ , respectively. Again, the models do not correctly reproduce the observed FIR and especially the sub-mm fluxes for either set of parameters. That is unexpected since all the dust heated by star formation is removed from the model so that it should be able to simulate the flux from the remaining dust heated by the general stellar population. Also, in both cases, the model predicted  $F_{60}/F_{100}$  are 0.7 and 1.15 for  $M_{bulge} = 0$  and  $M_{bulge} = 0.44$ , respectively. Those ratios are expected for high star-forming galaxies and are not consistent with pure IR-cirrus. Again, choosing dust disk scale lengths larger than the stellar scale length could reduce  $F_{60}/F_{100}$ . The models consistently imply that even the general stellar population produces too much energy to maintain large amounts of cool gas within the galaxy.

The images in Figure 5.7 do not reproduce the SCUBA images very well, which

is expected since only 40% of the flux is present in these images. Note, however, the bulge dominant image has similar properties to the residual SCUBA and  $H\alpha$  images (Figure 5.7 row 2) where the IR-cirrus dust would be expected to be in the bulge of the galaxy.

The model is still used to approximate IR-cirrus dust mass despite the poor fit. The model where  $M_{bulge} = 0$  uses a dust mass of  $1.35 \times 10^6 M_{\odot}$ . Comparing the mass found using single-temperature dust model from Chapter 4, where  $M_{dust} = 2.13 \times 10^6 M_{\odot}$ , provides a mass ratio of the dust heated by the general stellar population to the total dust in the galaxy is  $M_{cirrus}/M_{dust} = 0.63$ . Implying that roughly 63% of the total dust mass is heating by the general stellar population, or in another words, IR-cirrus dust.

As a check, the single temperature dust models can be used to determine the IR-cirrus dust mass. Using the data from Table 5.1 (column 4), a  $\beta$  of 1.38 and a IRAS best-fit temperature of 25.83 K, the estimated dust mass is  $1.13 \times 10^6 M_{\odot}$ . That gives a  $M_{cirrus}/M_{dust} = 0.53$ , implying that a little more than half of the dust in NGC 5866 is heating by the general stellar population.

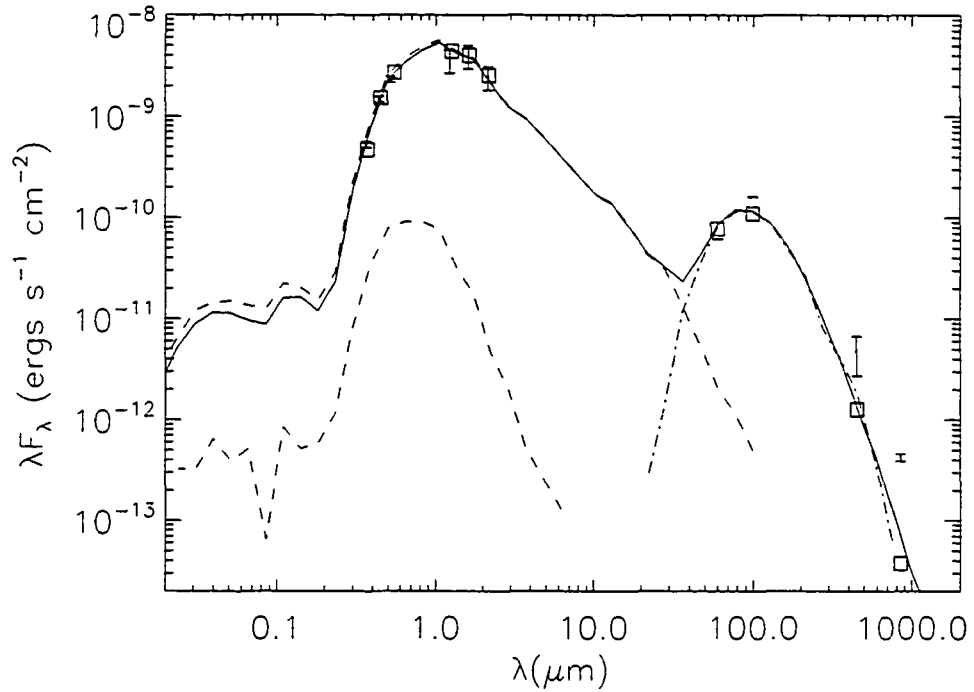


Figure 5.5: Sample SED (solid line) for NGC 5866 predicted by the Monte Carlo code for parameters  $h_{z_{dust}} = 200$  pc,  $h_{r_{dust}} = 2080$  pc &  $M_{bulge} = 0$ . The boxes are the predicted fluxes and the 10 data points are the observed fluxes for NGC 5866 at, respectively, U, V, B, J, H, K as well as the H $\alpha$  corrected IRAS 60  $\mu\text{m}$ , IRAS 100  $\mu\text{m}$ , SCUBA 450  $\mu\text{m}$ , SCUBA 850  $\mu\text{m}$  flux ( Table 5.1 column 4). The top dashed line represents a typical SED of a one Gyr burst model of age of 10 Gyr. The lower dashed line shows the SED of scattered emission and the dashed dotted line represents the re-radiated, thermal contribution.

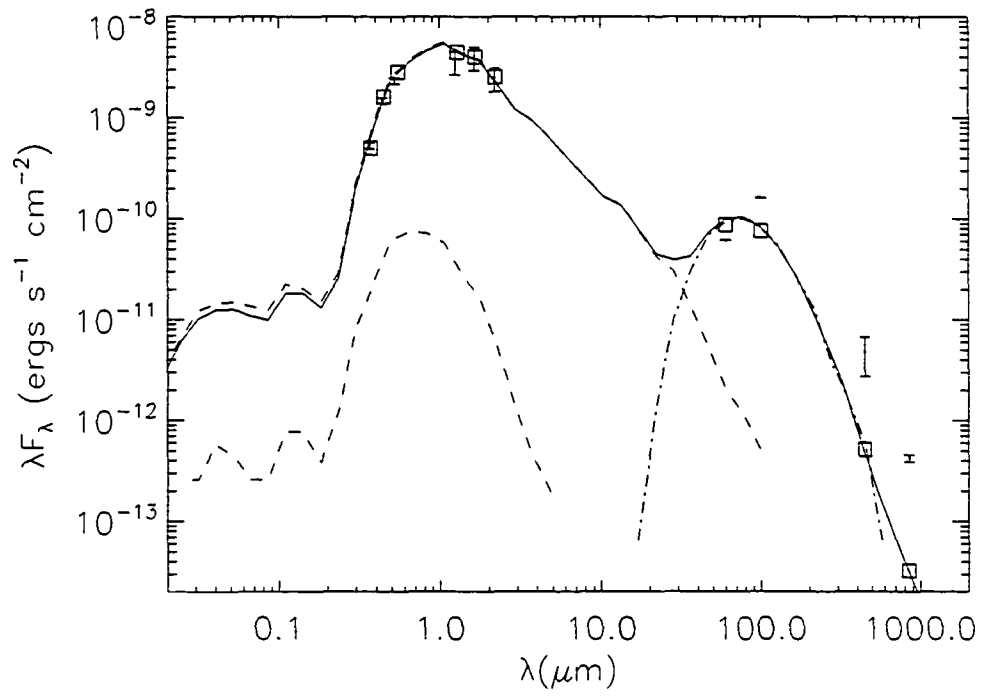


Figure 5.6: Same as Figure 5.5 except for  $M_{bulge} = 0.44$ .

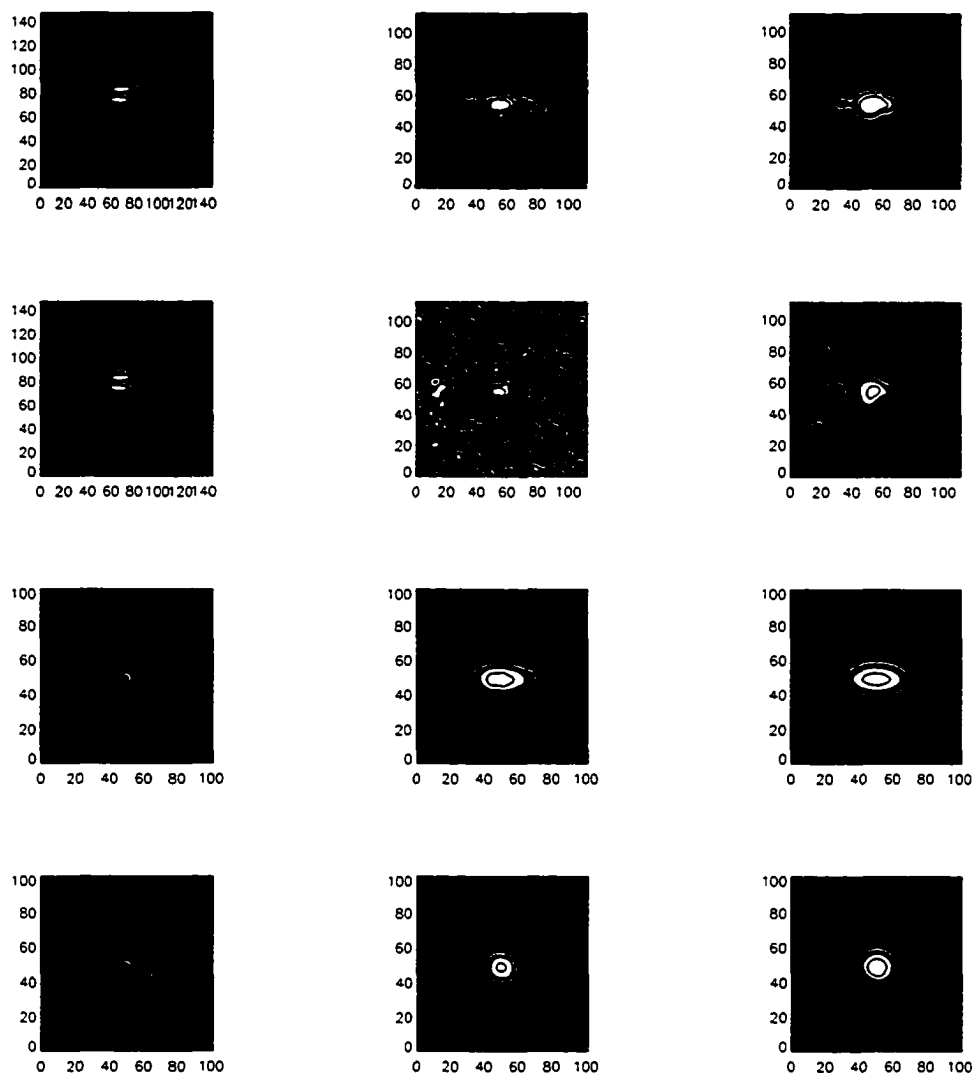


Figure 5.7: The top row: images of NGC 5866 in the V-band, 450 and 850  $\mu\text{m}$  respectively. Second row: V-band and the residual SCUBA and  $H\alpha$  image at 450 and 850  $\mu\text{m}$ . Below that are images produced by the models for comparison. The parameters for the remaining four row are:  $h_{z_{dust}} = 200$  pc,  $h_{r_{dust}} = 2080$  pc &  $M_{bulge} = 0, 0.44$  for rows 3, 4 respectively. The contours are one-fifth of the max value. All images are  $101'' \times 101''$ .

## Chapter 6

# Summary & Conclusions

The analysis of the interstellar gas component of the ISM in NGC 5866 was done using various transitions of CO as a tracer for the molecular gas. The transitions were observed on two telescopes, the IRAM and the JCMT, such that the  $J = 2-1$  transitions of  $^{12}\text{CO}$  and  $^{13}\text{CO}$  as well as the  $^{12}\text{CO}(1-0)$  had similar beam sizes of  $FWHM = 21''$ . The  $^{12}\text{CO}(3-2)$  was observed on the JCMT with a beam of  $FWHM = 14''$ . A technique was devised to find the shape of the emission source and then was artificially re-observed with a beam size of  $FWHM = 21''$ . This provided us with the unique opportunity to compare the various CO transitions without the use of uncertain beam filling factors to account for different beam sizes.

The almost all the CO transitions have similar emission features and line widths which suggest that those transitions come from the same region of gas. The  $^{12}\text{CO}(3-2)$  did not have the same line shape was reversed compared to those of the other transitions. In one particular pointing, the line shape was reverse of the other transitions. It is possible that either the pointing was off or that the  $^{12}\text{CO}(3-2)$  was emitted from a different region of gas.

The LVG analysis results in a kinetic temperature, if all CO transitions are observed from the same region of gas, of  $7\text{ K} \leq T_{kin} \leq 13\text{ K}$  and a molecular hydrogen density of  $n_H = (1.8 - 2.8) \times 10^3\text{ cm}^{-3}$ . If it is assumed that all the

transitions are emitted from the same gas except the  $J = 3 - 2$  transitions then the modeled physical conditions would still have the same molecular hydrogen density with a temperature range of  $7 \text{ K} \leq T_{kin} \leq 20 \text{ K}$ . These physical parameters indicate that the gas is cool and moderately dense. Cool and dense regions of gas are ideal for star formation. The line ratios of  $R_{21} = 0.74 \pm 0.08$ ,  $R_{32} = 0.29 \pm 0.15$  and  $R_{1213} = 8.5 \pm 2.3$  fall within the observed range of that found for star forming spirals. Those line ratios along with the temperature range and gas density reinforce the picture presented by the strong  $H\alpha$  and FIR emission that NGC 5866 is undergoing star formation.

The analysis of the dust component of the ISM in NGC 5866 was done in several steps. The first step involved modeling the FIR and SCUBA flux densities using one- and two-component single temperature dust models. Those dust models provide a good approximation of the average dust temperature and an order of magnitude approximation of the total dust mass. The best fit model to both the FIR and SCUBA data resulted in a temperature of 28.3 K for an emissivity index  $\beta = 1.38$ . The dust temperature is consistent with temperatures found in other early-type galaxies. The tight fit to the data provide no direct evidence of large amounts of cool dust unless it is too cold to contribute much signal even in the SCUBA passbands. A dust mass of  $2.13 \times 10^6 M_{\odot}$  which was determined by the models, which results in a  $M(H_2)$ -to- $M_{dust}$  ratio of 206, a factor of two higher than the Galactic value. A two component dust single temperature model was also used to model the data to get an estimate of the cool dust mass in NGC 5866. The two component model contained

hot and cool dust temperatures of 27.8 K and 11 K. It was determined that the hot dust mass is  $M_{dust\ hot} = 2.09 \times 10^6 M_{\odot}$  and the cool dust mass is  $M_{dust\ cool} = 2.04 \times 10^6 M_{\odot}$ . The model indicates that there could be roughly an equal amount of hot and cool dust residing in NGC 5866. The previous single temperature dust model does not show any evidence for cool dust. The single temperature dust models are primitive and lead only to an order of magnitude estimate of the dust mass. The total dust mass predicted by the two-component single temperature model is  $M_{total} = 4.13 \times 10^6 M_{\odot}$  which results in a  $M(H_2)$ -to- $M_{dust}$  ratio of 106 which is roughly equal to the Galactic value. Both  $M(H_2)$ -to- $M_{dust}$  ratios are consistent with ratios found in other surveys, which range between 50 and 1000 for galaxies of all types.

The second part of modeling the interstellar dust uses a more complicated three dimensional Monte Carlo radiative transfer model obtained from Kenneth Wood (Bjorkman & Wood 2001). The code is able to produce an output SED as well as images of the galaxy at any bandpass. The geometries for the stellar and dust distributions are defined by a Jaffe model for the bulge and a double exponential for the disk. The stellar Jaffe radius, scale height and scale length are fixed by observations at values of  $r_J = 3590$  pc,  $h_{r_*} = 2080$  pc and  $h_{z_*} = 687$  pc. The observed bulge to disk ratio of 0.44 is used in order to distribute the stellar light appropriately to the bulge and the disk. The dust bulge mass fraction  $M_{bulge}$ , the dust scale height  $h_{z_{dust}}$  and the dust scale length  $h_{r_{dust}}$  were free parameters in the code. The mass of the gas and dust is assumed initially to be  $4.39 \times 10^6 M_{\odot}$  (Welch

& Sage 2003). Eighty models were produced in order to constrain the three unknown parameters, assuming that the dust distribution in the disk is not greater than the stellar distribution. That assumption is supported observationally and is a standard assumption in most radiative transfer codes.

The best fit to the SCUBA images and the observed SED is achieved when  $h_{r,dust} = h_{r,*}$  and  $M_{bulge} = 0$ . The IRAS flux densities are predicted within 7% of the observed values and the SCUBA fluxes at 450 and 850  $\mu\text{m}$  were predicted within 30% and 45%, respectively. Comparing the model images and the SCUBA maps and the best fit SEDs suggest that the dust scale height ranges between  $50 \text{ pc} < h_{z,dust} < 300 \text{ pc}$ . There are however, indications in the trends seen in the predictions of the SED fluxes where a better fit can be obtained when the dust disk scale lengths are larger than stellar scale length. The results from the model images also hinted and a larger dust scale length. Further analysis demonstrated that the simulated sub-mm images and SED could match the observations only by using scale lengths greatly exceeding that of the stellar component. Those scale lengths are observationally inconsistent, which perhaps indicated that dust heated only via the general stellar populations can not account for all the emission seen in the FIR and sub-mm.

Comparing suitably convolved  $H\alpha$  images (Plana et al. 1998) to the SCUBA images reveals common features in both images, which strongly suggests that significant amount of dust emission is a result of star formation. There were no disk components left in any residual images. The only excess emission, which could possibly be associated with IR-cirrus, appeared in the bulge of the galaxy, where it

would be expected since the heating sources are more concentrated there.

We then decided that it was necessary to remove the emission due to star formation since the radiative transfer code used here only accounts for dust being heated by the general stellar population and does not include star formation. It was determined that the ratio of the contribution of FIR luminosity due to star formation and IR-cirrus is  $L_{\star}(FIR)/L_{cirrus}(FIR) = 2.5$ . Star formation appears to be the major heat source in the 40 to 120  $\mu\text{m}$  regime whereas the general stellar population provides less than half of the emission in the sub-mm regime. The SFR predicted for  $L_{tot}(FIR)$  is  $0.269 M_{\odot}/\text{yr}$  whereas the corrected luminosity which corresponds to star formation only  $L_{\star}(FIR)$  gives a SFR =  $0.192 M_{\odot}/\text{yr}$ . Both of those values are close to the SFR of  $0.243 M_{\odot}/\text{yr}$  determined from  $\text{H}\alpha$  emission. The star formation rates were compared to the mass return rate expected for NGC 5866. If we assume an age of 10 to 15 Gyr we find a ISM mass return rate of 0.430 to  $0.254 M_{\odot}/\text{yr}$ . In either case, the mass return rate is greater than the star formation rates. Since neither of these rates are constant it is difficult to predict how much mass is expected to be observable in NGC 5866. However, it is clear that ISM should be present given that the mass return rate is larger than the star formation rate. The gas observed in this galaxy has been returned by its aging stellar population and the only reasonable source for removing the gas is star formation.

To determine the cirrus dust mass, two Monte-Carlo models were used with one confining the dust to the disk and the other allowing the dust to share the same ratio as found for the light in the bulge and disk of NGC 5866. The cirrus dust mass

was estimated to be  $M_{\text{cirrus}} = 1.35 \times 10^6 M_{\odot}$ . Using the total dust mass determined by the single-temperature dust models we determine that the ratio of  $M_{\text{cirrus}}/M_{\text{dust}} = 0.63$ . Implying that roughly 63% of the total dust mass corresponds to IR-cirrus dust. Using the single temperature dust model to verify  $M_{\text{cirrus}}$ , resulted in  $M_{\text{cirrus}} = 1.13 \times 10^6 M_{\odot}$  giving  $M_{\text{cirrus}}/M_{\text{dust}} = 0.53$ . Both models suggest that around half of dust in NGC 5866 is heated by the general stellar population.

Note that in almost all the Monte-Carlo models, the sub-mm regime was under-predicted. That obvious failing deserves some discussion. There are many observational constraints placed on the model. Two constraints, stellar scale height and the bulge dust effective radius, were both approximations from observations. The stellar scale height of NGC 5866 has not been measured and was determined from studies of stellar disk scale length to scale height ratios. If the disk stellar scale height was increased, it would reduce the number density in the plane of the disk and spread out the stellar radiation over a larger area. That could lead to more cool dust in the plane of the galaxy and would not require large disk dust scale lengths to reproduce the sub-mm observations. The other constraint was that the dust effective radius was the same as the stellar distribution. If the dust has a different geometry in the bulge, such as an exponential profile or a ring, could result to an increase or decrease in sub-mm flux. Since exploring a large parameter space is computationally intensive, reasonable assumptions had to be made. Further analysis and a larger parameter space can be explored in any future studies.

All the above analysis suggest NGC 5866 has the environment to undergo star

---

formation, and in fact is presently forming stars. The idea that S0s have less gas mass than expected from monolithic models could be due to, in the case of NGC 5866, star formation. Both star formation and the general stellar population provide almost equal contributions to heating of the FIR-sub-mm dust regime. NGC 5866 may likely be entering an era of star formation fueled by its aging stellar population, which would make it a counter example of what has been assumed to be the standard ram-pressure stripped cluster S0 galaxy.

# Appendix A: CO Spectral Reductions

The software package SPECX was used to reduce the data. Since the DAS wide-band mode was used the data was stored in two overlapping subsections (called A and B) for all transitions. Each subsection samples a different portion of the total frequency window, which implies that the baseline shape and noise level might differ between subsections. To complicate things more, the CO line was centered in the middle of the total window, distributing the emission between subsections. Two reduction methods were compared: First, the two subsections of each six minute scan were concatenated (combining A and B) and a linear baseline was subtracted from the resulting spectrum. All concatenated, baseline-subtracted scans were then averaged. The second method involved removing a linear baseline from the individual subsections of each scan and then concatenating the averages of the two subsections. That was only possible since the frequency window was large enough to include a significant baseline from each subsection. Comparing the outcomes of both methods determines if the baseline tilt of each subsection is an important factor.

In the first method, a total baseline interval of  $1600 \text{ km s}^{-1}$  and  $800 \text{ km s}^{-1}$  (for the CO(2 – 1) and CO(3 – 2), respectively) is distributed equally on both sides of the line. The baselines for method two were one or the other of the above intervals

and, depending on the subsection, were located entirely on the low- or high-velocity side of the line.

Subsection B was consistently noisier, and the baseline was tilted compared to that of A. Method one, therefore, resulted in an over-subtraction of the part of the emission line in subsection B. Method two proved better able to compensate for baseline tilt in the separate subsections, and was therefore chosen for the initial reductions.

## Appendix B: CO Simplex Method

The Simplex Method, first published by Nelder and Mead (1965), uses linear adjustments of fitting parameters to modify a mathematical fitting function until some convergence criterion is met. The optimization begins with several initial trials that are set by the user. The number of initial trials is equal to the number of fitting parameters plus one. These initial trials form the first simplex. The shapes of the simplex in a one, two and a three parameter solution-space, are a line, a triangle and a tetrahedron of changing length and size. A geometric interpretation is difficult with more parameters, but the basic mathematical approach is the same. The axes in solution space correspond to values of the fitting parameters and to the value of the goodness-of-fit parameters. The latter is regarded as a function of the fitting parameters. Using the initial trial, the simplex proceeds to find the function minimum through a process of reflections, expansions and contractions of the simplex. The algorithm will converge toward a minimum following a series of contractions, and stops once the convergence criterion is met. The basic logic of the simplex method is shown in Figure B.1. The method differs from other techniques such as Gauss-Newton methods in that it does not use derivatives, which gives it well-behaved convergence properties. Hence, the Simplex Method is much less prone to finding false minima. Another nice feature of the Simplex algorithm is

---

that no divisions are required, so division by zero is not an issue.

The original code written by G. Welch was modified for the present purpose, and was tested with known Gaussian functions. The code was tested with simulated data and was successful in converging to the minima to within the set one-percent cutoff criteria. It was assumed that the solution-space was smooth and without local-minima. However, the simplex was started at numerous places in solutions-space in order to test this assumption. The Gaussian source of the gas emission for the  $J = 3 - 2$  transition was found to have an amplitude of  $346.15 \pm 33 \text{ K km s}^{-1}$ , a  $\sigma_x$  and  $\sigma_y$  of  $0.21 \pm 0.02''$  and  $7.462 \pm 0.007''$ . The uncertainties listed are the standard deviation in the output values determined by different starting values. Using this information, the source, can be convolved with any size beam necessary. For comparison with the  $J = 2 - 1$ , the source was convolved with a FWHM =  $21''$  beam to give an intensity of  $6.10 \pm 2.56 \text{ K km s}^{-1}$  where the uncertainty is determined the quadratic sums of the mean uncertainty of the 5 pointings and the standard deviation produced by the Simplex Method.

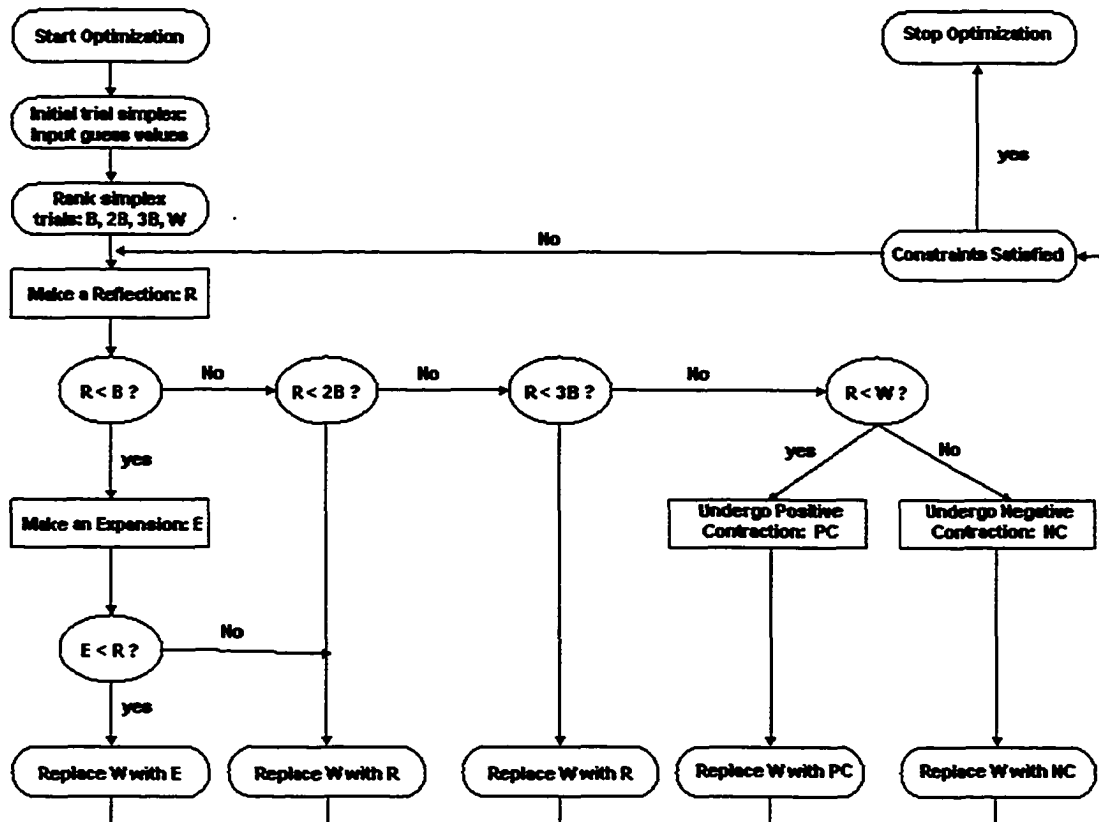


Figure B.1: This is the basic logic of the Simplex Method used to solve a three dimensional problem. The simplex is always composed of four vertexes: the best value  $B$ , a second best value  $2B$ , a third best value  $3B$ , and the worst value  $W$ . Through a series of reflections, expansions and contractions, the unknown parameters are determined within the selected constraints.

## Appendix C: LVG Model and Tests

The Large Velocity Gradient model is extensively used in deducing molecular abundances, hydrogen densities, optical depths and temperatures from mm-wave spectra. For the present purpose, three line transitions from Table 3.1 will be used to determine the hydrogen number density and the kinetic temperature of the gas.

The model pertains to a molecular cloud of uniform temperature and density with a background continuum source of temperature 2.7 K. The velocity field scales as  $v_r \propto r$ , where  $r$  is the distance from the center of the cloud.

In this model it is necessary to input an abundance factor,  $X_{CO} \equiv n(\text{CO})/n(\text{H}_2)$ , which is the number density ratio of CO and H<sub>2</sub>. The value of gradient  $X_{CO}/(dv/dr) = 1 \times 10^{-5} \text{ pc}/(\text{km s}^{-1})$ , which is typically assumed, is used here (eg: Wilson, Howe, & Balogh (WHB) 1999; Li, Seaquist, & Sage (LSS) 1993). The model was tested by recreating the graphs of WHB and LSS. Figure C.2 shows a recreation of the plot from LSS (red) using the present model (black). Minor discrepancies may arise through the use of different collision rates and cross sections. The models agree quite well in the region of interest and deviate only at higher temperatures and densities.

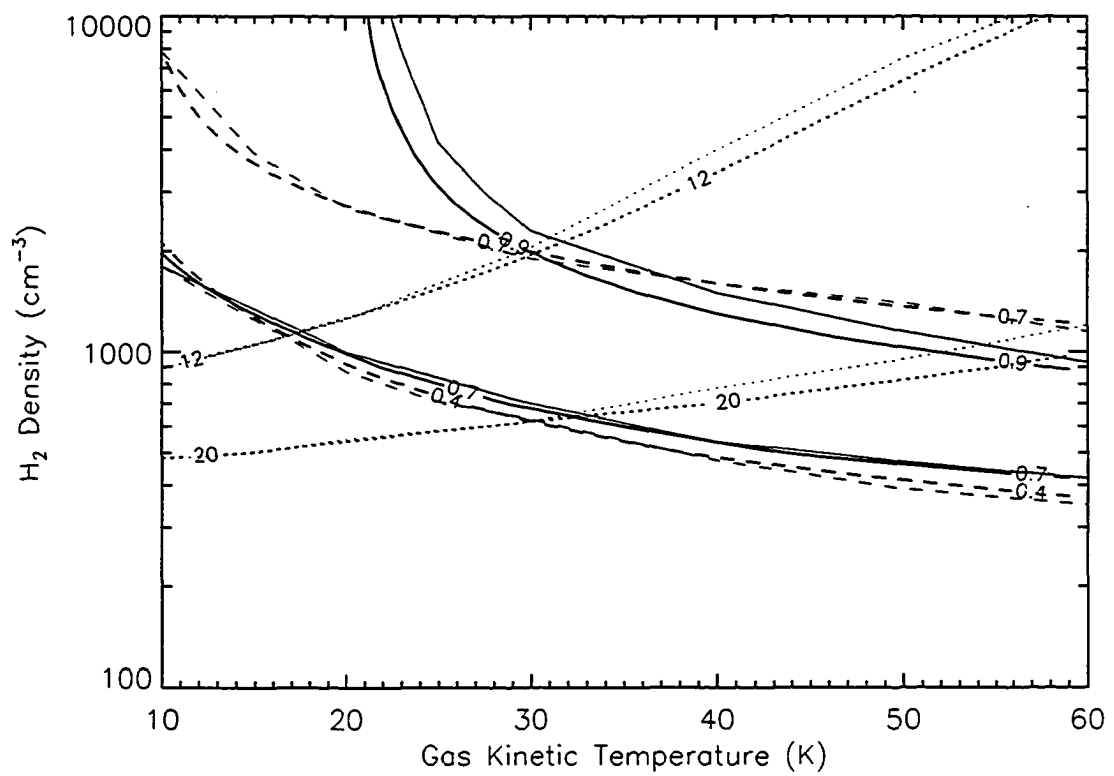


Figure C.2: LVG models from Li, Seaquist, & Sage (1993) in red compared to the models that we use for our analysis in black.

---

## Appendix D: SCUBA Data Reductions

This section describes steps taken to reduce the SCUBA data for NGC 5866, and NGC 3607 which was not used in this thesis, obtained on December 20th and 22nd of 2001. ORAC-DR was used to obtain first looks at the data; SURF was used for the final reductions

ORAC-DR is a pipeline data reduction system intended for real-time reduction of incoming data. Its output is generally not of publication quality, however it is useful in assessing the quality of the data. The pipeline software reduces the data by calling up recipes, each of which contains a list of individual data reduction steps. A step is a SURF primitive, which performs one reduction task. Directly using the primitives, allow more flexibility in the SURF reduction package. SURF is the preferred tool for reducing SCUBA data, since it gives freedom to modify reduction tasks; in ORAC-DR the entire process is fixed and difficult to change. ORAC-DR may be satisfactory when it comes to bright, small, spherically symmetric sources, but it is not effective for faint extended ones like NGC 5866. A good exercise is to first use SURF to follow the same procedure as ORAC-DR in order to understand the inner workings of ORAC-DR and become familiar with SURF.

As a test, the ORAC-DR procedure was duplicated in SURF using one full

night of observations of NGC 5866. The difference of the two reduced images was a smooth, uniform image with an average value of  $10^{-3}$  mJy/beam. That is, both maps are identical to  $10^{-3}$  mJy/beam. A possible reason for a non-zero result is the finite number of significant figures stored by the programs.

The next step is to use SURF to improve on the data reduction procedure followed in ORAC-DR. A flowchart showing the refined method is displayed in Figure D.3. Multiple observations made on the same date can be fully reduced, as well as combined, by following those basic commands.

The jiggle-map mode was used for the mapping the galaxies at 450 and 850 microns. That involves "jiggling" the secondary mirror by 3.09" over 64-positions to produce a fully sampled map at both wavelengths. The secondary mirror also chops the source against a reference position using a chop throw of 180" offset in Azimuth at a frequency of 7.8 Hz. An additional nodding of the telescope, which interchanges source and reference positions every 10–20 seconds, is used to help reduce the effect of sky emission.

Each 64-point jiggle map, defined as an integration, must be reduced separately. First, the SURF task REDUCE\_SWITCH is used to subtract the nod off-position from the on-source position. The FLATFIELD task is then applied to the output of REDUCE\_SWITCH to flat-field the image by multiplying each bolometer signal by the volume flat-field value which is incorporated within the data files. Next, it is necessary to correct for the atmospheric attenuation of the signal.

There are two methods of measuring the opacity ( $\text{Tau} = \tau$ ) of the atmosphere:

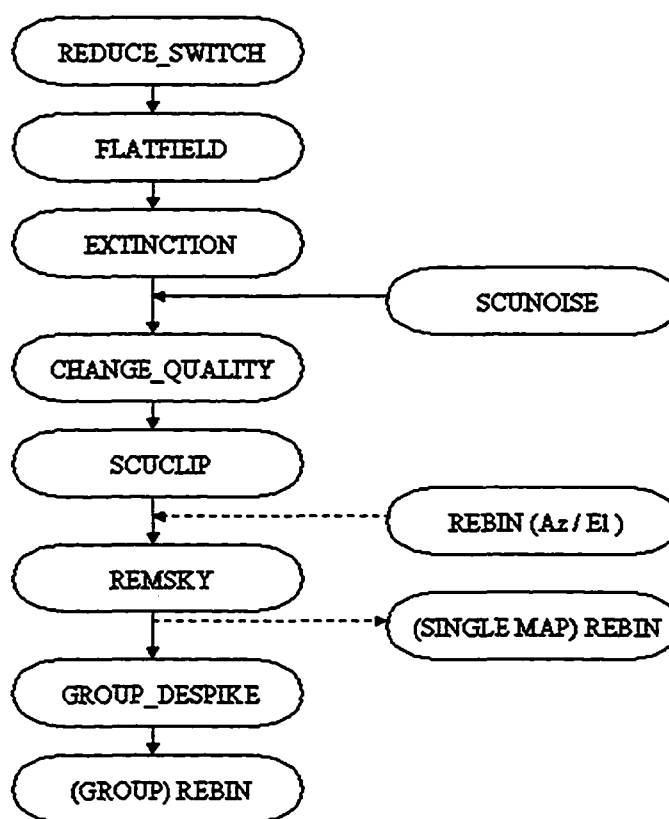


Figure D.3: SCUBA reduction procedure.

from a JCMT skydip at the observing frequency, and from the CSO sky monitor, which measures the zenith sky opacity at 225 GHz every ten minutes. Comparing the skydip values to the  $\tau_{CSO}$  values yields scaling relations between  $\tau_{CSO}$ ,  $\tau_{850}$  and  $\tau_{450}$ . Since skydips are time consuming, visiting observers use the  $\tau_{CSO}$  monitor to measure the opacity close to the time of the observations. The latest scaling relations are (see JCMT SCUBA calibration page);

$$\tau_{850} = 4.02 (\tau_{CSO} - 0.001) \quad (\text{D.1})$$

$$\tau_{450} = 26.2 (\tau_{CSO} - 0.0014) \quad (\text{D.2})$$

We have obtained polynomial FITS to measurements of  $\tau_{CSO}$  taken at various times on both nights (Moriarty–Schieven 2002). Knowing how the  $\tau_{CSO}$  behaves as a function of time and using the relations above, the zenith opacity of the atmosphere can be determined at 850 and 450 microns during the time of the observations. The UT time at the start of each map can be found in the fits header. The task EXTINCTION is used once zenith opacity is determined. Since sky opacity changes significantly between 850 microns and 450 microns, the long and short wavelength data sets are separated at this point and reduced independently thereafter. The next step is to discard any bolometers that were noisy during the observation period.

It is important to remove noisy bolometers and to do an initial removal of hot pixels (despiking) before sky subtraction, so that a more accurate value for the sky

---

brightness can be obtained. The most effective way to identify noisy bolometers is by using the command SCUNOISE, which displays the output of each bolometer during the noise measurements. There are 128 bolometers in all, 37 and 91 in the long and short wavelength arrays, respectively. Bolometers are deemed too noisy if their output is above 100 nV, and the SCUBA Users Guide recommends that any bolometer with a noise level of over 500 nV be switched off. The majority of the bolometers should have a typical noise level around 40 nV. There are usually a few noise measurements which can be used to identify bolometers that are continuously noisy as oppose to bolometers that had an occasional high reading. Bolometers that are noisy throughout the observing run can be removed using the CHANGE\_QUALITY command. Changing a bolometer to 'bad' will remove the data obtained with that bolometer. The present data set comprises measurements of the same object taken over several hours so, due to the rotation of the sky, removing the input from a few bolometers does not necessarily produce 'holes' in the final map. A total of two 850 micron sky bolometers were set to bad for the data set for each night. The 450 data was very noisy on the second night where 16 bolometers were set to bad, as opposed to only one bad bolometer on the first night.

The extinction corrected data set was initially despiked (SCUCLIP) at the  $5\sigma$  level. In that process the noise output of each bolometer is analyzed independently, the median and standard deviation are calculated, and any data greater than five sigma from the median are removed. In the jiggle-map mode, however, the despiking algorithm is only useful for weak sources since small, bright sources will also be

removed.

Before the sky can be subtracted, one must identify the sky bolometers for each integration separately. The rotation of the source between integrations is significant, so sky bolometers must be identified for each integration. Since the sources are extended and faint, care must be taken in choosing the sky bolometers. The individual maps must be REBINed in azimuth in order to overlay the bolometer positions using SCUOVER so one can visually select the sky bolometers. The task REMSKY is then used to remove the sky signal. It does this by using the sky bolometers chosen to calculate an average value for each integration and then subtracting the sky value from that integration. If there is only a single integration of the source, one can rebin the data back to the *RA, DEC* frame and the reduction is complete. However, the present project involves multiple integrations so an additional step is required.

A group despike (DESPIKE NOLOOP) of all the maps is the best way to remove spikes since it uses all the integrations from one night. A pixel whose output differs from the median of the pixels of all the integrations by more than  $3\sigma$  will be removed. The method is applied once all the previous steps have been completed. The despiked integrations are REBINed to create a final map of all the data acquired for one night. Pointing corrections are not applied to any of the integrations, since there was no change in the position of the brightest pixel between individual integrations. Furthermore, more experienced SCUBA users report that pointing corrections seldom necessary. (Moriarty-Schieven 2002).

---

To calibrate the data the standard source IRC+10216 was observed once on the first night and twice on the last. The reduction path described above was also followed for the calibrators. No spikes were removed in the DESPIKE procedure. That was important to verify since IRC+10216 is a bright, compact source which could possibly mimic a noise spike. In order to determine the calibration value, the brightest source pixel value which is in units of volts, must be determined. Consulting the JCMT SCUBA calibration website will indicate what the peak intensity should be for the calibration source used. In the case of IRC+10216, and other variable sources, equations derived from many observations are provided to determine the intensity of the source as a function of time. The calibration value for each wavelength is determined by dividing the predicted observed intensity by the peak pixel values. The average of the three values for each wavelength,  $239 \pm 19 \text{ Jy beam}^{-1} \text{ V}^{-1}$  and  $325 \pm 78 \text{ Jy beam}^{-1} \text{ V}^{-1}$  for 850 and 450 microns respectively, were used to multiply the pixel values in the images of NGC 5866 and NGC 3607. The standard deviation of the pixel values added in quadrature to the uncertainty in the measured flux of IRC+10216 is used for the uncertainty in the flux per beam of the galaxies. The maps are now in calibrated units of Jy/beam. To convert the maps to units of Jy, One must multiply by the effective area of the beam.

NGC 5866 was observed for a total of 30 minutes on the 20th and for 60 minutes on the 22nd. NGC 3607 was observed for 30 minutes on the 20th and for 40 minutes on the 22nd. Final images were produced by averaging the results from both nights using weights proportional to the nightly integration times. The tool KAPPA, which

allows one to do simple image math, was used to multiply the images by their weights. The weights for each map are equal to the integration time on the source for one night divided by the sum of the total time for both nights.

## Appendix E: Simulated SED Fit to Optical & FIR Data

In order to appropriately simulate the FIR–sub–mm data, the optical luminosity of the input spectrum must be calibrated such that it matches that of NGC 5866. The Bruzual and Charlot model chosen must be adjusted such that it is normalized to that of the observed UBVJHK fluxes found in Table 4.3. This can be done by adjusting the parameter  $L_{\nu_o}$  (see Table 4.2). Since the parameter space in the first round of models is large, the normalization of the SED is not expected to remain the same for each model. However, one model was normalized and used the same  $L_{\nu_o}$  for all the remaining 63 models. That will not affect the results since it is possible to look at the relative predictions in the FIR–sub–mm instead of the absolute predicted fluxes. If for example, due to the poor fit of  $L_{\nu_o}$ , a model under predicts all the fluxes in the FIR–sub–mm regime by approximately the same amount, then  $L_{\nu_o}$  and  $M_{dust}$  can be adjusted such to obtain a good fit for the optical and FIR–sub–mm regimes by adjusting these parameters respectively.

The model chosen to normalize accurately was for  $h_{\tau_{dust}} = h_{\tau_*} = 2080$  pc,  $h_{z_{dust}} = 100$  pc and  $M_{bulge} = 0$ . The mass of gas and dust  $M_{ISM}$  will be set to  $4.39 \times 10^8 M_{\odot}$  (Welch & Sage 2003) for the first round of models. The simplest way to do a fit would be to adjust  $L_{\nu_o}$  until a reduced  $\chi^2$  is minimized. Short simulations,

which took about 15 minutes CPU time, while varying  $L_{\nu_0}$  was done in order to find a minimum reduced  $\chi^2$ . Figure E.4 displays the points at which that model was run for a specific  $L_{\nu_0}$  as well as a fit by a third order polynomial. The best fit occurred when  $L_{\nu_0} = 5.92 \times 10^{10} L_{\odot}$ . That value is used for all of the first round models.

Just as a sidestep, I would like to explain what a short run model consist of. Recall that the Monte Carlo code is based on a technique where individual photons are followed around the galaxy, basically a bookkeeping of the interactions taking place until all the photons escape the galaxy. The time it takes to run the code depends entirely on how much bookkeeping is involved, which is proportional to the number of photons that are put into the system. Simulations can be shortened in run time by using fewer photons. A full model, which provides the required image quality, uses  $10^7$  photons, and for a short model  $10^6$  photons are used. The decrease of an order of magnitude in the photons roughly translates into an order of magnitude lower run time. A short run provides a reasonably accurate SED but does not have enough photons to produce the quality of images necessary for the analysis. Thus, short models are used for normalization purposes and long runs are used to produces the final SEDs and images.

It was clear that the quality of the fit to the optical data varies a lot. Figure E.5 shows the reduced  $\chi^2$  for the 64 models. The dust scale heights are binned into groups of four corresponding to a dust scale length and  $M_{bulge}$ . For example, the set of models run for  $h_{r_{dust}} = 580$  pc,  $M_{bulge} = 0$  and  $h_{z_{dust}}(\text{pc}) = [50, 100, 200, 300]$  represents one point. The error bars represent the standard deviation from the

mean for the different  $h_{z_{dust}}$ . Notice that the dispersion is less at a  $h_{r_{dust}} = 2080$  pc since this value is used for the normalization when  $h_{z_{dust}} = 100$ pc.

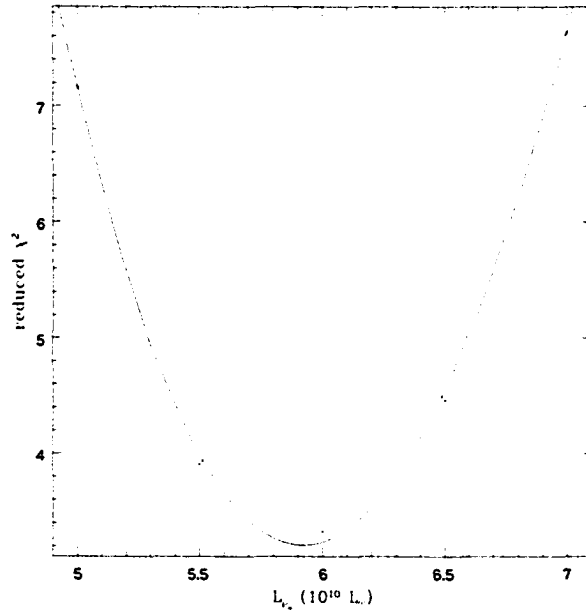


Figure E.4: A minimum in the reduced  $\chi^2$  was determined between the input SED and the optical data by fitting a third order polynomial (line) through five models at different  $L_{\nu_o}$ s (points).

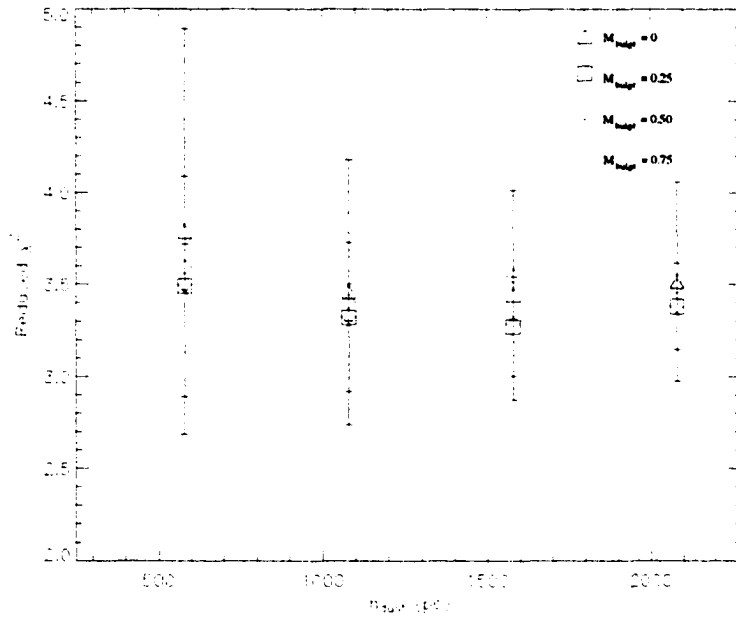


Figure E.5: Reduced  $\chi^2$  for the 64 models where the dust scale heights  $h_{z_{dust}}$  (pc) = [50, 100, 200, 300] are binned into groups of four corresponding to a dust scale length and  $M_{bulge}$ . The error bars represent the standard deviation from the mean for the different  $h_{z_{dust}}$ .

---

## Appendix F: Model Images

The following images are from the Monte–Carlo models. The top row of all the following Figures F.6–F.21 are, from left to right, the V–band, SCUBA 450 and 850  $\mu\text{m}$  images of NGC 5866. The remaining four rows are created with the parameters listed below them but do have in common that rows 2, 3, 4, 5 have increasing bulge mass fraction  $M_{bulge} = 0, 0.10, 0.25, 0.5$  respectively. Each image is displayed on each axis as a function of pixels. The observed images were adjusted such that they can be directly compared to the simulated images. This means that all images have a total box size of  $101'' \times 101''$ . The V–band and SCUBA 450 and 850  $\mu\text{m}$  are on different scales because they have a resolution of 0.693, 0.819 and 0.839  $''/\text{pixel}$ , respectively.

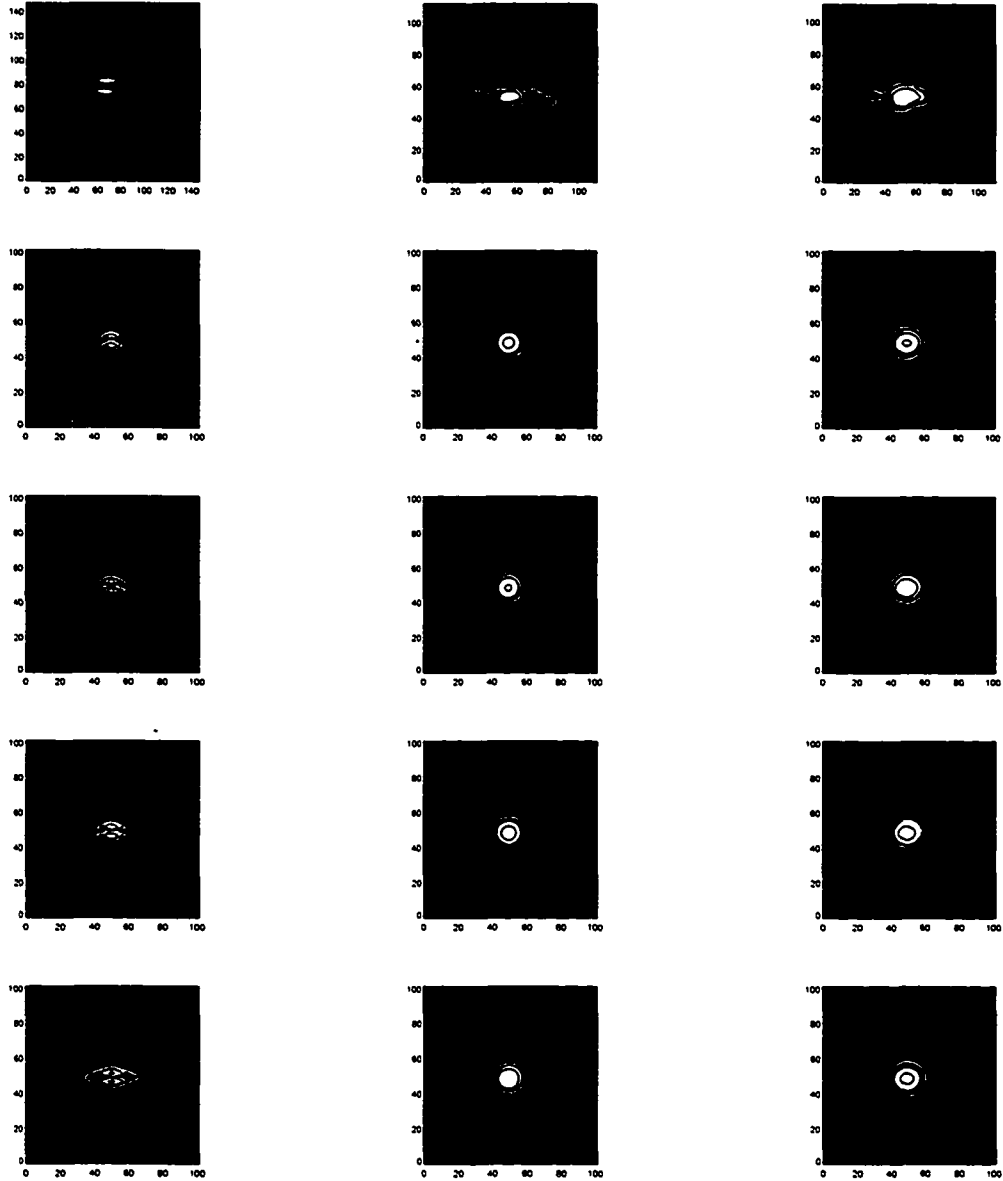


Figure F.6: The top row (from left to right): images of NGC 5866 in the V-band and 450 and 850  $\mu\text{m}$  respectively. Below are images produced by the models for comparison. The parameters for the remaining four rows are:  $h_{z_{dust}} = 50$  pc,  $h_{r_{dust}} = 580$  pc &  $M_{bulge} = 0, 0.25, 0.5$  for rows 2, 3, 4 respectively. The contours are one-fifth of the max value. All images are  $101'' \times 101''$ .

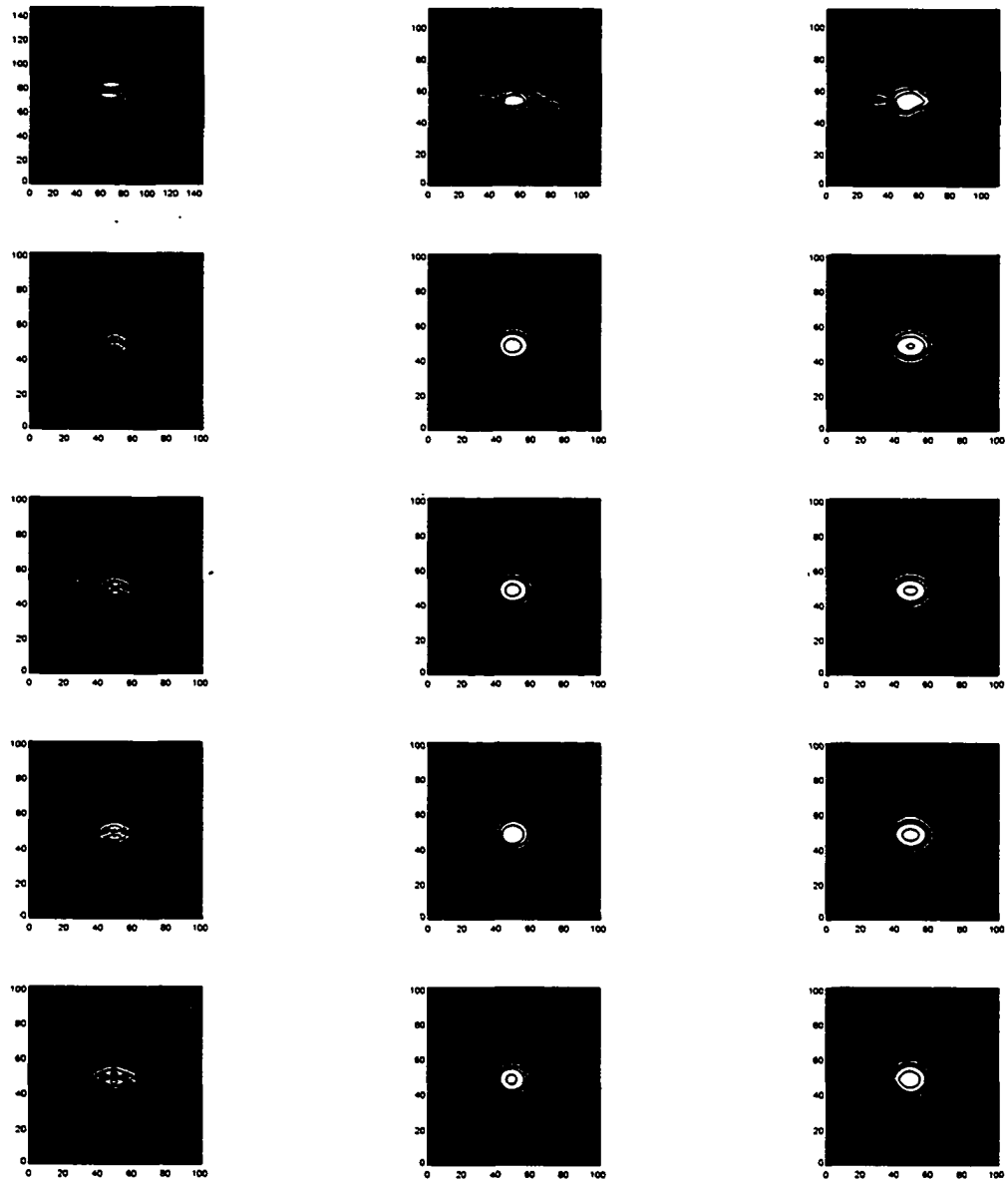


Figure F.7: Same as Figure F.6 except  $h_{r_{dust}} = 1080$  pc

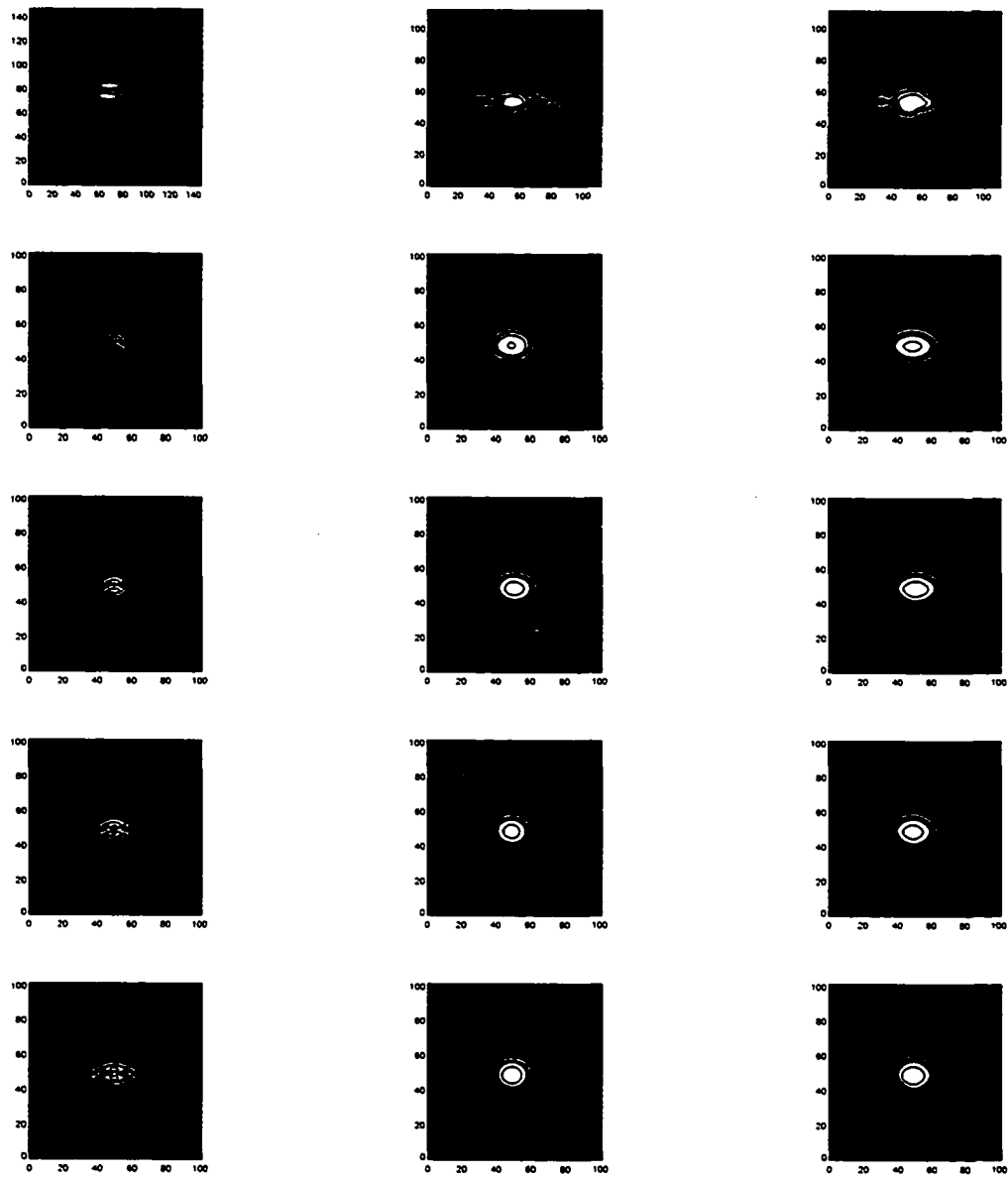


Figure F.8: Same as Figure F.6 except  $h_{r_{dust}} = 1580$  pc

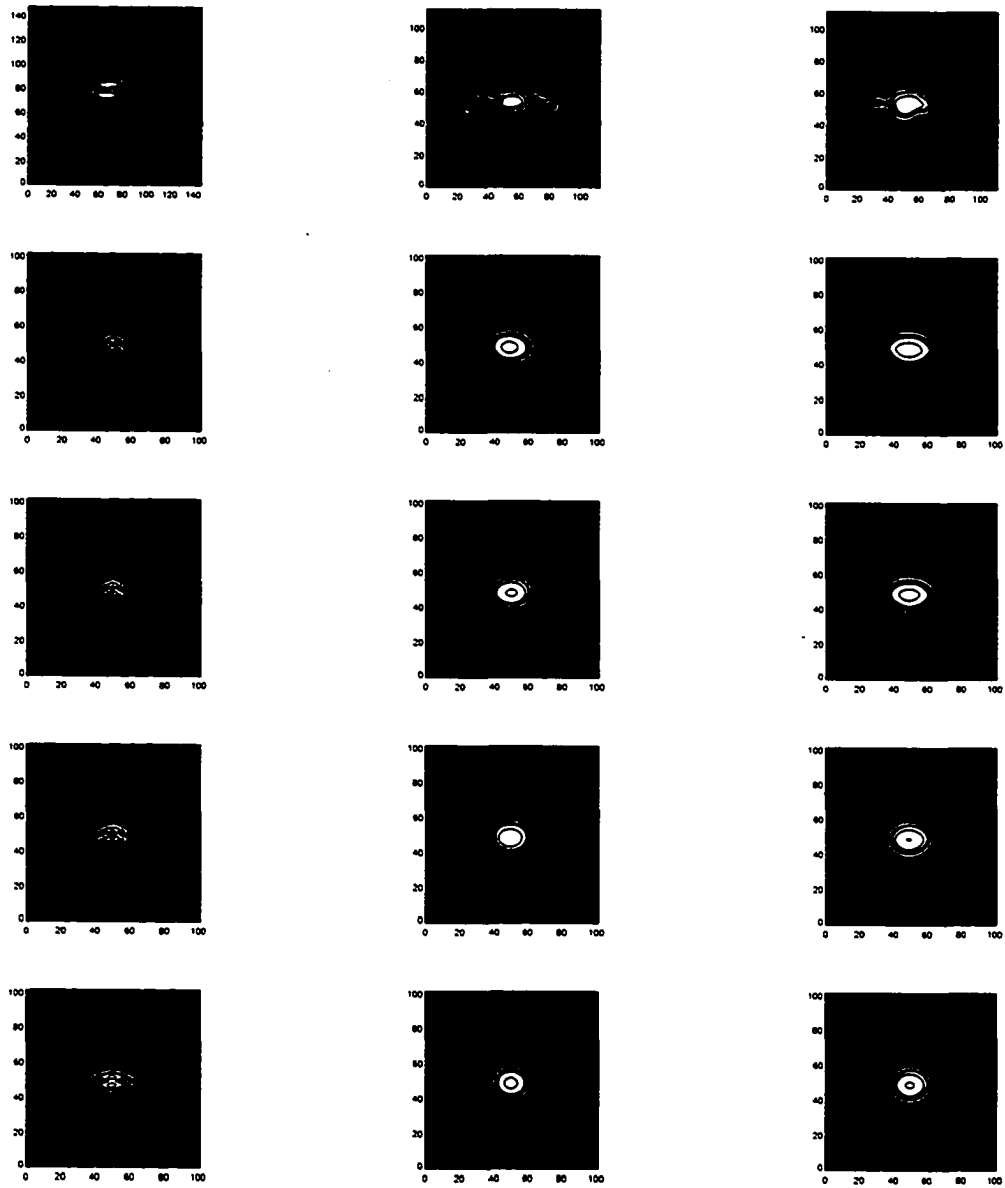


Figure F.9: Same as Figure F.6 except  $h_{r_{dust}} = 2080$  pc

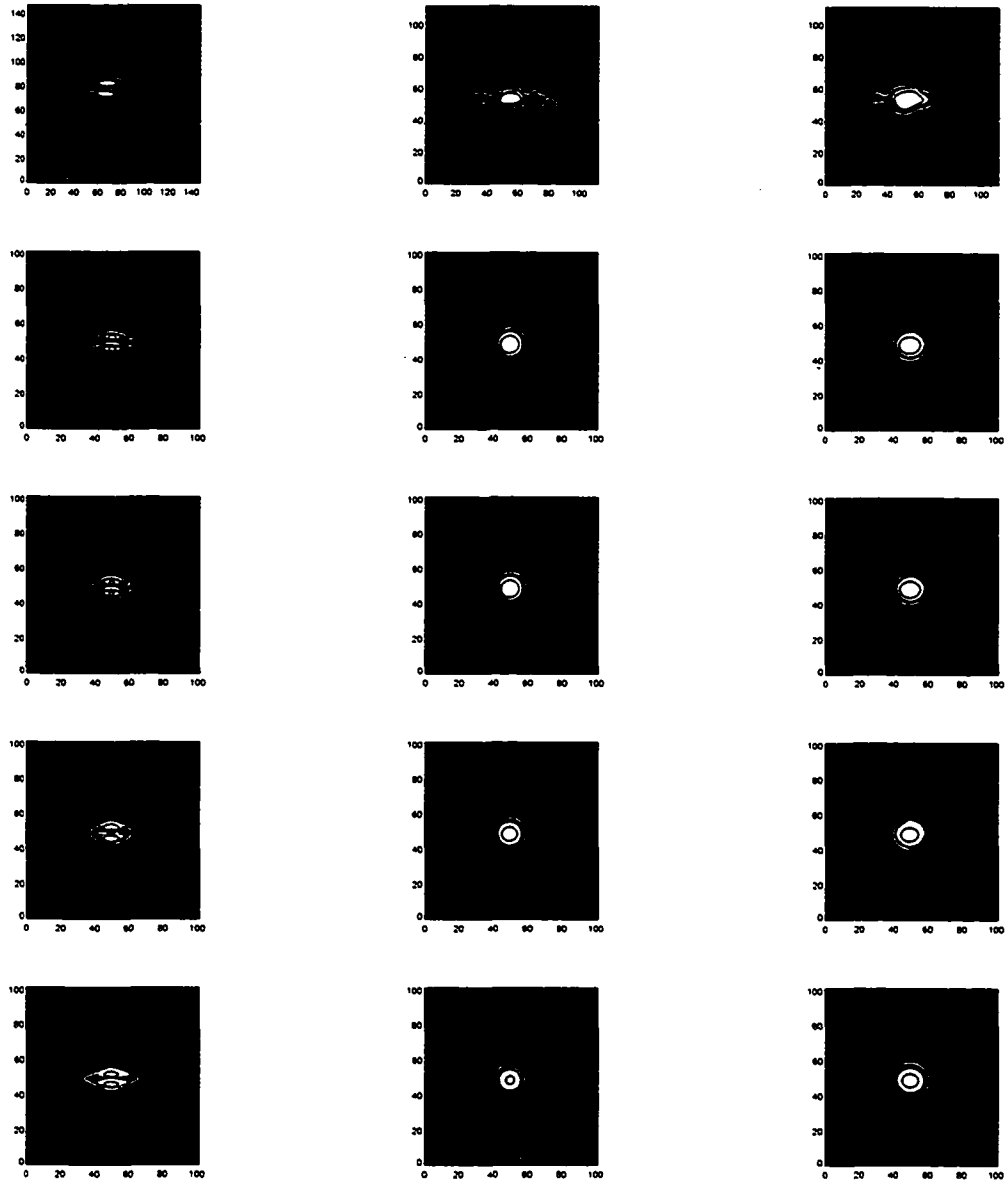


Figure F.10: Same as Figure F.6 except  $h_{z_{dust}} = 100$  pc &  $h_{r_{dust}} = 580$  pc

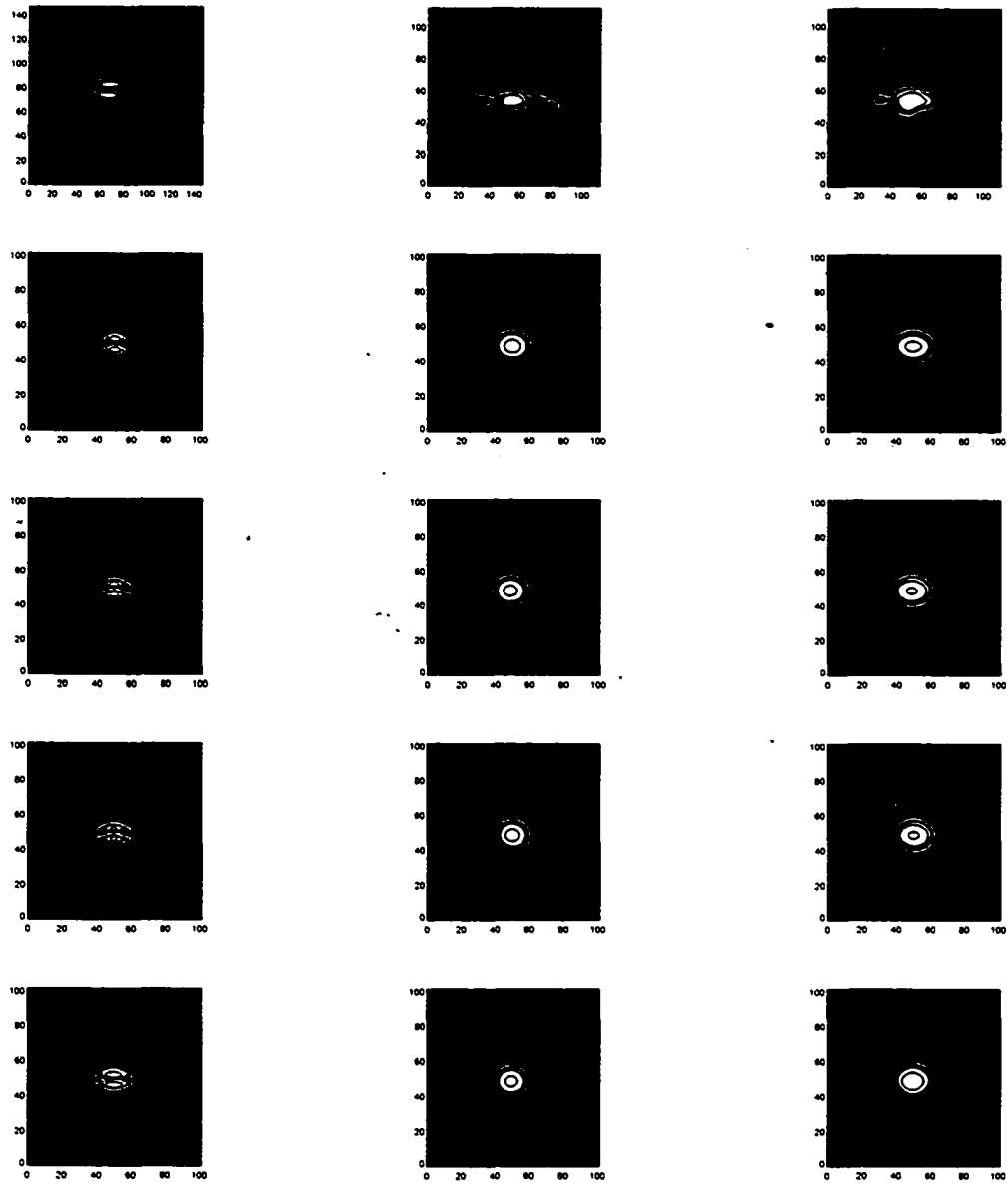


Figure F.11: Same as Figure F.10  $h_{\tau_{dust}} = 1080$  pc

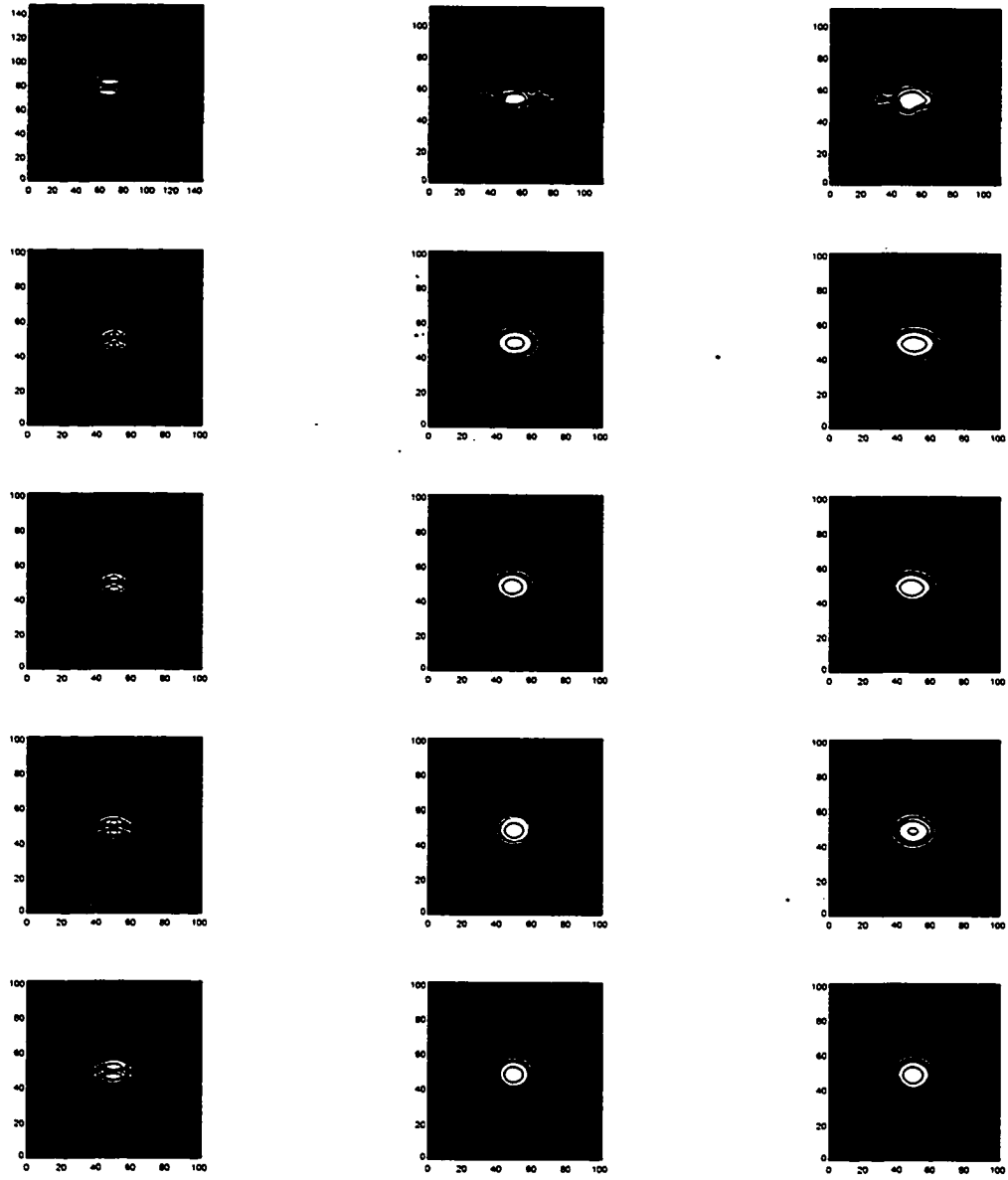


Figure F.12: Same as Figure F.10 except  $h_{r_{dust}} = 1580$  pc

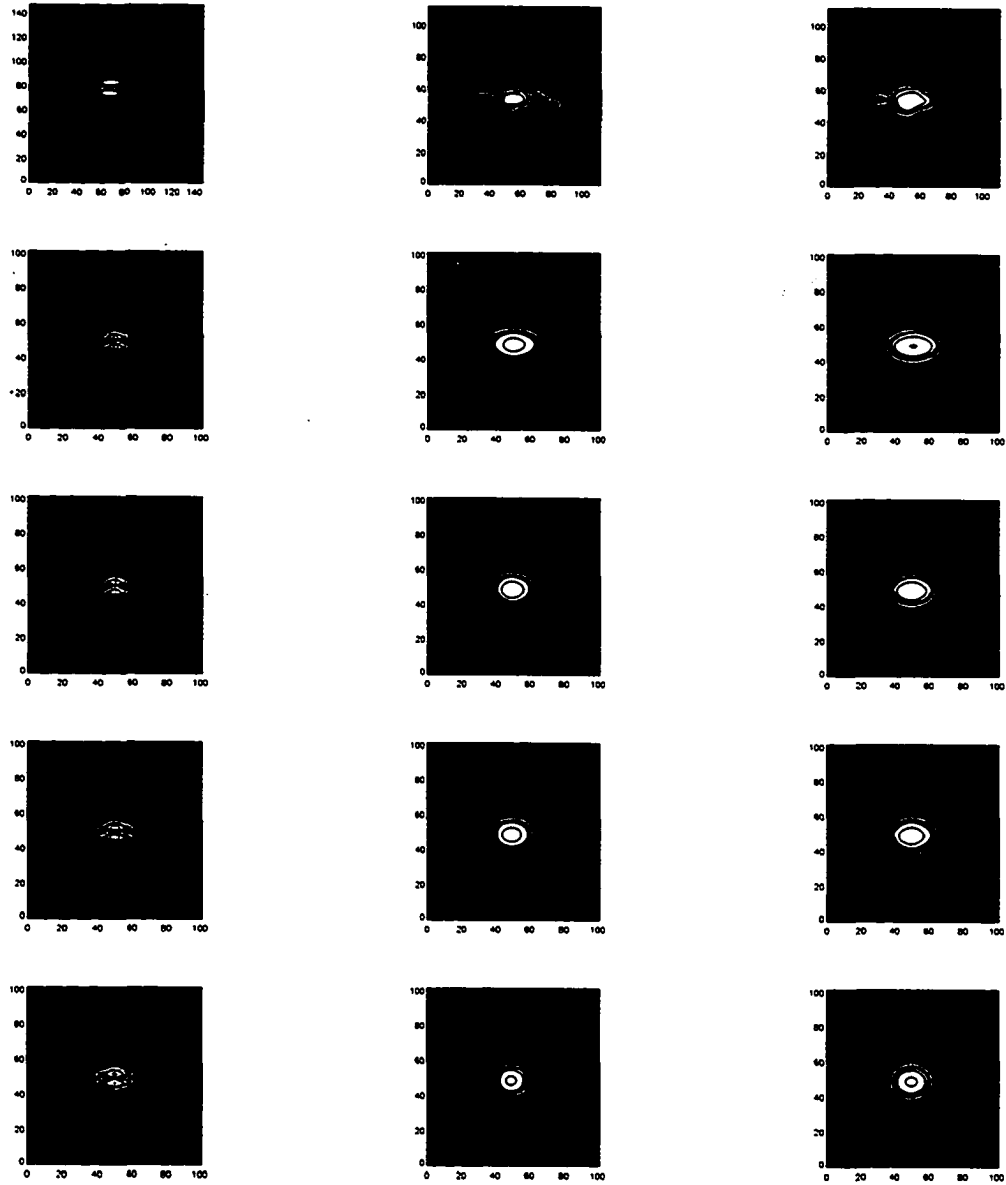


Figure F.13: Same as Figure F.10 except  $h_{\tau_{dust}} = 2080$  pc

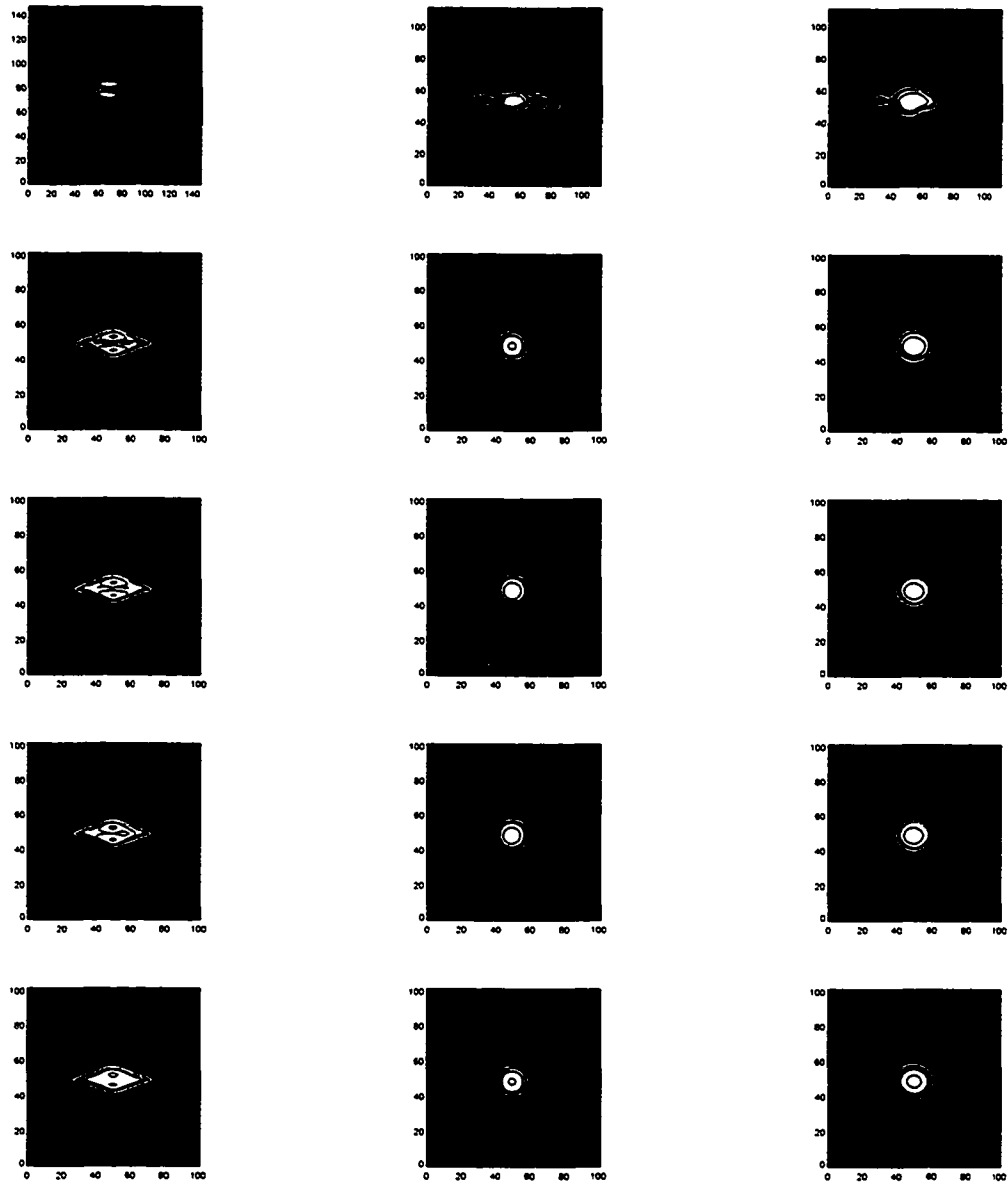


Figure F.14: Same as Figure F.10 except  $h_{z_{dust}} = 200$  pc &  $h_{r_{dust}} = 580$  pc

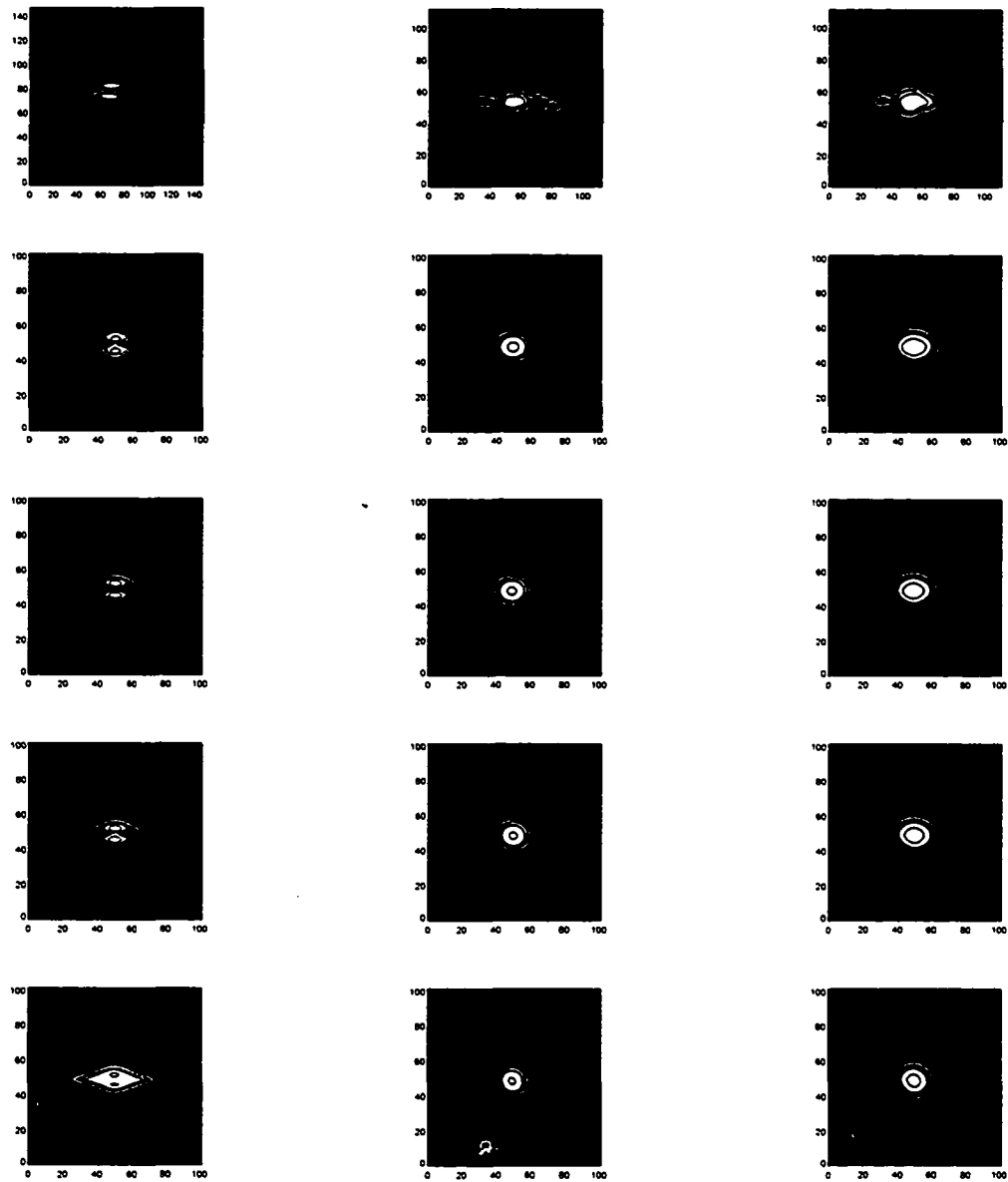


Figure F.15: Same as Figure F.14 except  $h_{r_{dust}} = 1080$  pc

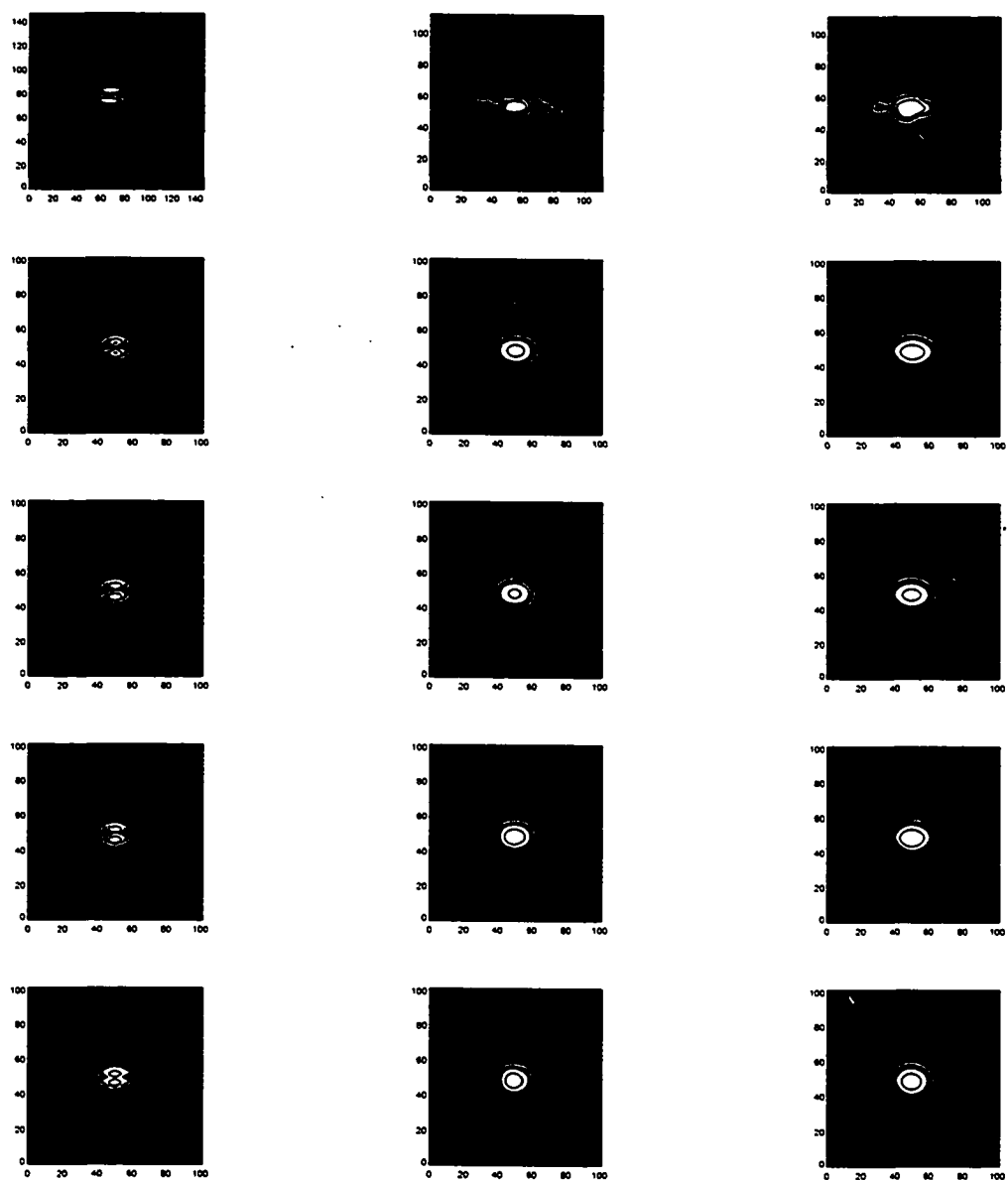


Figure F.16: Same as Figure F.14 except  $h_{r_{dust}} = 1580$  pc

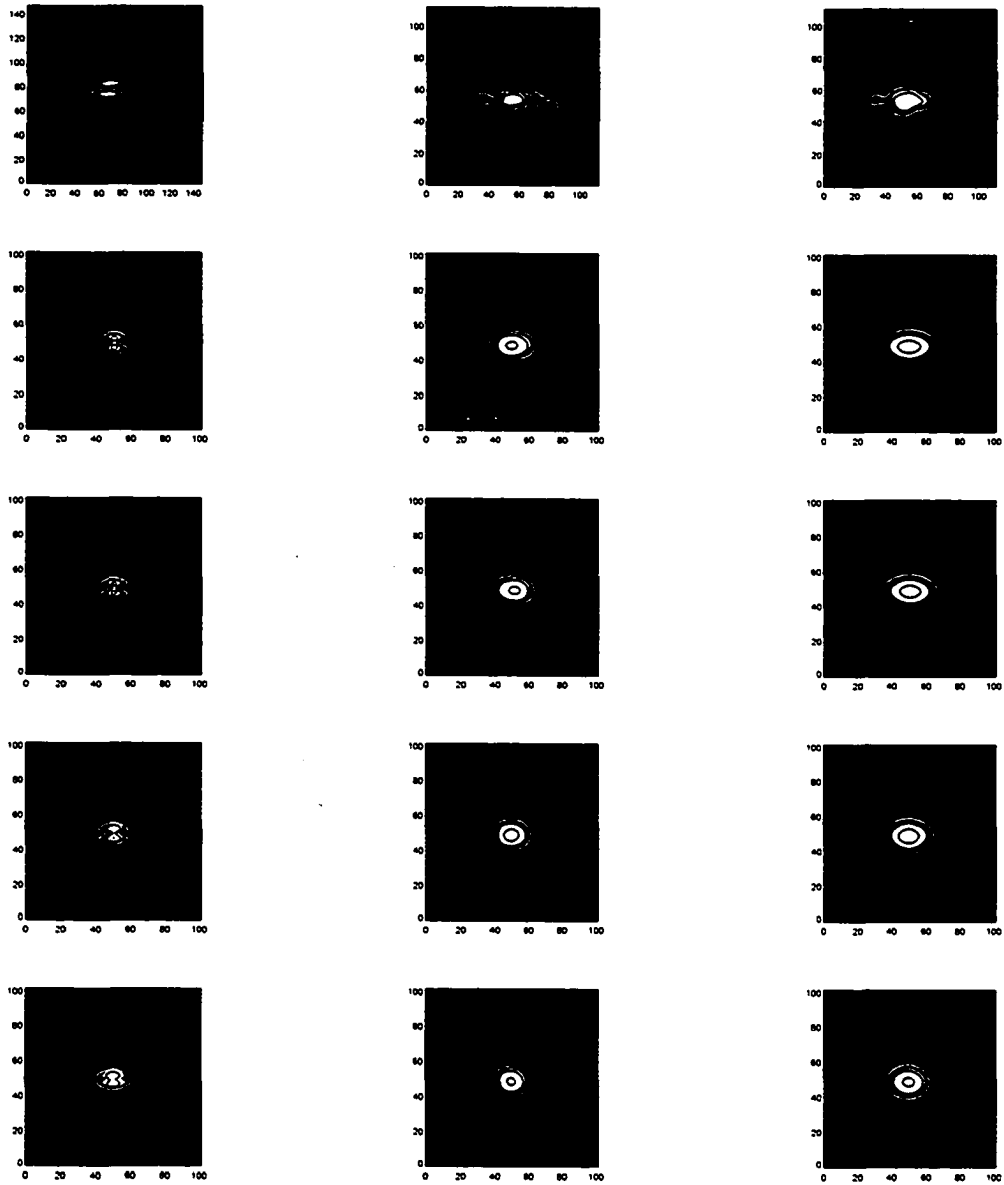


Figure F.17: Same as Figure F.14 except  $h_{r_{dust}} = 2080$  pc

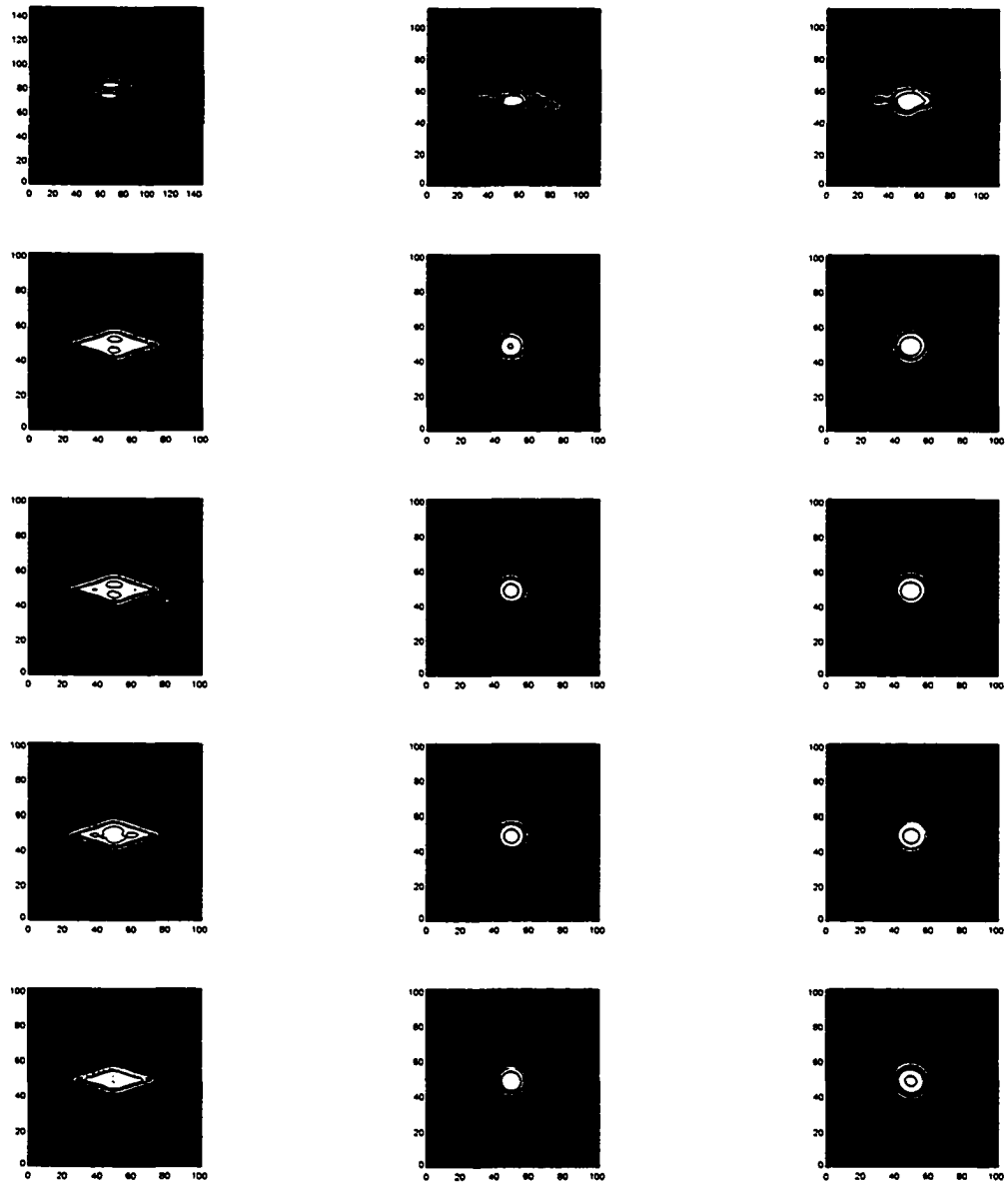


Figure F.18: Same as Figure F.14 except  $h_{z_{dust}} = 300$  pc &  $h_{r_{dust}} = 580$  pc

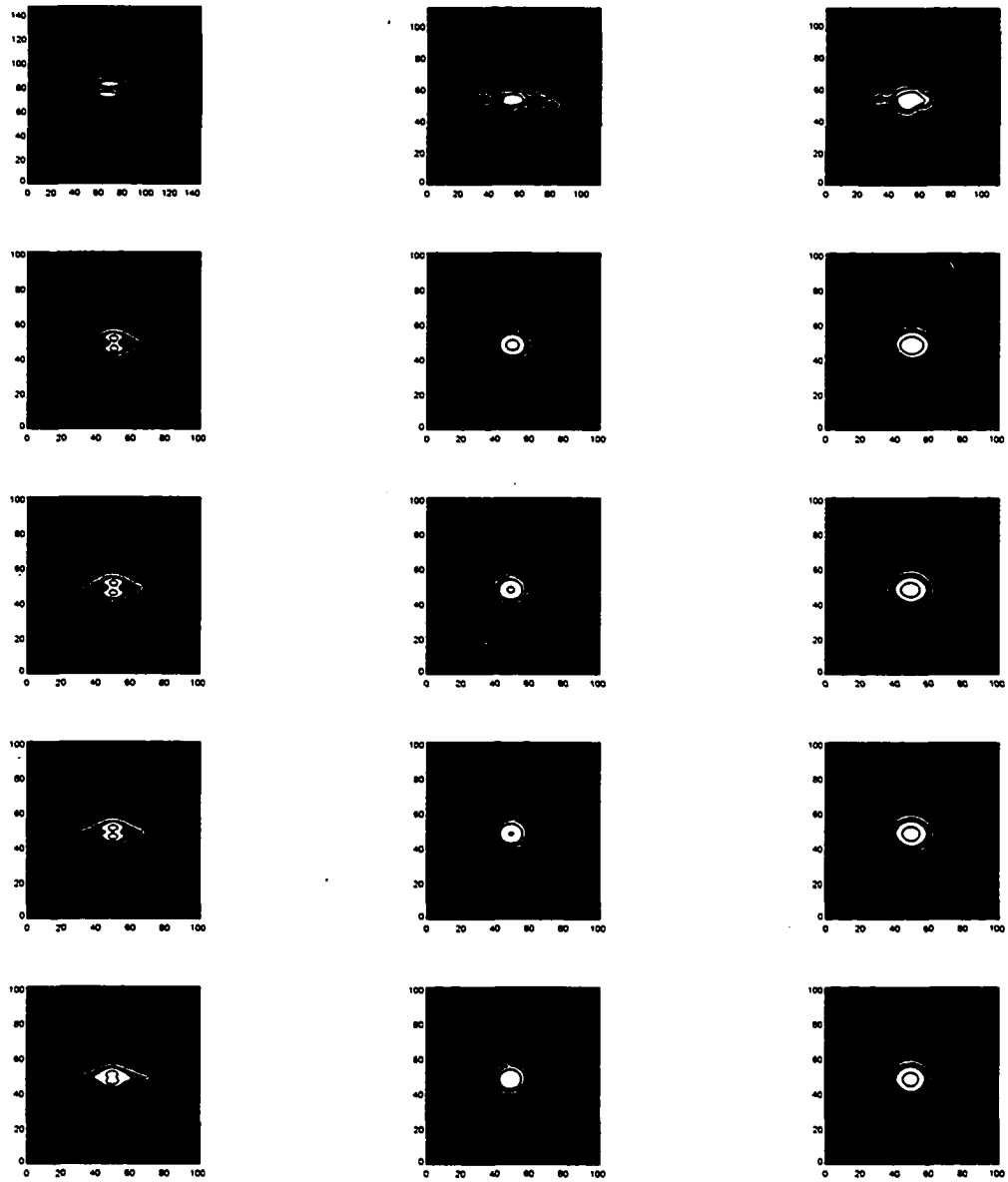


Figure F.19: Same as Figure F.18 except  $h_{r_{dust}} = 1080$  pc

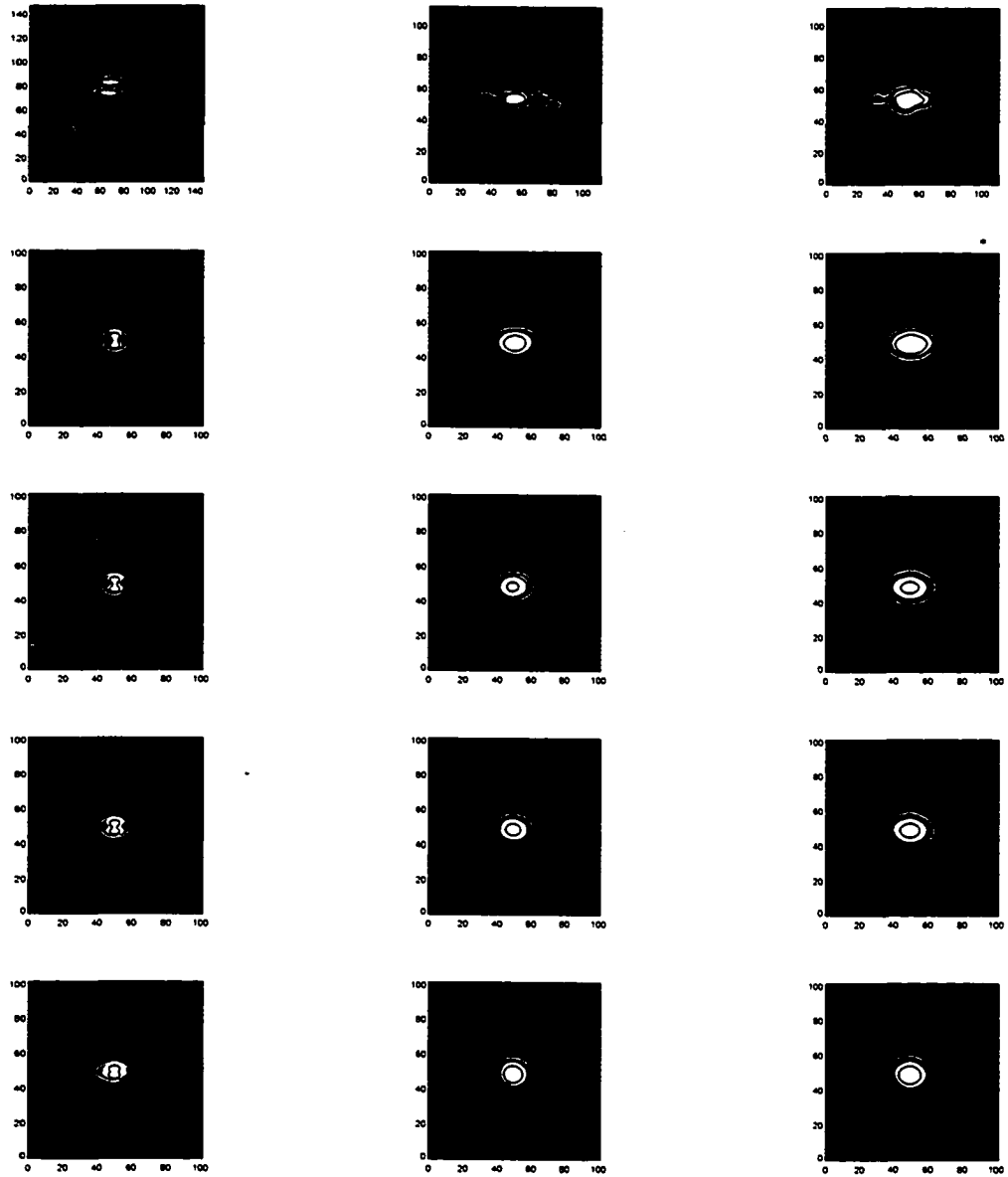


Figure F.20: Same as Figure F.18 except  $h_{r_{dust}} = 1580$  pc

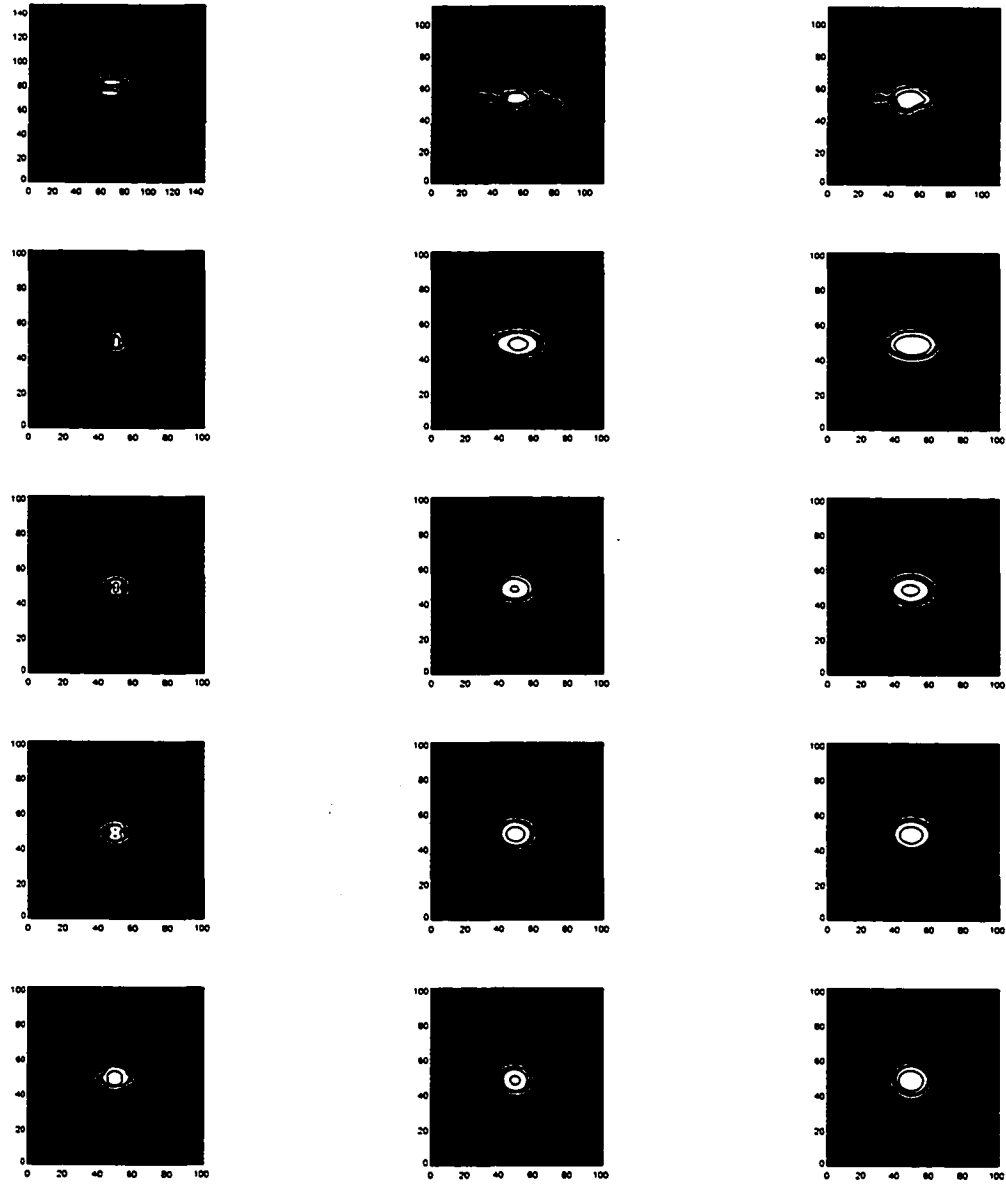


Figure F.21: Same as Figure F.18 except  $h_{r_{dust}} = 2080$  pc

---

# References

- Abell, G. O. 1965, *ARA&A*, **3**, 1
- Bertola, F., Buson, L. M., & Zeilinger, W. W. 1992, *ApJ*, **401**, L79
- Bessell, M. S. 1990, *PASP*, **102**, 1181
- Bjorkman, J. E., & Wood, K. 2001, *ApJ*, **554**, 615
- Bruzual A. G., & Charlot, S. 1993, *ApJ*, **405**, 538
- Burbidge, E. M., & Burbidge, G. R. 1960, *ApJ*, **131**, 224
- Byun, Y. I., Freeman, K. C., & Kylafis, N. D. 1994, *ApJ*, **432**, 114
- Casoli, F., Combes, F., Augarde, R., Figon, P., & Martin, J. M. 1998, *A&A*, **331**, 451
- Ciotti, L., & Pellegrini S. 1996, *MNRAS*, **279**, 240
- Ciotti, L., Pellegrini, S., Renzini, A., & D'Ercole, A. 1991, *ApJ*, **376**, 380
- Cowie, L. L., & Songaila, A. 1977, *Nature*, **266**, 501
- Davies, R. L., Sadler, E. M., & Peletier, R. F. 1993, *MNRAS*, **262**, 650
- de Grijs, R., & van der Kruit, P. C. 1996, *A&AS*, **117**, 19

- 
- Désert, F. X. 1986, in *Light on Dark Matter*, ed. F. P. Israel, p. 213
  - Devereux, N. A., & Young, J. S. 1990, *ApJ*, **359**, 42
  - Domingue, D. L., Keel, W. C., Ryder, S. D., & White, R. E. 1999, *AJ*, **118**, 1542
  - Dressler, A. 1980, *ApJ*, **236**, 351
  - Fabbiano, G., Kim, D.-W., & Trinchieri, G. 1992, *ApJS*, **80**, 531
  - Faber, S. M., & Gallagher, J. S. 1976, *ApJ*, **204**, 365
  - Fich, M., & Hodge, P. 1991, *ApJ*, **374**, 17L
  - Fich, M., & Hodge, P. 1993, *ApJ*, **415**, 75
  - Fisher, D., Franx, M., & Illingworth, G. 1996, *ApJ*, **459**, 110
  - Garcia-Burillo, S., Guélin, M., & Cernicharo, J. 1993, *A&A*, **274**, 123
  - Goldreich, P., & Kwan, J. 1974, *ApJ*, **189**, 441
  - Goudfrooij, P., & de Jong, T. 1995, *A&A*, **298**, 784
  - Greaves, J. S., White, G. J., Ohishi, M., Hasegawa, T., & Sunada, K. 1992, *A&A*, **260**, 381
  - Gunn, J. E., & Gott, J. R. 1972, *ApJ*, **176**, 1
  - Hafok, H., & Stutzki, J. 2003, *A&A*, **398**, 959

- 
- Helou, G. 1986, *ApJ*, **311**, 33L
  - Helou, G., Khan, I., Malek, L., & Boehmer, L. 1988, *ApJS*, **68**, 151
  - Henkel, C., & Wiklind, T. 1997, *Space Science Reviews*, **81**, 1
  - Hubble, E., 1936, *The Realm of The Nebula*, Dover, New York
  - Hubble, E., & Humason, M. L. 1931, *ApJ*, **74**, 43
  - Jaffe, W. 1983, *MNRAS*, **202**, 995
  - Jura, M. 1986, *ApJ*, **306**, 483
  - Kewley, L. J., Geller, M. J., Jansen, R. A., & Dopita, M. A. 2002, *AJ*, **125**, 3135
  - Khosroshahi, H. G., Wadadekar, Y., & Kembhavi, A. 2000, *ApJ*, **533**, 162
  - Kim, S. H., Martin, P. G., & Hendry, P. D. 1994, *ApJ*, **422**, 164
  - Knapp, G. R., Guhathakurta, P., Kim, D. W., & Jura, M. A. 1989, *ApJS*, **70**, 329
  - Knapp, G. R., & Gunn, J. E. 1982, *AJ*, **87**, 1634
  - Knapp, G. R., & Kerr, F. J. 1974 *A&A*, **35**, 361
  - Kutner, M. L., & Ulich, B. L. 1981, *ApJ*, **250**, 341
  - Kylafis, N. D., Misiriotis, A., Papamastorakis, J., & Xilouris, E. M. 2001, *Ap&SS*, **276**, 531

- 
- Larson, R. B., Tinsley, B. M., & Caldwell, C. N. 1980, *ApJ*, **237**, 692
  - Li, J. G., Seaquist, E. R., & Sage, L. J. 1993, *ApJ*, **411**, 71L
  - Mao, R. Q., Henkel, C., Schulz, A., Zielinsky, M., Mauersberger, R., Strzer, H., Wilson, T. L., & Gensheimer, P. 2000, *A&A*, **358**, 433
  - Matthews, L. D., & Wood, K. 2001, *ApJ*, **548**, 150
  - Melnick, J., & Sargent, W. L. W. 1977, *ApJ*, **215**, 401
  - Michard, R. 1998, *A&A*, **335**, 479
  - Miller, J. S., & Mathews, W. G. 1972, *ApJ*, **172**, 593
  - Moriarty-Schievens 2002, *private communication*
  - Naab, T., & Burkert, A. 2001, *ApJ*, **555**, L91
  - Nelder, J. A. and Mead, R. 1965, *Comput. J.*, **7**, 308
  - Nelson, A. E., Zaritsky, D., & Cutri, R. M. 1998, *AJ*, **115**, 2273
  - Oemler, A. 1974, *ApJ*, **194**, 1
  - Peletier, R. F., & Balcells, M. 1997, *NewA*, **1**, 349
  - Phillips, J. P., White, G. J., & Richardson, K. J. 1985, *A&A*, **151**, 421
  - Plana, H., Boulesteix, J., Amram, Ph., Carignan, C., & Mendes de Oliveira, C. 1998, *A&AS*, **128**, 75

- 
- Postman, M., Franx, M., Cross, N. J. G., Holden, B., Ford, H. C., et al. 2005, *ApJ*, **623**, 721
  - Radovich, M., Kahanpaa, J., & Lemke, D. 2001, *A&A*, **377**, 73
  - Rix, H-W., Carollo, C. M., & Freeman, K. 1999, *ApJ*, **513**, L25
  - Sage, L. J. 1990, *A&A*, **239**, 125
  - Sage, L. J. & Welch, G. A. 2005, in preparation
  - Sage, L. J., & Wrobel, J. M. 1989, *ApJ*, **344**, 204
  - Sandage, A. 1961, *The Hubble Atlas of Galaxies* Washington: Carnegie Inst. Washington
  - Sandage, A., & Visvanathan, N. 1978, *ApJ*, **225**, 742
  - Sandell, G., & Weintraub, D. A. 2001 *ApJS*, **134**, 115
  - Scorza, C., & Bender, R. 1995, *A&A*, **293**, 20
  - Scoville, N. Z., & Solomon, P. M. 1974, *ApJ*, **187**, 67L
  - Spitzer, L., & Baade, W. 1951, *ApJ*, **113**, 413
  - Tacconi, L. J., Tacconi-Garman, L. E., Thornley, M., & van Woerden, H. 1991, *A&A*, **252**, 541
  - Thronson, H. A., & Bally, J. 1987, *ApJ*, **319**, 63L

- 
- Thronson, H. A., Tacconi, L., Kenney, J., Greenhouse, M. A., Margulis, M., Tacconi-Garman, L., & Young, J. S. 1989, *ApJ*, **344**, 747
  - Tully, R. B. & Fisher, J. R. 1987, *Atlas of Nearby Galaxies*, Cambridge University Press
  - van Driel, W., & van Woerden, H. 1991, *A&A*, **243**, 71
  - Vila-Vilaró, B., Cepa, J., & Buntner, H. M. 2003, *ApJ*, **594**, 232
  - Welch, G. A. 2003, *private communication*
  - Welch, G. A., & Sage, L. J. 2003, *ApJ*, **584**, 260
  - White, R. E., Keel, W. C., & Conselice, C. J. 2000, *ApJ*, **542**, 761
  - Whitney, B. A., Wood, K., Bjorkman, J. E., & Wolff, M. J. 2003, *ApJ*, **591**, 1049
  - Wiklind, T., Combes, F., & Henkel, C. 1995, *A&A*, **297**, 643
  - Wiklind, T., & Henkel, C. 1989, *A&A*, **225**, 1
  - Wilson, C. D., Howe, J. E., & Balogh, M. L. 1999, *ApJ*, **517**, 174
  - Witt, A. N., Thronson, H. A., & Capuano, J. M. 1992, *ApJ*, **393**, 611
  - Xie, S., Young, J., & Schloerb, F. P. 1994, *ApJ*, **421**, 434
  - Young, J. S., Xie, S., Kenney, J. D. P., & Rice, W. L., 1989, *ApJS*, **70**, 699

# Curriculum Vitae

- **PERMANENT ADDRESS** 297 Shefford Street

Bromont, QC J2L 1B7

Phone:

email:

Birth date: May 15, 1978

Citizenship: Canadian

- **EDUCATION**

Languages: English, French

Ph.D. (projected), Astronomy, New Mexico State University, 2007

M.Sc., Astronomy, Saint Mary's University, 2005

B.ScH., Astrophysics, Queen's University, 2001

DEC, Pure & Applied Sciences, Champlain Regional Collage Lennoxville, 1998

High School Diploma, Massey-Vanier High School, 1995

- **CONFERENCES**

Kacprzak, G.G., Churchill, C.W., & Steidel, C.C. 2005, oral presentation at IAU Colloquium 199: Probing Galaxies Through QSO Abs Lines, Shanghai,

China March 14–18, March "Galaxy-Halo Gas Kinematic Connection  $0.3 < z < 1$ "

Kacprzak, G.G., Churchill, C.W., & Steidel, C.C. 2005 poster presentation, AAS conference, San Diego, CA, 09–13 January "Galaxy-Halo Gas Kinematic Connection  $0.3 < z < 1$ "

Churchill, C.W., Kacprzak, G.G., & Steidel, C.C. 2005 oral presentation, AAS conference, San Diego, CA, 09–13 January "Galaxy Properties and the Kinematics of Gaseous Halos"

Kacprzak, G.G., Churchill, C.W., & Steidel, C.C. 2004, oral presentation at The Environments of Galaxies: from Kiloparsecs to Megaparsecs, Crete, Greece, 9–13, August "Galaxy-Halo Gas Kinematic Connection  $0.3 < z < 1$ "

Kacprzak, G.G., & Welch, G.A. 2004, poster presentation, AAS conference, Atlanta, GA 4–8 January "The Cool Interstellar Medium of NGC 5866"

Kacprzak, G.G., & Welch, G.A. 2003, poster presentation, CASCA conference, University of Waterloo, ON 1–3 June "The Cool Interstellar Medium of NGC 5866"

- **PUBLICATIONS**

Galaxy Morphology - Halo Gas Connections

Kacprzak, G.G., Churchill, C.W., & Steidel, C.C. May 2005 Conference Proceedings. IAU 199: Probing Galaxies through Quasar Absorption Lines *astro-ph/0505211*

MgII Absorption through Intermediate Redshift Galaxies

Churchill, C.W., Kacprzak, G.G., & Steidel, C.C. April 2005 Conference Proceedings. IAU 199: Probing Galaxies through Quasar Absorption Lines astro-ph/0504392

Models of Five Absorption Line Systems Along the Line of Sight Toward PG0117+213

Masiero, J.R., Charlton, J.C., Ding, J., Churchill, C.W., & Kacprzak, G.G. 2005 ApJ, 623, 57

Mg II Absorbing Galaxies: Morphologies and Kinematics

Churchill, C.W., Steidel, C.C., & Kacprzak, G.G. Nov 2004, Dwingeloo Conference Proceedings astro-ph/0411269

• **HONOURS AND AWARDS**

- o Award of Merit-based Enhancement Fellowship, 2005
- o New Mexico State University Graduate Scholarship, 2005
- o Pegasus Teaching Award, 2004
- o New Mexico State University Graduate Scholarship, 2004
- o Sigma Xi Grant, 2003
- o New Mexico State University Graduate Scholarship, 2003
- o JCMT CANSERV time, 2002
- o Saint Mary's University Graduate Scholarship, 2002

---

o Saint Mary's University Graduate Scholarship, 2001

o Queens University Bursary Award, 1999

● **WORK HISTORY**

EMPLOYER: New Mexico State University, Astronomy Department

PERIOD: August 2003 - December 2003 - 2005

DUTIES: Instructor for two first year Astronomy labs and giving the occasional lecture to the same class.

EMPLOYER: Saint Mary's University, Astronomy Department

PERIOD: January 2003 - April 2003

DUTIES: Instructor for the first year Physics tutorial and giving the occasional lecture to the same class.

EMPLOYER: Saint Mary's University, Astronomy Department

PERIOD: September 2001 - April 2003

DUTIES: Instructor for the first year physics component of the forensics labs. Conducting public tours of our telescope, supervising tutorials and labs for two first year Physics classes.

EMPLOYER: IBM in Bromont, Qc.

PERIOD: May 1996 - August 2002

DUTIES: Testing plastic memory pieces, constructing processing units for companies such as: Hewlett Packard, Nortel, VLSI, and Nintendo. Involved the operation of complicated machinery and the use of various problem solving

techniques.

● REFERENCES

Dr. Gary Welch, Professor, (St. Mary's ext: 5637)

Dr. David Guenther, Professor, (St. Mary's ext: 5832)

Dr. Chris Churchill, Assistant Professor, NMSU 505-646-1913